# Patterns of spike synchrony in neural field models

Jose M. Esnaola Acebes

TESI DOCTORAL UPF / 2018

DIRECTOR DE LA TESI:

Ernest Montbrió,
Department of Information and Communication Technologies

*Amatxori, Aitatxori eta Mikeli, beraiek izan baitira lan honen haziak.*

*A ti, compañera de mis días y del porvenir ...*

# Esker onak — Agraïments — Agradecimientos

Este trabajo culmina el final de una etapa que ocupa, aunque parezca extraño decirlo, algo más de un 5% de la vida de un individuo medio en nuestro país. Una etapa en la cual he tenido la oportunidad y la suerte de conocer a innumerables personas que han afectado de una manera u otra en el desarrollo de esta tesis. Es por lo tanto imposible agradecer todo lo recibido durante este tiempo en unas pocas páginas.

Evidentment, aquest treball no hauria sigut possible sense l'Ernest, sense la seva ajuda, paciència i dedicació en la direcció de la meva tesi. Perquè no només ha sigut un director de tesi atent i comprensiu del que he pogut aprendre tant, sinó que també ha sigut un company i un amic amb el que hem gaudit de tantíssimes converses i discussions enriquidores.

A David y Federico, que se unieron a nuestro reducido pero entrañable grupo y con los que he podido compartir tantas experiencias, a ellos quiero agradecerles su compañerismo, lealtad, honradez y generosidad. Especial mención se merece la inestimable ayuda de Federico en el desarrollo último de esta tesis.

Gracias también a nuestro colaborador habitual, Alex Roxin, por su importante contribución a todo este trabajo sin el cual difícilmente hubiese podido progresar. Aprovecho también para agradecer su esfuerzo a la hora de organizar tantísimos eventos relacionados con la neurociencia computacional y de los cuales nos hemos beneficiado tantas personas en Barcelona.

Gracias a todos los miembros del grupo de Gustavo y al mismo Gustavo, que nos acogen en su magnifico grupo como a unos más. Gracias a los que están; Gorka, Adrián, Victor, Andrea, Vicente, Josefina, Matthieu, Silvana, Mohit, ... y a los que estuvieron.

I want to thank all the anonymous people of the open software community from which I have benefited so much during my PhD, thanks to all the deveolopers of Python, Linux, C, etc. , that offer their work in a completely free and selfless manner. Every day, they prove that a world were solidarity and self-organization is the norm is possible.

Gracias a mis compañeras del despacho durante la etapa en Poblenou, Elisa, Cristina, Joanna, Pallabi, Loreto, Stephanie y Luis, y a todos los demás miembros de los despachos "satélite", Irene, Kalinka, Gabriele, Sanders, Marc, Jesús, Elena, ... por su incansable y alegre compañía. Por acompañarme y arroparme durante algunos de los momentos más duros de

esta etapa. Y a todos aquellos que se incorporaron más tarde en Ciutadella y que me apoyaron especialmente durante el último año. Milesker Iñigori bere bizitzarekiko ikuspuntu interesgarria erakusteagatik, beren baikortasun amaiezina banatzeagatik eta berarekin izan ditugun elkarrizketa eta erreflexio ugariengatik.

No me puedo olvidar de la gente del IDIBAPS y de su extenso entorno, por los seminarios compartidos y por la pasión desprendida por muchos de ellos: Albert, Jaime, Klaus, Ainhoa, Genis, Maria, Joao, Alberto, ...

Y menos aún de Marina, por su admirable forma de ver la vida y por su energía al enfrentarse a las innumerables incoherencias que inundan el mundo de la ciencia. Gracias por su visión armonizadora de la tierra y de todos los seres que la pueblan. Gracias a Bernat, con el que empecé este viaje, y con el cual sobran las palabras.

Gracias a todos los compañeros de docencia en los grados de la escuela de ingeniería de la UPF, a Gloria, Àngel, Jordi, ... y a todos los estudiantes que tuvieron la paciencia de escuchar. Gracias a ellos por permitirme aprender tanto enseñando tan poco.

Termino agradeciendo a los que siempre están y estarán ahí, a los que nunca piden nada a cambio, y a los que les debo todo. Eskerrik asko Amatxori eta Aitatxori, beraien bizitza emateagatik eta bizitzan benetan garrantzia dituzten gauzak irakasteagatik. Eta Mikeli beti nirekin egoteagatik eta beti niri zaintzeko prest egoteagatik. Eskerrik asko izeba Jexuri eta familia guztiari geuren bizitzako momentu zailetan eskeiniko laguntzagatik. Gracias de nuevo Mamá, por todo el amor infinito que nos diste y nos sigues dando, por ese regalo que es la vida que parece no acabar con la muerte.

Gracias a todos los demás miembros de la familia, Nuria, Enric, Robert por acogerme en vuestro seno. A Tere, a la petita Valentina, a la Montse i al Xavi, a la Pilar i al seu Xavi per rebre'ns sempre amb els braços oberts.

Y evidentemente, gracias a Laia, por acompañarme todo este tiempo, por escucharme, ayudarme y aguantarme. Por todo lo que has hecho y haces por mí. Y por el futuro que nos espera.

*Barkamena amalurrari,*
*bere maitasun iturri amaiezinari,*
*tesi hau egiteko xahututako energiarengatik,*
*merezi bezala zaindu ez izanagatik.*
*Eskerrik asko itsasoari, mendiari, zeruari,*
*euren handitasun zirraragarriari,*
*txiki sentiarazteagatik,*
*amalurran barne bizi naizela oroitarazteagatik.*

— Iñigo Romero Arandia

# Resum

Els models neuronals de camp mig són descripcions fenomenològiques de l'activitat de xarxes de neurones espacialment organitzades. Gràcies a la seva simplicitat, aquests models són unes eines extremadament útils per a l'anàlisi dels patrons espai-temporals que apareixen a les xarxes neuronals, i s'utilitzen àmpliament en neurociència computacional. És ben sabut que els models de camp mig tradicionals no descriuen adequadament la dinàmica de les xarxes de neurones si aquestes actuen de manera síncrona. No obstant això, les simulacions computacionals de xarxes neuronals demostren que, fins i tot en estats d'alta asincronia, fluctuacions ràpides dels inputs comuns que arriben a les neurones poden provocar períodes transitoris en els quals les neurones de la xarxa es comporten de manera síncrona. A més a més, la sincronització també pot ser generada per la mateixa xarxa, donant lloc a oscil·lacions auto-sostingudes.

En aquesta tesi investiguem la presència de patrons espai-temporals deguts a la sincronització en xarxes de neurones heterogènies i espacialment distribuïdes. Aquests patrons no s'observen en els models tradicionals de camp mig, i per aquest motiu han estat àmpliament ignorats en la literatura. Per poder investigar la dinàmica induïda per l'activitat sincronitzada de les neurones, fem servir un nou model de camp mig que es deriva exactament d'una població de neurones de tipus *quadratic integrate-and-fire*. La simplicitat del model ens permet analitzar l'estabilitat de la xarxa en termes del perfil espacial de la connectivitat sinàptica, i obtenir fórmules exactes per les fronteres d'estabilitat que caracteritzen la dinàmica de la xarxa neuronal original. Aquest mateix anàlisi també revela l'existència d'un conjunt de modes d'oscil·lació que es deuen exclusivament a l'activitat sincronitzada de les neurones. Creiem que els resultats presentats en aquesta tesi inspiraran nous avenços teòrics relacionats amb la dinàmica col·lectiva de les xarxes neuronals, contribuïnt així en el desenvolupament de la neurociència computacional.

# Laburpena

Eremu-neuronalen ereduak (EME), sare neuronal trinkoen aktibitatearen deskripzio fenomenologikoak dira. Eredu hauek neurozientzia konputazionalean sarritan erabiltzen dira, azterketa matematikoa errazteko aukera ematen baitute eta aldi berean ordenagailuz egindako simulazioen denbora eta zailtasuna asko murrizten dutelako. Alegia, sare neuronal asinkronoetan ageritako patroi anitzak aztertzeko baliabide teoriko eskuragarriak direla frogatu dute behin eta berriro. Ezaguna da baina, eredu tradizional hauek dauzkaten mugen artean, neuronek askotan erakusten duten aktibitate sinkronizatua deskribatzeko ezintasuna dela garrantzitsuenetariko bat. Ordea, simulazio numerikoek erakusten duten bezala, nahiz eta neuronak egoera guztiz asinkronoan egon, kanpotik ezarritako korronteen fluktuazio handiek aktibitate altuko tarteak eragin ditzakete, non sarea osaturiko neuronek modu sinkronoan jarduten dute. Orobat, fluktuazio horiek oso arruntak dira nerbio-ehunetan neurtutako dinamiketan.

Tesi honetan, aipatutako muga hori arakatzen dugu, EME tradizionalek erakusten dituzten dinamikak, sare neuronalen simulazioak eskaintzen dituzten emaitzekin konparatuz, eta honela neuronen sinkronizazio kolektiboak dinamika makroskopikoan daukan eragina aztertzen dugularik. Hain zuzen ere, sinkronizazioak sare horietan patroi espazio-tenporal, bai iragankorrak edota iraunkorrak, eragiteko gaitasuna daukala erakusten dugu. Patroi horiek sortarazten dituzten oinarrizko arrazoiak ikertzeko, EME berri bat garatu dugu, sare neuronalen dinamikatik zehazki deribatuta dagoena. Erdietsiko eredu berri honek neurona kitzikatzaileen eta inhibitzaileen arteko interakzioek induzitutako patroi espazio-tenporal multzo bat ikertzeko aukera ematen digu. Bereziki, oreka-egoeran, uhin-zenbaki ezberdineko perturbazio espazialek maiztasun ezberdineko uhin-geldikor iragankorrak sortzen dituztela aurkitu dugu, hots, tentsioan dagoen soka batean ageri diren modu normalen moduan. Horrez gain, uhin horien maiztasunak konektibitate sinaptikoaren profilarekin harreman estua dutela, eta gainbeheratze-tasa, sarearen heterogeneitatearen mendean besterik ez dagoela ikusi dugu.

# Resumen

Los modelos neuronales de campo medio son descripciones fenomenológicas de la actividad de redes de neuronas organizadas espacialmente. Debido a su simplicidad, dichos modelos son herramientas extremadamente útiles para el análisis de los patrones espacio-temporales que surgen en redes neuronales, i son ampliamente utilizadas en neurociencia computacional. Es bien sabido que los modelos de campo medio tradicionales no describen adecuadamente la dinámica de las redes de neuronas si éstas actúan de manera síncrona. Sin embargo, las simulaciones computacionales de redes de neuronas demuestran que, incluso en los estados con actividad altamente asíncrona, fluctuaciones rápidas en los inputs comunes que llegan a las neuronas pueden provocar períodos transitorios de actividad sincronizada. Además, la sincronización también puede ser generada por la propia red, dando lugar a oscilaciones robustas y auto-mantenidas.

En esta tesis investigamos la aparición de patrones espacio-temporales en redes heterogéneas de neuronas espacialmente distribuidas, relacionados con la actividad sincronizada de las neuronas. Estos patrones no se observan en los modelos tradicionales de campo medio y han sido en gran parte ignorados en la literatura. Para poder investigar los fenómenos inducidos por la actividad sincronizada de las neuronas empleamos un nuevo modelo de campo medio que proviene de la derivación exacta de la dinámica de una población de neuronas de tipo *quadratic integrate-and-fire*. La simplicidad del modelo nos permite analizar la estabilidad de la red en términos del perfil espacial de conectividad sináptico, i nos permite obtener fórmulas exactas para las fronteras de estabilidad que caracterizan la dinámica de las red neuronal original. Notablemente, el análisis también revela la existencia de un conjunto de modos de oscilación que se deben exclusivamente a la actividad sincronizada de las neuronas. Creemos que los resultados presentados en esta tesis inspirarán nuevos avances teóricos relacionados con la dinámica colectiva de las redes neuronales, contribuyendo así en el desarrollo de la neurociencia computacional.

# Abstract

Neural field models are phenomenological descriptions of the activity of spatially organized, recurrently coupled neuronal networks. Due to their mathematical simplicity, such models are extremely useful for the analysis of spatiotemporal phenomena in networks of spiking neurons, and are largely used in computational neuroscience. Nevertheless, it is well known that traditional neural field descriptions fail to describe the collective dynamics of networks of synchronously spiking neurons. Yet, numerical simulations of networks of spiking neurons show that, even in the case of highly asynchronous activity, fast fluctuations in the common external inputs drive transient episodes of spike synchrony. Moreover, synchronization may also be generated by the network itself, resulting in the appearance of robust large-scale, self-sustained oscillations.

In this thesis, we investigate the emergence of synchrony-induced spatiotemporal patterns in spatially distributed networks of heterogeneous spiking neurons. These patterns are not observed in traditional neural field theories and have been largely overlooked in the literature. To investigate synchrony-induced phenomena in neuronal networks, we use a novel neural field model which is exactly derived from a large population of quadratic integrate-and-fire model neurons. The simplicity of the neural field model allows us to analyze the stability of the network in terms of the spatial profile of the synaptic connectivity, and to obtain exact formulas for the stability boundaries characterizing the dynamics of the original spiking neuronal network. Remarkably, the analysis also reveals the existence of a collection of oscillation modes, which are exclusively due to spike-synchronization. We believe that the results presented in this thesis will foster theoretical advances on the collective dynamics of neuronal networks, upgrading the mathematical basis of computational neuroscience.

**Keywords:** mathematical neuroscience, spatiotemporal patterns, oscillations, bump states, synchronization, neural population, firing rate, population model, spiking neurons, quadratic-integrate-and-fire, neural-field, mean-field.

# Preface

This work is intended to explore, and hopefully rise some new questions, on the role of spike synchrony in shaping the dynamics of large networks of spiking neurons, and the ability of Neural Field models to capture such macroscopic phenomena.

Due to the astonishing number of neurons in the brain, almost any theoretical approach to study large-scale brain processes requires the use of some sort of population model. As such, neural field models have been extensively used as modeling tools to describe the activity of the brain, in which the interaction of millions of neurons is treated as a continuum. Indeed, they have proved to be a valuable tool to describe the average firing rate activity of neuronal ensembles in a wide range of situations. However, they only constitute an heuristic representation of the underlying microscopic state, and unfortunately, they do not guarantee a complete description of the macroscopic dynamics arising in networks of spiking neurons. Specifically, neural field models are typically derived by assuming uncorrelated neural activity and therefore fail to describe any collective dynamics which may appear as a consequence of the synchronized spiking of neurons.

Despite these constraints that limit the applicability of neural field models, they are broadly used to model a great variety of dynamics involving interacting populations of neurons. Typical descriptions include both excitatory and inhibitory interactions which give rise to an extensive cacophony of spatiotemporal patterns. Experimental observations of qualitatively similar patterns often report the existence of correlations among neurons during such dynamical regimes. Our question is then, whether synchronous activity is just an inessential detail that can be ignored, or instead, plays a decisive role in shaping the macroscopic neuronal dynamics. We think that an answer to this question may help in developing more suitable macroscopic models, and hopefully shed some light into the basic principles governing collective neuronal dynamics. The main result of this work is the derivation of a novel neural field model which explicitly takes into account the sub-threshold dynamics of its constituent neurons, and thus is able to exactly describe synchrony-related dynamics. Additionally, it enable us to investigate a particular form of oscillatory behavior which is observed in spiking neural networks, and for which traditional neural field models have no valid description. That is, the synchrony-induced decaying standing waves.

In chapter 1 we review fundamental aspects relevant to our work, first

by introducing the main features of traditional neural field models, and then showing some of the spatiotemporal patterns that they are capable of reproducing when considering excitatory and inhibitory interactions. Next, we conduct a series of numerical experiments displaying a variety of patterns which are directly related to synchronization processes, and for which traditional neural field models have no appropriate description. Finally, we finish the chapter presenting the derivation of the population model which exactly describes the activity of a network of spiking neurons and show some of the results associated to that model.

In chapter 2 we extend the firing rate model presented in chapter 1 to a spatially extended network of spiking neurons, and obtain an exact neural field model for a network of quadratic integrate-and-fire neurons. The model will then allow us to analytically investigate the oscillatory phenomena observed in the numerical experiments. This analysis indicates that synchronous activity is indeed relevant in shaping the dynamics of neural networks and therefore it may play an important role in neural processing during cognitive tasks.

We finish by discussing the most relevant results of this thesis and comment on their potential implications as relevant modeling tools in neuroscience. Additionally, we comment on future work that could be done to further improve the presented model, and about potential extensions that could account for additional neuronal features.

# Contents

**Abstract** xi

**Preface** xiii

**Contents** xvii

**List of figures** xx

**Introduction** 1

**Chapter 1 NEURAL FIELD MODELS AND THEIR FAILURE TO DESCRIBE SPIKE-SYNCHRONY** 9

1.1. Traditional neural field models . . . . . 9

1.1.1. Excitation-inhibition based spatiotemporal phenomena in neural field models . . . . . 18

1.1.1.1. Interneuron Network Gamma (ING) oscillations . . . . . 19

1.1.1.2. Pyramidal Interneuron Network Gamma (PING) oscillations . . . . . 25

1.1.1.3. Spatially inhomogeneous patterns: bump states (BS) . . . . . 28

1.2. Spike-synchrony in neural field models . . . . . 31

1.3. Firing rate model for quadratic integrate-and-fire neurons . 44

1.3.1. Quadratic Integrate-and-Fire (QIF) model neuron . 45
1.3.2. Continuity equation for a population of quadratic integrate-and-fire neurons . . . . . 48
1.3.2.1. Continuous formulation . . . . . 49
1.3.3. Dimensionality reduction: Lorentzian Ansatz . . . 50
1.3.4. Solution to the continuity equation: firing rate equations for quadratic integrate-and-fire neurons . . . 53
1.3.5. Firing rate equations with synaptic kinetics . . . . 57
1.3.5.1. The limit of slow synapses: a low-pass filtered version of Eqs. (1.58) . . . . . 59
1.3.6. Recent development on the quadratic integrate-and-fire firing rate model . . . . . 60

**Chapter 2 SYNCHRONY-INDUCED MODES OF OSCILLATION OF A NEURAL FIELD MODEL 63**

2.1. Introduction . . . . . 64
2.2. Synchrony-induced modes of oscillation in Networks of quadratic integrate-and-fire Neurons . . . . . 66
2.3. Neural Field model for quadratic integrate and fire neurons 69
2.3.1. Effective neural field model for quadratic integrate-and-fire neurons . . . . . 70
2.3.2. Spatially homogeneous states and their stability: Synchrony-induced modes of oscillation . . . . . 71
2.3.3. Turing bifurcation and nonlinear stability of the spatially homogeneous states . . . . . 74
2.3.4. Synchrony-induced transient oscillations in bump states . . . . . 74
2.4. Conclusions . . . . . 77
**Chapter Appendices** . . . . . 79
2.A. Derivation of the quadratic integrate-and-fire neural field model (QIF-NFM) . . . . . 79
2.A.1. Effective neural field model . . . . . 81
2.B. Linear stability analysis of the spatially homogeneous states 82
2.B.1. Linear stability of the effective QIF-NFM Eq. (2.7) 82
2.B.2. Linear stability of the full QIF-NFM . . . . . 83
2.C. Small-amplitude equation near the Spatially Homogeneous State . . . . . 85
2.C.1. Critical eigenvectors . . . . . 85

2.C.2. Amplitude equation . . . . . 85
2.D. Numerical simulations . . . . . 89
2.D.1. Numerical simulation of the QIF model . . . . . 89
2.D.2. Numerical simulation of the ring network . . . . . 90

**Discussion** **93**

**Appendix A NUMERICAL SIMULATIONS** **99**
A.1. Simulations of spiking neural networks . . . . . 99

**Appendix B MATHEMATICAL APPENDIX** **107**
B.1. Derivation of the firing rate equations . . . . . 107
B.1.1. Reduction to a system of two ordinary differential equations: QIF firing rate equations . . . . . 108
B.2. Firing rate equations of conductance based spiking neurons 110

**References** **129**

# List of Figures

1.1. Diagram of effective networks for two-population and ring models. . . . . 14
1.2. Space-time plots of the heuristic neural field model (H-NFM). 17
1.3. Interneuron Network Gamma (ING) and Pyramidal Interneuron Network Gamma (PING) mechanisms. . . . . 20
1.4. Interneuron Network Gamma (ING) oscillations for different versions of the heuristic neural field model. . . . . 24
1.5. Symmetry breaking and bump state in the effective two population model and its homologous ring neural field model. 30
1.6. Transient oscillations in a leaky integrate-and-fire (LIF) neuronal population. . . . . 33
1.7. Transient activity of an uncoupled network of quadratic integrate-and-fire neurons. . . . . 35
1.8. Interneuron Network Gamma (ING) oscillations in networks of heterogeneous inhibitory neurons. . . . . 38
1.9. Interneuron Network Gamma (ING) oscillations in networks of identical inhibitory neurons under gaussian white noise. 39
1.10. Pyramidal Interneuron Network Gamma (PING) oscillations in networks of heterogeneous excitatory and inhibitory neurons. . . . . 41
1.11. Transient episodes and bump states in networks of spiking neurons. . . . . 43
1.12. Possible regimes of the quadratic integrate-and-fire (QIF) model neuron. . . . . 47

1.13. Membrane potential distribution of quadratic integrate-and-fire (QIF) neurons and firing rate of the population. . . . . 53
1.14. Phase diagram, and phase portraits of QIF-FREs. . . . . 56

2.1. Schematics of the excitatory-inhibitory ring network. . . . 67
2.2. Transient synchrony in ring networks of quadratic integrate-and-fire (QIF) neurons . . . . . 69
2.3. Stability of the spatially homogeneous state (SHS) ($J_K$ vs. $\bar{\eta}$). 73
2.4. Phase diagram of the QIF-NFM ($J_K$ vs. $\bar{\eta}$). . . . . 75
2.5. Spectrum and firing rate profiles of the bump state. . . . . 76
2.D.1. Euler integration of QIF neurons. . . . . 90

A.1. Exponential integrate-and-fire (EIF) neuron model: $f(v)$ curve. . . . . 102
A.2. Transfer function of a population of leaky integrate-and-fire (LIF) neurons. . . . . 104

B.1. Residue Theorem: Contour around $\bar{\eta} - i\Delta$. . . . . 109
B.1. Pyramidal Interneuron Network Gamma (PING) oscillations in a network of conductance-based spiking neurons. . . . . 111

# Introduction

> *"Philosophy is written in this great book—by which I mean the universe—which stands always open to our view, but it cannot be understood unless one first learns how to comprehend the language and interpret the symbols in which it is written, and its symbols are triangles, circles, and other geometric figures, without which it is not humanly possible to comprehend even one word of it; without these one wanders in a dark labyrinth."*
>
> — Galileo Galilei, *Il Saggiatore* (The Assayer) (1623)

Since the pioneering discoveries of Santiago Ramon y Cajal and Camilo Golgi in the late 19th century which established the foundations of what we nowadays know as Neuroscience, extensive work has been done in order to understand the laws that shape neuronal dynamics. As in almost any natural science, the aim of scientists toward universal laws explaining our observations have pushed, from the very beginning, towards mathematical descriptions of the observed phenomena. With the birth of *neural theory* researchers sought to understand the secrets behind animal behavior looking into the microscopic constituents of its source: the neurons. Early in the 20th century, Louis Lapicque introduced what is considered as the precursor of the famous integrate-and-fire model neuron (Brunel and Van Rossum, 2007b) (see also Brunel and Van Rossum, 2007a; Abbott, 1999), providing a first quantitative approach to the depolarization process of neurons and modeling the generation of the first spike after the stimulus onset —what we know as the action potential. Theoretical neuroscience was born and

following his work many phenomenological models describing the onset of the action potential were developed (Hill, 1936; McCulloch and Pitts, 1943; Stein, 1965; Geisler and Goldberg, 1966; Weiss, 1966; Stein, 1967).

In the 1950's Hodgkin and Huxley published the first detailed biophysical model of the action potential (Hodgkin and Huxley, 1952), a system of four differential equations which modeled the electrical currents across the cell membrane leading to action potentials in the squid's giant axon, and for which they received the Nobel price in 1963. Their almost 30 year investigation not only proved that detailed biophysical —yet simple and elegant— models of neuronal dynamics were possible, but also drove them to the hypothesis of the existence of ionic channels, which were confirmed only few decades later.

## Modeling from the microscopic perspective: Spiking neuron models

Further development in the biophysical principles of neuronal dynamics was made with the study of additional cellular mechanisms involved in the reception and generation of the action potentials, such as different classes of ionic channels and pumps, synaptic transmission processes, etc. Currently, detailed biophysical modeling of single neurons remains a very active field of research where sophisticated models are continuously expanding our knowledge about neural mechanisms. On the other hand, the necessity of decreasing the complexity of neuronal systems lead many theoreticians towards simplified models of the neuron, where only the most fundamental mechanisms that generate the action potential were sought. We refer to these phenomenological models as point neurons or **spiking neuron** models. The first of its kind was probably that developed by Lapicque which later evolved into the *leaky integrate-and-fire* (LIF) neuron model (Stein, 1965; Knight, 1972; Tuckwell, 1988).

The LIF model and the more general nonlinear integrate-and-fire models can be mathematically derived as limit cases of the Hodgkin-Huxley model (see for example Gerstner et al., 2014); they are typically presented in the form of an ordinary differential equation (ODE) describing the time evolution of the membrane potential of the neuron, plus a resetting rule mimicking the generation of the action potential, which basically drives the potential back to a reset potential after the neuron crosses a given peak potential.

As an tradeoff to reduce complexity, the accuracy with which the model reproduces electrophysiological measurements is sacrificed. However, due to the rather stereotyped shape of the action potential, it is unlikely that information transmission depends on its specific shape, but rather on its timing or frequency. Therefore, these models serve as an excellent tool to model spiking events and are much easier to analyze than complex biophysical models. In fact, since the outbreak of computer driven simulations, their elegance and simplicity has make them a widely used tool in the study of principles of neuronal information processing: the simplest LIF model is still the most popular of the *integrate-and-fire* family, but nonlinear models, such as the exponential-integrate-and-fire (EIF) (Fourcaud-Trocmé et al., 2003) and the quadratic-integrate-and-fire (QIF) (Ermentrout and Kopell, 1986; Ermentrout, 1996) models are often considered as they better reproduce the spiking onset. The choice of the model rests upon the specific system we are willing to study, and what questions are we seeking to answer. For a thorough analysis on the dynamical properties of a great variety of spiking neuron models see Izhikevich (2007).

Yet, the outstanding number of neurons present in any small piece of cortex makes the brain one of the most complex systems ever studied. Even if we considered the simplest phenomenological model neuron, and without taking into account any complex network structure, a simple model of the brain would consist on a system of approximately $86 \times 10^9$ differential equations –each describing the dynamics of a single neuron. Any mathematical study involving so many differential equations is generally unfeasible, unless a proper reduction in dimensionality is done.

Practical matters aside, fundamental reasons concerning the statistical nature of neuronal populations (Cragg and Temperley, 1954), alongside other information theory-based hypothesis, suggested that collective, rather than single neuron dynamics, were more relevant in the information processing happening in the brain. With this paradigm in mind, models of population average activity started to appear, first in the 1950's by the hands of Beurle (1956), and later in the 1960's by Griffith (1963). They developed the first continuum approximations of neuronal activity by making some statistical assumptions, following a methodology closely related to that used in statistical physics and thermodynamics. The aim was to create low dimensional models capable of capturing the collective properties of neural populations, yet simple enough to provide a mathematically tractable framework for their study.

In parallel, the rapid progress made in experimental neuroscience with

studies such as those carried out by Mountcastle, and Hubel and Wiesel in the somatosensory and visual cortex of cats and monkeys (Mountcastle, 1957; Hubel and Wiesel, 1962, 1968), gave support to the original hypothesis of Beurle. Moreover, in the early 1960's the first attempts to account for physiologically measurable phenomena in terms of the modeled properties of population of neurons were held by Freeman (1964). During the 1970's all these accumulation of experimental evidence inspired the work of many researchers, including Wilson and Cowan (1972, 1973), Knight (1972) and Amari (1972, 1974, 1977) among others, towards the development of population models, also known as *neural mass* models or *firing rate* models.

## Looking at the whole picture from a low-dimensional perspective: Population models

Population models were quickly accepted as valid descriptions of neuronal activity due to the increasing popularity of the rate and population code* hypothesis—which assumes information is transmitted as the average activity of neurons and not by their individual spiking times (known as the time code hypothesis)—, plus the empirical evidence that pointed towards the existence of large redundancy among neural populations. Moreover, many brain measurement techniques, such as electroencephalography (EEG) and functional magnetic resonance imaging (fMRI), provide measures of neural activity averaged over relatively large areas of the cortex. All that made firing-rate-based population models very useful tools not only as a theoretical construct but also as an experimental modeling tool (Destexhe and Sejnowski, 2009).

Among the various firing rate (FR) models developed in the 1970's, the Wilson and Cowan (WC) model (Wilson and Cowan, 1972) is probably the most popular one due to its simplicity and versatility. It typically consists on an a set of two ODEs describing the time evolution of the activity of spatially lumped excitatory and inhibitory neural populations, measured as the fraction of active neurons in each population. Such activity is defined as the number of spikes per unit time, i.e. the firing rate.

*Although both, rate and population code hypothesis, lie on the average activity of neurons, the former refers to the temporal average of spikes, while the latter refers to the population average. In an ergodic system, both hypothesis should be equivalent, however many neural systems show fast dynamics where the ergodic assumption is not likely to stand.

During the last 46 years, the WC model has been adapted or extended to account for different network configurations and to include a variety of physiologically relevant elements (see Destexhe and Sejnowski, 2009). Moreover, it is used not only to model population of neurons but also averaged activities of single neurons (measured as trial-to-trial averages) (e.g. Grossberg, 1973). However, these rate models are generally treated as 'ad hoc' models as they are not derived from the dynamics of the microscopic elements that constitute the studied systems: the neurons. In other words, the derivation of rate equations does not consist on a proper reduction of the microscopic neural system. Moreover, traditional firing rate models assume microstates where neurons' activity is fully or highly uncorrelated in order to simplify their mathematical expressions. Therefore they usually fail to describe any dynamical phenomena occurring as a consequence of synchronous firing.

### Neural field models

Space dependent firing rate models, also known as **neural fields** models (NFMs), are extensions of the localized firing rate models to continuously distributed populations of interacting excitatory and inhibitory neurons arranged according to some network topology. In such cases, the model usually appears as a set of partial differential equations, where the activity of the neuronal population and the interactions are space dependent functions. Due to the spatial arrangement of the neurons in the brain, they constitute the natural extension of the simpler localized population models. The commonly used formulation for NFMs is still that of the first models of the 1970s. It is common to indistinctly refer to firing rate and to neural field models just as Wilson-Cowan models. Indeed, the difference between both representations resides on the spatial dependence of the macroscopic magnitudes appearing in the equations. Therefore, their derivation is essentially identical and is based on the same statistical assumptions and simplifications (Bressloff, 2012; Ermentrout, 1998). In section 1.1 we formally present the WC model and briefly review the main assumptions done in its derivation.

Traditional NFMs generally appear in the form of continuous, first-order integro-differential equations (Wilson and Cowan, 1973; Amari, 1977), greatly facilitating the computational and mathematical analysis of the dynamics of large networks of spiking neurons. They have proven to be remarkably accurate in capturing a wide variety of the qualitative spatiotemporal dynamics observed in networks of asynchronously spiking neurons

(Latham et al., 2000; Shriki et al., 2003; Roxin et al., 2005). For example, the WC model is known to capture oscillatory dynamics arising in networks of excitatory and inhibitory neurons having different temporal dynamics. Moreover, when the pattern of synaptic connectivity depends on the distance between neurons, these differences can also lead to more complex spatiotemporal dynamics, including spatially and temporally periodic patterns, localized regions of high activity (bump and multi-bump states) and travelling waves such as fronts, pulses, target waves and spirals, (see (Coombes et al., 2003; Coombes, 2010; Ermentrout, 1998) for extensive reviews on the matter).

It is precisely their capability of displaying such rich repertoire of dynamics together with their mathematical simplicity that has make them so popular among neuroscientists. As such, they have been broadly used to model a variety of phenomena, including electroencephalogram (EEG) and magnetoencephalogram (MEG) rhythms (Jirsa et al., 2001, 2002; Liley et al., 2002; Nunez and Srinivasan, 2009), geometric visual hallucinations (Bressloff et al., 2001; Ermentrout and Cowan, 1979; Tass, 1995), short term memory (Laing and Troy, 2003; Laing et al., 2002; Nykamp et al., 2017), feature selectivity (Ben-Yishai et al., 1995; Hansel and Sompolinsky, 1998), motion perception (Giese, 1999), binocular rivalry (Kilpatrick and Bressloff, 2010; Bressloff and Webber, 2012), or the head direction system (Zhang, 1996).

However, neural field models are subject to the same assumptions and simplifications as their localized firing rate versions. Thus, they do not represent proper mathematical reductions of the original network of spiking neurons, but rather are heuristic. Similarly, their derivation assumes completely uncorrelated activity among neurons. Therefore, it is well known that traditional NFMs fail in capturing dynamics that arise as a consequence of the synchronous spiking of neurons (see e.g. Schaffer et al., 2013).

On the other hand, a great deal of experimental observations indicate that synchronous activity is common in brain tissue, and that the interplay between excitatory and inhibitory interactions alongside with synchronous activity may be responsible of generating complex spatiotemporal dynamics in networks of neurons (Whittington et al., 1995, 2000; Bennett and Zukin, 2004; Bartos et al., 2007; Whittington et al., 2011). Particularly, it has been shown that the population activity responds to big and rapid changes in the input currents in a relatively fast manner. This observations have been reported in studies dealing with spiking neural networks and supported by experimental data obtained *in vitro* preparations (see e.g Gerstner, 2000;

Brunel et al., 2001; Silberberg et al., 2004; Naud and Gerstner, 2012). It is therefore natural to ask, whether considering correlated activity of neurons, and therefore the possibility of generating synchronous activity, will modify and/or expand the dynamical repertoire shown by traditional NFMs.

## Objectives

Our aim is to explore this apparent discrepancy between traditional NFMs and their equivalent networks of spiking neurons, and assess the impact that synchronous activity may have in shaping the spatiotemporal patterns displayed by such networks.

In Chapter I we first explore the basic spatiotemporal dynamics described by traditional (or heuristic) neural field models, in terms of the fundamental mechanisms that give place to the different patterns observed. Next, we compare them with those observed in equivalent networks of spiking neurons. We observe that spiking neural networks display a variety of synchrony-related macroscopic patterns that are not captured by their counterpart population models, unless additional elements are heuristically added to their mathematical description. Specifically, perturbations to the asynchronous state display transient oscillatory behaviors, which in the case of a spatially distributed networks strongly depend on the synaptic connectivity between individual neurons. In fact, we show that ring networks of spiking neurons display a number of discrete modes of oscillation, resembling those of a tense string. In addition, we observe that the stability of the asynchronous regimes in networks of excitatory and inhibitory neurons also depends on the synchronization of neurons, which under some circumstances may lead to persistent oscillatory states, that are not predicted by the stability analysis of neural field models.

In order to investigate and characterize these synchrony-based spatiotemporal patterns, in section 1.3 we present and review a recently published firing rate model for a globally coupled heterogeneous population of quadratic integrate-and-fire (QIF) neurons (Montbrió et al., 2015).

In Chapter II we apply the same method as in (Montbrió et al., 2015) to a spatially extended network of QIF neurons to include nonlocal, instantaneous interactions. The resulting neural field model (QIF-NFM) explicitly takes into account sub-threshold integration and is therefore capable of capturing dynamics arising due to synchronous spiking of neurons. We then are able to investigate the reported spatiotemporal patterns with the newly obtained neural field model by means of both linear and nonlinear stability analysis

of the spatially homogeneous state. We find that such oscillatory behavior is characterized by the presence of an infinite number of oscillation modes, linked to the Fourier components of the spatial pattern of the synaptic connections.

CHAPTER 1

# Neural field models and their failure to describe spike-synchrony

*"There cannot be a language more universal and more simple, more free from errors and from obscurities, that is to say more worthy to express the invariable relations of natural things"*

— Joseph Fourier, The Analytical Theory of Heat (1878)

## 1.1 Traditional neural field models

Since the appearance of the first computational models describing the dynamics of single neurons in the cortex, networks of large number of spiking neurons have been the natural benchmark model for studying the collective dynamics of cortical neurons. Their derivation includes the most important physiological elements, such as sub-threshold voltage dynamics, spiking, or discontinuous synaptic interactions. Thus, they are generally considered to be biologically realistic models, and have proved to be extremely useful in the qualitative study of many neuronal mechanisms. However, given the astonishing number of neurons found in any small region of the cortex, network models are generally unpractical and time consuming. Furthermore, their complexity makes any analytical treatment unfeasible without a proper reduction in the dimensionality of their descriptions (Amit and Brunel, 1997;

Brunel and Hakim, 1999; Brunel, 2000; Brunel and Wang, 2003; Shriki et al., 2003).

This paradigm motivated many researchers to develop continuum theories of brain organization in an attempt to reduce the enormous complexity of neuronal interactions to simpler, macroscopic models that could become analytically tractable. The resulting mathematical models of cortical tissue are often referred to as **neural field** (NF) models, and they are generally presented as simple, phenomenological models of neuronal activity in the form of continuous, first-order differential equations (see e.g. Wilson and Cowan, 1973; Amari, 1977; Nunez, 1974; Ermentrout, 1998; Coombes, 2005; Bressloff, 2012; Coombes et al., 2014; Deco et al., 2008), which can be analyzed by means of standard techniques for differential equations. These models have shown qualitative agreement with their equivalent networks of spiking neurons, for a wide range of dynamical states (Latham et al., 2000; Shriki et al., 2003; Roxin et al., 2005). Specifically, they have proven to be remarkably accurate in capturing spatiotemporal patterns arising in networks of interacting excitatory and inhibitory neurons (Amari, 1977; Ermentrout and McLeod, 1993; Pinto and Ermentrout, 2001a,b).

However, their derivation follows an heuristic approach based on statistical assumptions, rather than on the specific dynamics of single neurons, and therefore it is generally difficult to quantitatively relate their dynamics with the specific details of their representative microscopic state. Particularly, neural field models are derived assuming that the macroscopic state only depends on the all-or-none spiking mediated interactions between neurons. Therefore, among all the dynamics displayed by a single neuron, the only element that is taken into account is the spike, thus ignoring all sub-threshold dynamics occurring in between the spikes. Indeed, this assumption implicitly ignores any existing correlations between neural spikes which should be duly tracked by the precise way in which the membrane potential evolves between spikes. In other words, tracking the sub-threshold dynamics is necessary to preserve the correlations that may arise through the network.

In order to better understand the concepts above, we now present the Wilson and Cowan (1972) model and its spatially extended version (Wilson and Cowan, 1973), often considered as the canonical neural field model. We will be referring to these traditional models as the *heuristic neural field models* (H-NFMs), or simply the WC model, to distinguish them from the firing rate equations we will present in Section 1.3. The simplest form of the WC equations describes the activity of the interacting excitatory (e) and

inhibitory (i) sub-populations in terms of their respective firing rates, $R_\alpha$ ($\alpha = e, i$):

$$\tau_e \frac{dR_e}{dt} = -R_e + \Phi\left(\tau_e J_{ee} R_e - \tau_e J_{ie} R_i + \bar{\eta}_e + P_e(t)\right), \tag{1.1a}$$

$$\tau_i \frac{dR_i}{dt} = -R_i + \Phi\left(\tau_i J_{ei} R_e - \tau_i J_{ii} R_i + \bar{\eta}_i + P_i(t)\right), \tag{1.1b}$$

where $\Phi(I)$ is the steady-state current-to-rate transfer function (also known as f-$I$ function), which models the response of the population to input currents $I$. It typically consists of a sigmoid function that provides a phenomenological description of the level of activity of a population of neurons with thresholds distributed according to a unimodal distribution. As such, the f-I curve can be seen as a cumulative distribution function of the inputs received by neurons. Both neuronal sub-populations, $\alpha = e, i$, receive synaptic inputs from neurons in the $\beta = e, i$ sub-population with synaptic weights $J_{\alpha\beta}$. Similarly, each sub-population receives external inputs, $\bar{\eta}_\alpha + P_\alpha(t)$, where we distinguish between constant and time-varying inputs. Finally, $\tau_\alpha$ is a time constant determining the temporal scale of the dynamics of each sub-population. Due to the heuristic nature of the WC equation, the choice of the time constant is somehow arbitrary, as we will see next. A schematic representation of this set up can be seen in Fig. 1.1(a) on page 14, where two coupled "cortical units" (gray background) are depicted. The dynamics of each uncoupled cortical unit (**1, 2**) would obey Eqs. (1.1).

A quick revision to the seminal work of Wilson and Cowan (1972) reveals the assumptions made for obtaining this type of firing rate equations:

i) The heterogeneity of neuronal population, modeled as the distribution of a given microscopic neuronal parameter, is generally averaged out to a single macroscopic variable. In their paper, the mean field approach reduces the initial distribution of membrane potentials to the neuronal response function $\Phi$. This assumption only takes into account the first passage time of neurons through the threshold potential, that once averaged over the whole membrane potential distribution, provides a measure of the population firing rate. However, this assumption is ignoring any dynamical effects that higher moments of the distribution may have over the macroscopic dynamics (Cowan, 2014).

ii) Similarly, correlations between the level of excitation of a cell and the probability that the cell is sensitive are assumed to be negligible.

iii) Probably, the most famous simplification is that of the *time coarse graining*: by considering that synaptic activation behaves as a low-pass filter, the authors reduce the temporal integrals to time-averaged quantities, thus simplifying the original system composed of a couple of integrodifferential equations to Eqs. (1.1). This smooths out fast transients occurring due to synaptic dynamics and makes difficult to interpret the temporal scale of the equations. Often this last step is not applied, and instead, the temporal integral is written in the form of a differential equation* which accounts for the dynamics of the synapses. However, the system becomes at least 4-dimensional and consequently harder to mathematically analyze.

In this chapter we will explore the consequences that the first two assumptions may have in the macroscopic dynamics of neuronal populations. The resulting firing rate model corresponds to a system in which the activity of neurons is uncorrelated, and is sometimes taken as a macroscopic description in the limit of asynchronous activity. Furthermore, these assumptions are probably the reason why Eqs. (1.1) are only expressed in terms of the average firing rate, and not in terms of any other macroscopic magnitude related to the membrane potentials of neurons.

Notice that, after the third simplification is considered, the resulting time constant $\tau_\alpha$ could be interpreted either as the membrane time constant or the synaptic time constant. By assuming instantaneous synapses, one can fairly interpret $\tau_\alpha$ to be the membrane time constant.

The above equations (1.1) describe the dynamics of local populations of neurons, the purpose of which is to model neural ensembles containing similar type of neurons located at specific places of the brain, for instance at the different layers of cortical columns. However, a great deal of electrophysiological and anatomical data indicate that the cerebral cortex is spatially and functionally organized (see, for example Mountcastle, 1997; Martin, 1988; Lund et al., 2003; Lodato and Arlotta, 2015). Therefore neural field models represent the natural extension of Eqs. (1.1) where neuronal interactions, and consequently the activity of the neurons, are spatially dependent. They typically consist on a couple of partial integrodifferential equations describing the temporal and spatially dependent activity of populations of excitatory and inhibitory neurons. However, analytically dealing with partial

*A general model of synaptic kinetics is the alpha function, which accounts for both rise and decay of synaptic activation described by a second order ODE, with different time constants for each process.

differential equations is generally difficult and a common simplification comes from assuming spatially dependent global connectivity. That is, by considering nonlocal coupling, one can write the spatial interactions as a global mean field, removing the spatial derivatives from the equations. The connectivity then is a function of the distance between neurons, rather than the position of neurons. Notwithstanding, such systems retain the majority of the dynamics shown by their counterpart localized versions (Roxin et al., 2005; Roxin and Montbrió, 2011; Martí and Rinzel, 2013).

The resulting ordinary integrodifferential system is* (Ermentrout and Cowan, 1980):

$$\tau_e \frac{\partial R_e}{\partial t} = -R_e + \Phi_e \Bigg[ \tau_e \int_\Omega \big[ J_{ee}\left(|x-y|\right) R_e\left(y,t\right) - J_{ie}\left(|x-y|\right) R_i\left(y,t\right) \big] dy + \bar{\eta}_e + P_e(x,t) \Bigg], \tag{1.2a}$$

$$\tau_i \frac{\partial R_i}{\partial t} = -R_i + \Phi_i \Bigg[ \tau_i \int_\Omega \big[ J_{ei}\left(|x-y|\right) R_e\left(y,t\right) - J_{ii}\left(|x-y|\right) R_i\left(y,t\right) \big] dy + \bar{\eta}_i + P_i(x,t) \Bigg]. \tag{1.2b}$$

These equations differ from the localized E-I model (1.1) in that variables are now space dependent, and that the synaptic activation is now represented in terms of an integral (or a spatial convolution) where the functions $J_{\alpha\beta}\left|x-y\right|$ describe the weight of all synapses from cells of the $\alpha$th population to the $\beta$th population a distance $|x-y|$ away. Here the populations are arranged in one dimension on a domain $\Omega$. All the other elements follow the same interpretation as in (1.1). The simplest one-dimensional topology is given by a ring network, which eliminates boundary conditions. The expansion from the localized E-I network (1.1) to a ring neural field network is schematically represented in Fig. 1.1(a,b) on the next page, top panels. Panel (a) shows a pair of cortical columns, each modeled according to Eqs. (1.1) and coupled via inhibitory synaptic connections. The ring network in panel (b) can be thought as the succession of several of those cortical columns where the synaptic projections connect all columns following a specific connectivity kernel.

*To facilitate the notation we have avoided explicitly writing the dependence of the variables on $x$ and $t$; $R_\alpha = R_\alpha\left(x,t\right)$.

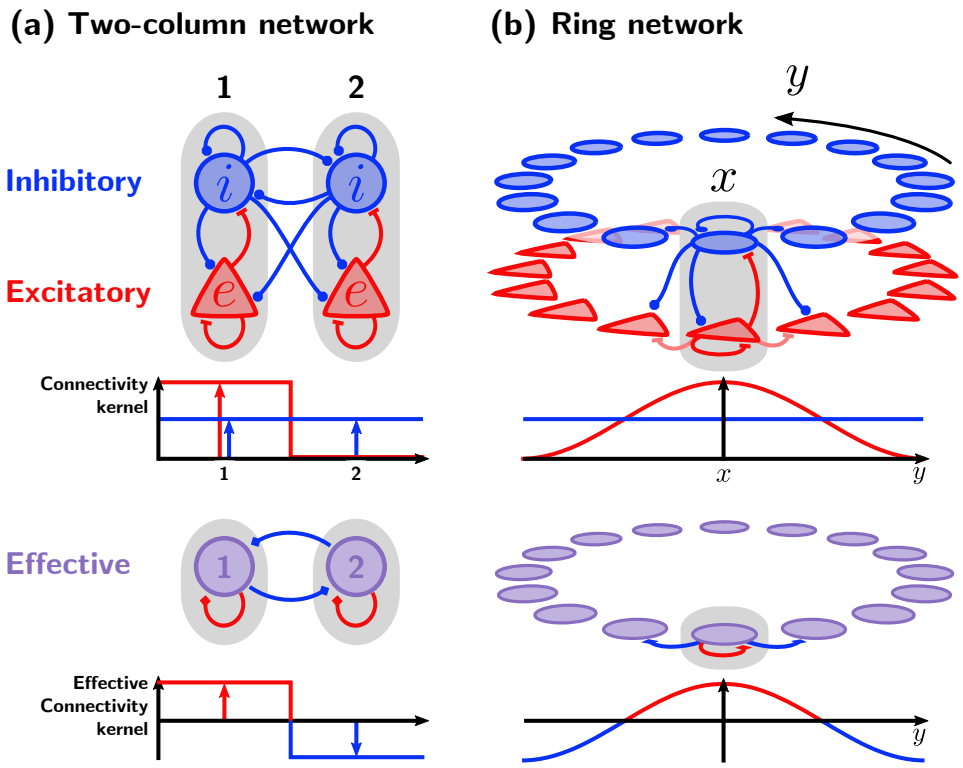


**Figure 1.1:** Network diagrams representing cortical columns (gray area), each composed of an excitatory and an inhibitory pull of neurons. In panel (a), an example network containing two cortical columns is shown, while in panel (b), the extension to a continuum ring of the previous network is schematically depicted. Top diagrams correspond to the full network [Eqs.(1.1) and (1.2)], containing separated ensembles of excitatory and inhibitory neurons, whereas in the bottom panels the equivalent effective model (Eq. (1.3) for the ring model) is shown. The connectivity kernels located under each network diagram represent the homologous profiles for each system, i.e. both represent local excitation and global inhibition.

The interpretation given so far considers the neural field as a continuous sequence of spatially connected "cortical columns" (Wilson and Cowan, 1973; Amari, 1977; Coombes, 2005; Coombes et al., 2014). Nevertheless, an alternative interpretation in which individual neurons are distributed according to the variable $x$ is also possible, for example to model feature selectivity (Ben-Yishai et al., 1995; Hansel and Sompolinsky, 1998; Roxin et al., 2005; Roxin and Montbrió, 2011) or networks with arbitrary degree distributions (Nykamp et al., 2017).

### Effective model

A general analysis of Eqs. (1.2) is technically difficult even though it is the natural extension to the previously presented firing rate equations (1.1). With that goal in mind—but out of the scope of this thesis—-, we first study the dynamics of the simplified **effective model**. By assuming that the excitatory and the inhibitory neurons/populations follow the same dynamics, i.e. $\tau_e = \tau_i = \tau_m$, $J_{ee} = J_{ei} = J_e$, $J_{ii} = J_{ie} = J_i$, $\Phi_e = \Phi_i = \Phi$, $\bar{\eta}_e = \bar{\eta}_i = \bar{\eta}$, then $R_e = R_i = R$ and Eqs. (1.2) become:

$$\tau_m \frac{\partial R}{\partial t} = -R + \Phi\left[\frac{\tau_m}{2\pi}\int_{-\pi}^{\pi} J\left(|x-y|\right) R\left(y,t\right) dy + \bar{\eta} + P(x,t)\right], \tag{1.3}$$

H-NFM

where the synaptic connectivity kernel, $J$, is the combination of the excitatory and the inhibitory contributions, $J(x) = J_e\left(|x|\right) - J_i\left(|x|\right)$, and therefore represents an effective mixed coupling which may have both positive and negative regions (see the effective connectivity kernels in Fig. 1.1). Note that the effective model assumes that any perturbations, $P_\alpha$, applied on the full model (1.2) obey $P_e = P_i = P$, such that the activity of both sub-populations remains equal at any time. Finally, we have consider the simplest one-dimensional topology: the ring network of length $2\pi$, i.e. $x \in [-\pi, \pi)$. Fig. 1.1 shows schematic representations of the network for the different conceptual stages between the two-column paradigm and the effective ring network described by Eq. (1.3). The effective networks in the lower diagrams (in purple) represent simplified versions of their counterpart full models in the top diagrams (blue circles and red triangles).

The transition from the discrete two-column model in Fig. 1.1(a) to the continuous ring model in Fig. 1.1(b) is further emphasized by the shape of the connectivity kernels in each case. The connectivity profile in Fig. 1.1(d) follows a simple cosine function, $J(x) = J_0 + J_1\cos(x)$ with $J_0 = 0$, but a more general connectivity may be applied by considering a general cosine series (symmetric Fourier series)

$$J\left(x\right) = J_0 + 2\sum_K J_K \cos(Kx), \quad K \in \mathbb{Z}. \tag{1.4}$$

The choice of the connectivity coefficients $J_K$ generally follows physiological assumptions and is therefore sensitive to the particular network in mind.

In the next section we review some of the spatiotemporal patterns arising in such networks for different connectivity profiles. But first, we explore the possible dynamics offered by Eq. (1.3) by analyzing the linear stability of the fixed points.

If we consider the general connectivity kernel (1.4), Eq. (1.3) admits two families of spatial solutions. On one hand, at the spatially homogeneous state (SHS) the activity of the network is flat $R(x,t) = R(t)$, and the spatial convolution corresponding to the synaptic activation is just $\tau_m J_0 R(t)$. The resulting state is thus equivalent to that obtained for each sub-population equation, (1.1a) or (1.1b), when the cross couplings vanish, $J_{\alpha\beta} = 0$ ($\alpha \neq \beta$). That is, it corresponds to the WC equation of a single recurrently coupled population that we write here for future reference:

$$\tau_m \frac{dR}{dt} = -R + \Phi(I), \tag{1.5}$$

Therefore, the SHS is given by

$$R_* = \Phi(\tau_m J_0 R_* + \bar{\eta}), \tag{1.6}$$

where $R(x,t) = R_*$. Although the resulting fixed point is equivalent to that of a single excitatory ($J_0 > 0$) or inhibitory ($J_0 < 0$) population, the stability, and by extension, the response of the system may depend on higher order Fourier coefficients. Indeed, with the ansatz

$$R(x,t) = R_* + \sum_{K=0}^{\infty} \varepsilon_K e^{iKx + \lambda_K t}, \tag{1.7}$$

with $\varepsilon_K \ll 1$, we obtain the following real-valued eigenvalues

$$\lambda_K = -\frac{1}{\tau_m} + J_K \Phi'_*, \tag{1.8}$$

where the slope $\Phi'_*$ is evaluated at the fixed point (1.6), and is a positive function provided the transfer function is an increasing function. The SHS will destabilize ($\lambda_K > 0$) via a pattern-forming (Turing) bifurcation at a critical value of the connectivity mode $J_K^c$. Yet, the response of the stable SHS, i.e. with $\lambda_K < 0$, to perturbations of wavenumber $K$ will always follow an exponential relaxation with a characteristic time constant proportional to the corresponding value of the connectivity mode $J_K$, as shown in Fig. 1.2(a); the larger the value of the connectivity the longer it takes

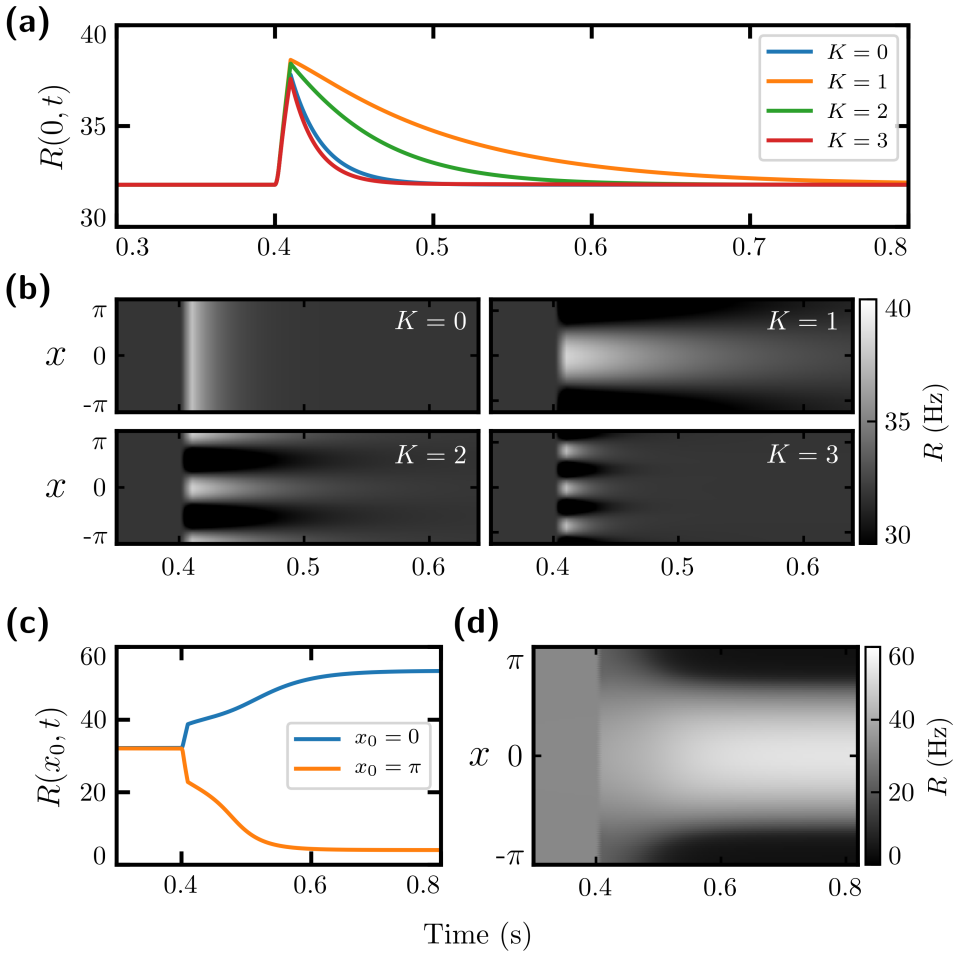


**Figure 1.2:** Time series of the H-NFM (1.3) corresponding to the SHS ($J_1 = 10$), and to the bump state ($J_1 = 14$). Panel (a) shows time series corresponding to the position $x = 0$ of the response of the system to a brief spatially modulated perturbation of wavenumber $K = 0, 1, 2, 3$ applied at $t = 0.4$ s. In panel (b) the same simulations are plotted in a space-time representation. Panels (c) and (d) show the transition from the unstable HS to the BS. Parameters: $\bar{\eta} = 4$, $\tau_m = 20$ ms, $J_K = 0$ for all $K \neq 1, 2, 3$; $J_2 = 7.5$, $J_3 = -2.5$. Eq. (A.1.4) was used for the transfer function $\Phi$. See Appendix 2.D for specifics related to the perturbation.

for the activity to decay to the equilibrium state. There, we used different values of the connectivity modes $K = 1, 2, 3$, such that perturbations of each mode exhibit different relaxation times. At the critical value $J_K^c$ the relaxation time approaches infinity indicating the bifurcation boundary. This dynamical property was in part used by Martí and Rinzel (2013) to model

feature categorization processes in the sensory areas of the brain.

The second family of spatial solutions arises at the Turing bifurcation. Above the critical value $J_K$, a spatially inhomogeneous pattern of activity arises consisting of $K$ equidistant bumps of activity. This is the so-called bump state (BS), depicted in Figs. 1.2(c) and (d) for $K = 1$. We skip further analysis of the inhomogeneous states. However, numerical simulations show that the bump state is stable and exhibits the same exponential relaxation process as the homogeneous state. We can conclude then, that even though the ring neural field model (1.6) actually combines the effects of excitatory and inhibitory neurons, such interactions are only manifested in the ability of generating bump states and in the different decaying times showed when perturbing the SHS.

In the following section we review some of the spatiotemporal patterns that can arise in similar neural field models when additional physiologically inspired elements are heuristically added to the dynamical equations. Specifically, we will show how these patterns are closely related to some fundamental mechanisms which are well known to generate oscillatory dynamics in neuronal networks.

### 1.1.1 Excitation-inhibition based spatiotemporal phenomena in NFM

A great deal of experimental evidence shows that any nervous process is dependent upon the interaction of both excitatory and inhibitory neurons. Such negative-positive interplay is known to produce a variety of spatiotemporal patterns which can be categorized into oscillatory behaviors, spatial patterns, and into dynamics which are a combination of the two.

In order to better understand the dynamical features shown by neural field models, we first focus on exploring the most simple mechanisms capable of generating oscillatory dynamics. Such mechanisms have been extensively studied after experimental observations done *in vivo*. Measures of local field potentials (LFP) in the hippocampus show prominent oscillations in the theta band (4-10 Hz) and the gamma band (30-80 Hz) (Buzsáki and Draguhn, 2004). Recent findings link them with tasks related to spatial navigation memory (Buzsáki and Moser, 2013), which have elicited major interest on understanding the origin and functional role of such oscillations.

Following a great deal of experimental research *in vitro* (Whittington et al., 1995; Fisahn et al., 1998; Whittington et al., 2011; Gloveli et al., 2010)

(see Bartos et al., 2007, for a review), gamma rhythms have been divided in two major categories: on one hand, oscillations generated in networks of only inhibitory neurons (interneuron), and on the other hand, those generated in networks composed of both inhibitory (i) and excitatory (e) (pyramidal) neurons. The first category is generally known as ING oscillations while the second can be divided between PING and PG (Persistent Gamma) oscillations. Notice that this categorization does not cover all oscillatory behavior in the brain, not even all Gamma oscillations, but we focus on ING and PING mechanisms because they involve networks motifs that are common throughout the cortex and the hippocampus.

#### 1.1.1.1 Interneuron Network Gamma (ING) oscillations

Although seemingly paradoxical, the simplest form of gamma generation is found in networks were the dynamics are driven exclusively by interneurons (inhibitory neurons). A positive drive is facilitated by external excitatory inputs, which alongside a delayed feedback inhibition (provided by recurrent synaptic connections), establish the typical excitatory-inhibitory loop necessary to produce robust oscillations. The mechanism, which is schematically depicted in Fig. 1.3(a), consists on an ensemble of recurrently coupled inhibitory (i) neurons subject to sufficiently strong excitatory external inputs $\bar{\eta}$. However, the precise way in which interneurons are recruited and generate the subsequent oscillations is not trivial.

First, we may ask what is the basic neuronal substrate necessary to hold such mechanism. This question has been theoretically addressed with different approaches, including extensive computational studies carried on in networks of spiking neurons (Wang and Buzsáki, 1996). Following those studies there is large consensus on the basic requirements needed to generate ING oscillations (Buzsáki and Wang, 2012):

1. Recurrent connection between inhibitory neurons, represented by the closed loop in Fig. 1.3(a).

2. A time constant, representing the synaptic transmission, which introduces an effective delay in the spread of inhibition.

3. High enough excitation (red input in Fig. 1.3(a)), sufficiently depolarizing interneurons such that they are able to fire at high enough rates.

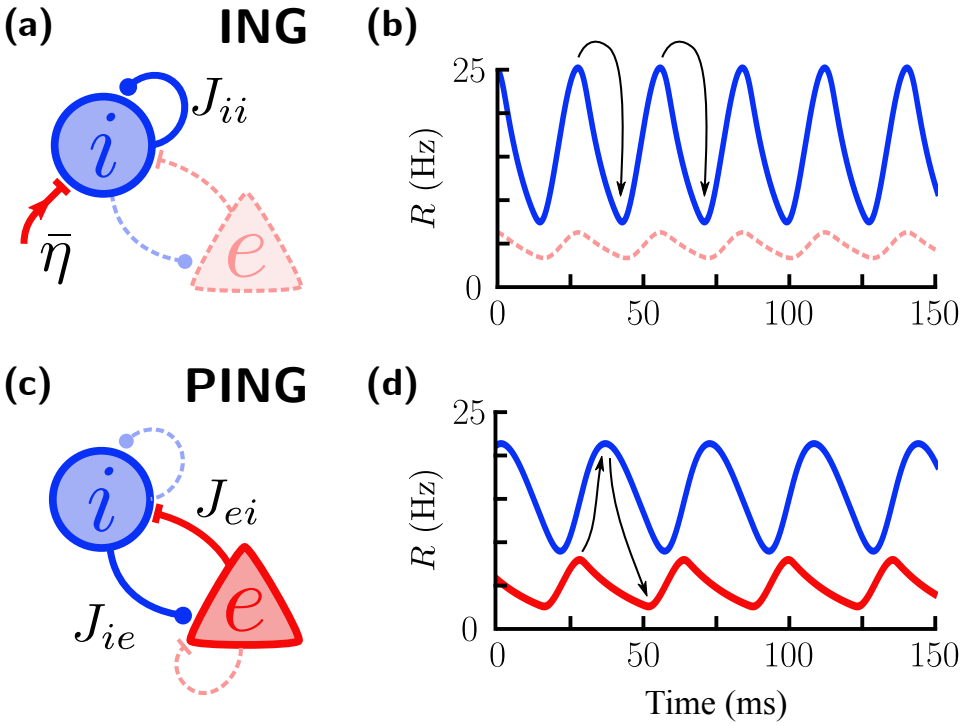


**Figure 1.3:** Schematic representation of interneuron network gamma (ING) and pyramidal interneuron network gamma (PING) mechanisms and their resulting oscillatory dynamics. In panels (a) and (c) blue circles and red triangles correspond to the inhibitory (i) and the excitatory (e) sub-populations, respectively. Accordingly, blue and red lines correspond to inhibitory and excitatory connections. The dashed (transparent) elements are not needed to generate the oscillations. *Top panels:* **ING** mechanism. **(a)** Minimal network for ING oscillations requires an inhibitory recurrently coupled population receiving external excitatory inputs, $\eta$. **(b)** Example of ING oscillations. Black arrows indicate the self-inhibition effect produced when the activity of the population is high, which is the origin of the oscillations. *Bottom panels:* **PING** mechanism. **(c)** Minimal network for PING oscillations requires a pair of cross-coupled excitatory and inhibitory populations. **(d)** As in (b), black arrows indicate the order in which each cycle is generated. Both time series were generated using WC model [Eq. (1.9)] with a time constant $\tau_m = 10$ ms, see Appendix A for details of the numerical simulations.

Synaptic kinetics are therefore key in generating these type of oscillations, and their time scale greatly determines the frequency of the macroscopic oscillations. Longer time constants will delay the inhibitory volley slowing the overall cycle, and therefore decreasing the frequency.

The ING mechanism has been thoroughly studied by means of simulations of networks of spiking neurons, and surprisingly, two very different microscopic scenarios were found compatible with the macroscopic oscillations:

1. On one hand, oscillations due to neural synchronization may arise when neurons have similar spiking frequencies. An initial group of neurons may start firing almost synchronously, increasing the activity of the population, which at the same time, inhibits the rest of the neurons and brings them closer to the group. After some time, a larger fraction of neurons will be firing synchronously, producing the macroscopic oscillations (Van Vreeswijk et al., 1994; Wang and Buzsáki, 1996). Therefore, in this situation large fractions of neurons become frequency-entrained, firing with frequencies equal or close to the macroscopic oscillation. This intuitive scenario is nonetheless fragile when heterogeneity in the population is sufficiently increased.

2. On the other hand, in a less intuitive scheme (Brunel and Hakim, 1999; Brunel and Wang, 2003) neurons receive stochastic inputs at large rates, resulting in a highly asynchronous state. When recurrent inhibition is powerful enough, single neurons fire at low rates despite the strong external excitatory inputs. Moreover, the E-I balanced current remains sub-threshold, not only maintaining neurons at low firing rates, but also facilitating a fluctuation-driven regime, therefore causing irregular firing. Yet, random fluctuations will eventually increase the activity, recruiting enough neurons to produce a a large inhibitory volley that will arrive after a brief period of time due to synaptic filtering, strongly hyperpolarizing neurons and dramatically lowering the activity of the population. Once the inhibition is shuttered, the population activity increases again and the cycle is repeated. In this situation, neurons fire at much lower frequencies than the population frequency and in a highly *irregular* fashion, as compared to the previous scenario where neurons fired *regularly* close to the population frequency.

These two variants are sometimes known as the *synchronous regular* and *synchronous irregular* ING mechanisms. Anyhow, the macroscopic behavior is caused by the synchronous firing of a fraction of the population, and macroscopic measures will, in most cases, look alike.

Note that, even though the ING mechanism only takes into account inhibitory neurons, in the brain interneurons are densely connected to pyramidal cells—-dashed elements in Fig. 1.3(a). Nevertheless, the ING mechanism is still relevant in networks where connections between pyramidal and interneuron cells are not affecting the overall macroscopic dynamics. Experimental results showed that in such networks, breaking the pyramidal-interneuron connections did not affect oscillatory activity, hence, proving pyramidal cells to be irrelevant in shaping macroscopic oscillations. Accordingly, the activity of the pyramidal sub-population in such situations is entirely dependent on the intrinsic activity of the inhibitory network, showing the same population frequency and nearly phase locked to it—-see Fig. 1.3(b).

ING oscillations can be described by means of the effective neural field model [Eq. (1.3)] if we take a flat inhibitory profile $J\left(|x|\right) = J_0 < 0$. Also, following the above requirements one must include an additional equation to model the synaptic kinetics, which is needed to effectively generate the temporal loop between excitation and inhibition. The resulting neural field description is equivalent to the single population description (1.5) with $J_0 < 0$ plus a synaptic equation, and takes the form (Wilson and Cowan, 1972; Cowan, 2014):

$$\tau_m \frac{dR}{dt} = -R + \Phi\left(\tau_m J_0 S + \bar{\eta} + P(t)\right), \tag{1.9a}$$

$$\tau_d \frac{dS}{dt} = -S + R, \tag{1.9b}$$

where again, $-\tau_m J_0 S$ accounts for the recurrent inhibitory connections and $S$ and $J_0 < 0$ being the synaptic activation and the synaptic strength, respectively. Finally, $\tau_d$ is the synaptic time constant (Ledoux and Brunel, 2011; Keeley et al., 2017).

Eqs. (1.9) meet all the requirements of a typical network exhibiting ING oscillations. Nevertheless, as we can prove by a linear stability analysis, Eqs. (1.9) cannot generate sustained oscillations. The fixed point is given by the expression

$$R_* = \Phi\left(\tau_m J_0 S_*\right), \quad S_* = R_*, \tag{1.10}$$

that has a single solution provided $J_0 \leq 0$. The eigenvalues associated to the fixed point (1.10) are

$$\lambda_\pm = -A\left[1 \pm \sqrt{1 - B}\right], \tag{1.11}$$

with

$$A = \frac{\tau_m + \tau_d}{2\tau_m\tau_d}, \quad B = \frac{4\tau_m\tau_d}{(\tau_m + \tau_d)^2}\left(1 - \tau_m J_0 \Phi'_*\right).$$

$\Phi'_*$ is the derivative of the transfer function at the fixed point, and as we may recall, is always a positive function provided $\Phi$ is an increasing function, and thus $B > 0$. Therefore, the real part of the eigenvalues is always negative, and accordingly, the fixed point is either a stable node ($B < 1$) or a stable focus ($B > 1$). For sufficiently large inhibition, the stable node becomes a focus and therefore the system exhibits damped oscillations when a perturbation is applied, as shown in Fig. 1.4(a).

**Adding time delays:** the equation (1.9b), describing synaptic kinetics, introduces the necessary feedback mechanism into the WC equation (1.9a), but something else is needed to account for the effective time delay necessary to generate the oscillations. In order to obtain persistent oscillatory dynamics, an explicit fixed time delay is introduced in Eq. (1.9) as a heuristic proxy for the combined effects of synaptic and sub-threshold integration (Roxin et al., 2005; Roxin and Montbrió, 2011; Brunel and Hakim, 2008; Keeley et al., 2017). The resulting equations are:

$$\tau_m \frac{dR}{dt} = -R + \Phi\left(\tau_m J_0 S + \bar{\eta} + P(t)\right), \tag{1.12a}$$

$$\tau_d \frac{dS}{dt} = -S(t) + R(t - D), \tag{1.12b}$$

with $D > 0$ representing the effective delay. Actually, the synaptic equation (1.12b) is no longer necessary and one can get rid of it by taking the limit of fast synapses, $\tau_d \to 0$, thus reducing the above equations (1.12) to a single equation **heuristically** describing ING oscillations (H-ING),

$$\tau_m \frac{dR}{dt} = -R + \Phi\left(\tau_m J_0 R(t - D) + \bar{\eta} + P(t)\right). \tag{1.13}$$

H-ING

The above equation is infinite dimensional and is not easy to study. Moreover, it can be prove that the system is formally equivalent to the H-NFM (1.5) with $n$th order synapses, at the limit $n \to \infty$.

Also, it can be prove that the period of the oscillations is between four times and two times the delay, depending on whether the delays are small or large (Roxin et al., 2005; Roxin and Montbrió, 2011; Brunel and Hakim,

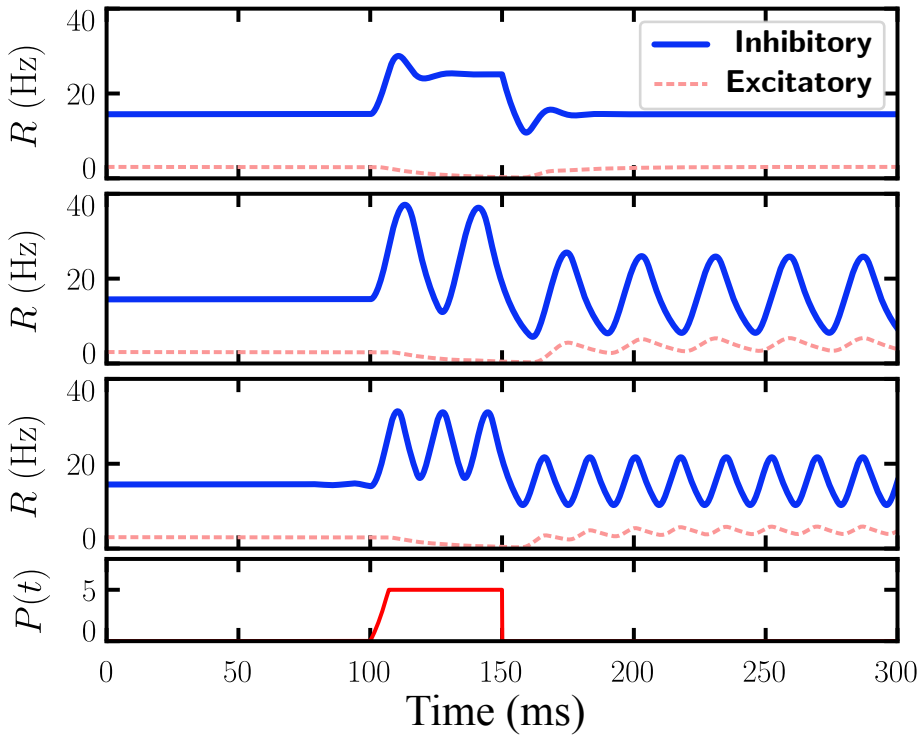


**Figure 1.4:** Time series of the H-NFMs for different synaptic configurations showing the response of the system to the transient step current in panel (d). The dashed line corresponds to the excitatory sub-population's activity that is driven by the inhibitory one. **(a)** H-NFM with synaptic kinetics [Eqs. (1.9)]. **(b)** with both synaptic kinetics and delay [Eqs. (1.12)]. **(c)** with delay [Eq. (1.13)]. In panels (b) and (c) the system starts at an unstable fixed point. Parameters: $\bar{\eta}_i = 8$, $\bar{\eta}_e = 5$, $J_{ii} = 45$, $J_{ie} = 15$, $\tau_m = 10$ ms. For panels (a) and (b): $\tau_{d,i} = 5$ ms, $\tau_{d,e} = 2$ ms. For panels (b) and (c): $D = 5$ ms. In all cases we used the transfer function, $\Phi$, of a LIF population (A.1.4).

2008). It is worth mentioning that we could also perform the limit of slow synapses of equation (1.12) (see section 1.3.5.1) obtaining a similar expression for the synaptic activation:

$$\tau_d \frac{dS}{dt} = -S + \Phi\left(\tau_m J_0 S(t-D) + \bar{\eta} + P(t)\right). \tag{1.14}$$

Finally, an example of the oscillatory dynamics generated by Eqs. (1.12) and Eq. (1.13) is shown in Fig. 1.3(b), where we used the f-I curve, $\Phi$, of a LIF population [Eq. (A.1.4)] with the diffusion coefficient $\sigma = 1$. The

inclusion of synaptic kinetics modifies the frequency of the oscillations since its directly affecting the recurrent inhibitory feedback, thus effectively slowing the overall dynamics and decreasing the frequency. In Fig. 1.4 a comparison between the three versions of the H-NFM is shown, i.e. only with synaptic kinetics (1.9), with synaptic kinetics and delays (1.12), and only with delays (1.13). In all three cases, a perturbation $P(t)$ of duration $0.05$ s was applied at $0.1$ s. Note that, in the second and third case the system is set in an unstable state, which explains the small fluctuations in the third plot that arise just before the perturbation is applied.

So far we have seen that the H-NFM needs the introduction of a delay parameter in order to successfully describe ING oscillations. Next, we discuss the other oscillatory mechanism, i.e. the PING mechanism, and its representation in the neural field model.

#### 1.1.1.2 Pyramidal Interneuron Network Gamma (PING) oscillations

In contrast to ING oscillations, there are situations in which the removal of pyramidal to interneuron connections do actually affect the oscillatory dynamics of the network (Roberts et al., 2013). The study of oscillations in reciprocally connected E-I networks goes back to the 1970s (Wilson and Cowan, 1972; Nunez, 1974). In a way, they represent a much more intuitive oscillatory mechanism, since the excitation (positive) and inhibition (negative) drives appear explicitly in the model. The PING cycle [Fig. 1.3(c) and (d)] starts with a strong input driving excitatory cells to fire. A large enough recruitment of pyramidal cells sends an excitatory volley to the interneurons, producing a sudden increase of their activity. The interneuron-pyramidal connections facilitate the rapid inhibition of the excitatory sub-population which strongly depolarizes the neurons, and thus, interrupts the excitation of the inhibitory sub-population. Consequently, the activity of inhibitory neurons falls dramatically, allowing the excitatory sub-population to *recover* and to repeat the cycle one more time.

Once again, the precise way in which the recruitment and recovering processes are done is not unique. Similar to ING oscillations, the E-I mechanisms can also exhibit two distinct regimes, depending on the regularity of the spikes of single neurons (Wang and Buzsáki, 1996; Brunel and Wang, 2003). In any case, the recruiting process of excitatory neurons is thought to occur synchronously, eliciting many simultaneous spikes that contribute to increase the activity of the excitatory sub-population. Additionally, *in vitro* experiments (Kopell et al., 2010; Whittington et al., 2011) show that

oscillations are short lived and that both, pyramidal neurons and interneurons, present high spike rates. Moreover, experiments conducted in *in vivo* (Tiesinga and Sejnowski, 2009; Buzsáki and Wang, 2012) revealed that cells fired at approximately the same frequency as the population oscillations, and that pyramidal cells were firing just before the interneurons, as it is expected to happen in this mechanism.

The robustness of PING oscillations critically depends on the mean E-I ratio (Buia and Tiesinga, 2006; Tiesinga and Sejnowski, 2009, 2010; Brunel and Wang, 2003), which modulates the synchronicity in the network. Generally speaking, the principle of fast excitation versus slow inhibition must hold, which means that increasing the inhibitory feedback—-for example, by strengthening the interneuron to pyramidal couplings—-may destroy synchrony. Note that an increase in the inhibitory feedback results in a decrease in the activity of the excitatory sub-population, which reduces the frequency of the excitatory neurons, and thus effectively slows down the excitatory sub-population. In contrast, when the E-I ratio is sufficiently increased, synchronization emerges spontaneously out of the asynchronous regime and neurons lock to the macroscopic oscillations.

The minimal network configuration of the PING mechanism is schematically depicted in Fig. 1.3(c). Its description requires explicitly differentiating between the excitatory and the inhibitory sub-populations, as they both receive different mean synaptic inputs. In other words, in order to have the E-I feedback loop it is necessary to have a system were one sub-population is sending excitatory inputs to a second sub-population while the latter sends inhibitory inputs back to the former. As such the **effective model** shown at the bottom panel of Fig. 1.1(b) cannot account for PING oscillations because both populations are identical and receive the same excitatory or inhibitory synaptic input. Similarly, the effective neural field model (1.3) does not meet the aforementioned requirements. Therefore, we do not expect those effective models to produce PING oscillations, but rather a different type of patterns. Namely, the particular network architecture shown in Fig. 1.1 produces the so-called winner-take-all (WTA) pattern that we will discuss in the next section.

Nonetheless, imposing different temporal dynamics to the excitatory and to the inhibitory neurons in the full model (1.2), by either considering different time scales, $\tau_e < \tau_i$, or different input currents, $\bar{\eta}_e > \bar{\eta}_i$, we can also obtain PING oscillations. Next, we briefly study the conditions in which such oscillations arise so that we may compare them with the results obtained

from networks of spiking neurons that we will present later in this chapter. For the sake of simplicity we only analyze the stability of the spatially homogeneous state (SHS) and therefore we consider the equivalent two sub-population system (1.1) which contemplates four synaptic interactions: $e-e$, $e-i$, $i-e$ and $i-i$. We can reduce the number of parameters by rescaling the membrane time constants $\tau = \tau_e/\tau_i$, and additionally, without loss of generality, by considering the external currents to be equal and fixed, $\bar{\eta}_e = \bar{\eta}_i = 1$. In fact, as we will see in the following section, both parameters, $\tau_\alpha$ and $\bar{\eta}_\alpha$, are associated to the mean frequency of single neurons, and therefore, have similar effects over the population activity. Moreover, the temporal dynamics of the E-I system are characterized by the difference of these sets of parameters, i.e. by the difference in the mean frequency of the populations. After rescaling, Eqs. (1.1) become

$$\tau \frac{dr_e}{d\tilde{t}} = -r_e + \Phi_\tau \left(\tau J_{ee} r_e - \tau J_{ie} r_i + 1 + P_e(t)\right), \tag{1.15a}$$

$$\frac{dr_i}{d\tilde{t}} = -r_i + \tau \Phi_\tau \left(J_{ei} r_e - J_{ii} r_i + 1 + P_i(t)\right), \tag{1.15b}$$

where the rescaled firing rate is $r_\alpha = R_\alpha \tau_i$, time is $\tilde{t} = t/\tau_i$, and the transfer function $\Phi_\tau$ is the rescaled version of $\Phi$ (see Eqs. (1.50) and (A.1.4) for details). For $P_\alpha(t) = 0$, the fixed points of Eqs. (1.15) are given by the self consistent relations:

$$r_{e,*} = \Phi_\tau \left(I_e\right), \quad \text{and} \quad r_{i,*} = \tau \Phi_\tau \left(I_i\right), \tag{1.16}$$

with $I_e = 1 + \tau J_{ee} r_e - \tau J_{ie} r_{i,*}$ and $I_i = 1 + J_{ei} r_{e,*} - J_{ii} r_{i,*}$. For better readability, from now on we denote $\Phi_\alpha = \Phi_\tau \left(I_\alpha\right)$.

As in the previous section, we study the linear stability of the fixed points (1.16) to determine whether an oscillatory instability can happen or not. Notice that, as already mentioned above, the results obtained from the current E-I system can be extrapolated to the full ring network (1.2) when the activities of the excitatory [Eq. (1.2a)] and the inhibitory [Eq. (1.2b)] populations remain homogeneous. The Jacobian of the linearized system is

$$J = \begin{pmatrix} -\frac{1}{\tau} + \tau J_{ee} \Phi'_e & -\tau J_{ie} \Phi'_e \\ \tau J_{ei} \Phi'_i & -1 - \tau J_{ii} \Phi'_i \end{pmatrix}, \tag{1.17a}$$

and its trace and determinant are given by

$$\mathrm{tr}(J) = -\left(\frac{1+\tau}{\tau}\right) - \tau J_{ii}\Phi_i' + \tau J_{ee}\Phi_e', \tag{1.17b}$$

$$\det(J) = \frac{1}{\tau} + J_{ii}\Phi_i' - \tau J_{ee}\Phi_e' + \tau^2 \Phi_e'\Phi_i' \left(J_{ei}J_{ie} - J_{ee}J_{ii}\right). \tag{1.17c}$$

The oscillatory instability arises if

$$-\left(\frac{1+\tau}{\tau}\right) - \tau J_{ii}\Phi_i' + \tau J_{ee}\Phi_e' \geq 0, \tag{1.18}$$

which, given that $\Phi_\alpha' > 0$, and $J_{\alpha\beta} \geq 0$, requires $J_{ee} > 0$. Therefore, **recurrent excitation**, $J_{ee}$ must be strong enough for traditional rate models [(1.1) or (1.2)] to show PING oscillations. On the face of things, we may define the minimal firing rate equations for PING oscillations as

$$\tau \frac{dr_e}{d\tilde{t}} = -r_e + \Phi_\tau \left(\tau J_{ee} r_e - \tau J_{ie} r_i + 1 + P_e(t)\right), \tag{1.19a}$$

$$\frac{dr_i}{d\tilde{t}} = -r_i + \tau \Phi_\tau \left(J_{ei} r_e + 1 + P_i(t)\right). \tag{1.19b}$$

**H-PING**

where $J_{ee}$, $J_{ei}$ and $J_{ie}$ are all positive numbers. It is worth mentioning that, perturbations applied asymmetrically to the sub-populations, i.e. $P_e \neq P_i$, did not generate any new qualitative dynamics (not shown) neither in the above equations nor in the full ring network (1.2), except for a difference in the amplitude of the response of each sub-population, which modified their respective relaxation decay times.

These simple mechanisms, ING and PING, constitute the fundamental way in which temporal patterns arise in neural field models. Summarizing, all oscillatory dynamics arise as the interplay between fast excitation followed by an inhibitory reaction. The precise way in which such loop is obtained in neural field models rests upon the different choices of the connectivity profile, and may require the use of temporal delays to effectively force the temporal mismatch between the excitation and the inhibition (Roxin et al., 2005; Roxin and Montbrió, 2011).

#### 1.1.1.3 Spatially inhomogeneous patterns: bump states (BS)

Spatially dependent synaptic connectivity is known to produce persistent localized regions of higher activity in the network as the one shown in

Fig. 1.2(c,d) on page 17. These states are also known as bump states (BS) (Wilson and Cowan, 1973; Amari, 1977). Particularly, it has been shown that such bumps emerge in networks with translationally invariant local excitation combined with global inhibition, a connectivity profile similar to that depicted in Fig. 1.1(b) on page 14. Several works have exploited the emergence of these spatial patterns in ring networks (1.3), to model for example orientation selectivity (Ben-Yishai et al., 1995; Somers et al., 1995) in V1, or other types of feature selectivity (Hansel and Sompolinsky, 1998); or to model spatial short-term memory (Compte, 2000; Gutkin et al., 2001; Wimmer et al., 2014).

A simple way to understand the mechanism underlying a bump state is to investigate an equivalent situation in a two population effective model, like the one depicted in the bottom panel of Fig. 1.1(a). There we have two identical recurrently and cross-coupled populations with synaptic strengths $J_s$ and $J_c$, respectively. The equations are similar to the E-I model (1.1) and read

$$\tau_m \frac{dR_1}{dt} = -R_1 + \Phi\left(\tau_m J_s R_1 - \tau_m J_c R_2 + \bar{\eta} + P_1(t)\right), \tag{1.20a}$$

$$\tau_m \frac{dR_2}{dt} = -R_2 + \Phi\left(\tau_m J_s R_2 - \tau_m J_c R_1 + \bar{\eta} + P_2(t)\right). \tag{1.20b}$$

The stability analysis does not differ much from the two population model. Again there are no limit cycles and we just have fixed points. The phase portrait can be studied by looking at the intersection of the nullclines. Fig. 1.5(b) shows the activity time series of the two population system (1.20) with recurrent excitation $J_s = 7$, as the cross coupling, $J_c$, is gradually increased, therefore increasing the inhibitory coupling between both populations. The upper panels, Fig. 1.5(a), show the phase portraits for different values of the cross coupling. As inhibition increases the nullclines twist towards a cubic shape and eventually they cross giving birth to a pair of symmetric stable nodes. Simultaneously the previous stable node looses its stability. This transition corresponds to a Pitchfork bifurcation typical of systems that undergo a symmetry breaking. Models that display this type of behavior, i.e. in which two variables compete for a "privileged" state, are often known as *winner-takes-all* (WTA) systems and have been used to model two-choice decision making in networks of spiking neurons (Roxin and Ledberg, 2008; Martí et al., 2008). A detailed study of the two population WC model can be found in (Beer, 1995) and also in (Ermentrout and Terman, 2010).

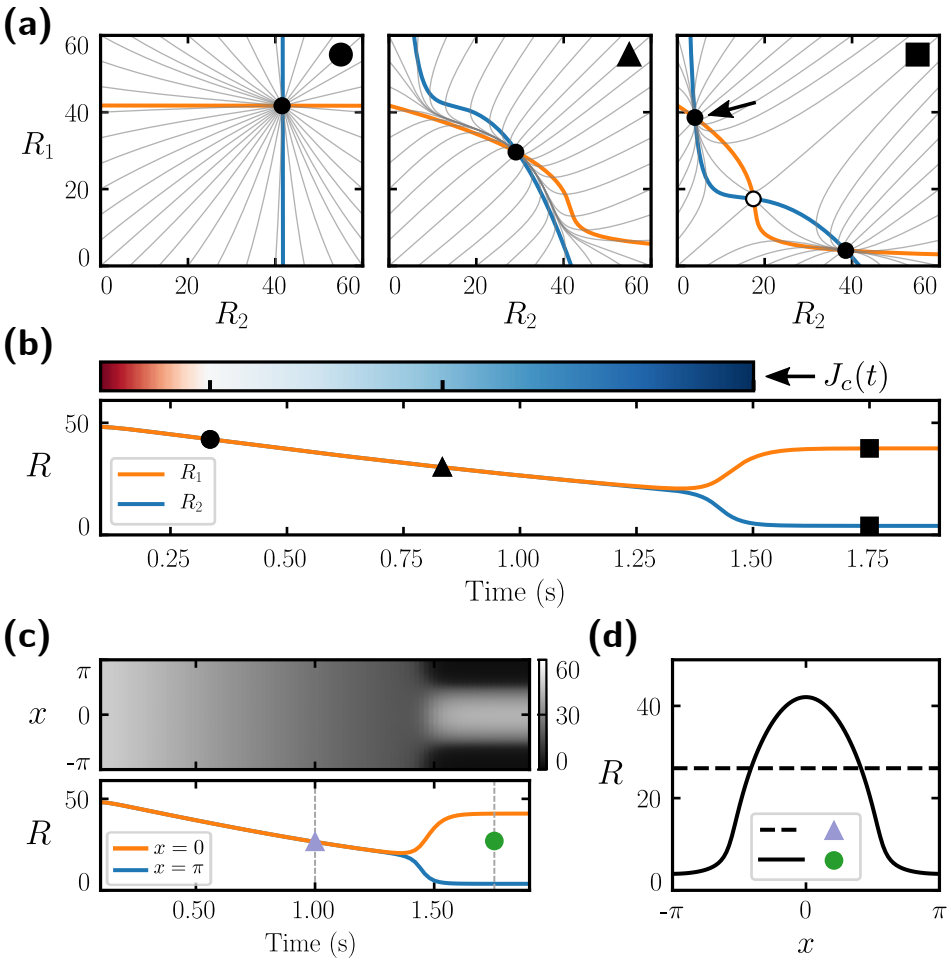


**Figure 1.5:** Symmetry breaking and bump state in the effective two population model and its homologous ring neural field model. Panels (a) and (b) correspond to the two population effective model (1.20), while panels (c) and (d) show results for the effective ring neural field (1.3). In panel (a), three phase portraits corresponding to different values of the cross inhibition $J_c$ are shown. Each of them correspond to different instants of the simulation shown in panel (b), where the cross inhibition, $J_c(t)$, is gradually increased from $J_c = -1.4$ (excitatory) to $J_c = 7$ (inhibitory) as indicated by the color bar. Panel (c) shows an equivalent simulation of the ring neural field in which the first two Fourier coefficients of the connectivity profile (1.4) where gradually modified. In the bottom plot, the time series of to two particular spatial coordinates are represented. Panel (d) shows two representative spatial profiles of the time series of the neural field in panel (c). For both models we used the transfer function corresponding to a population of quadratic integrate-and-fire (QIF) neurons (1.50), and parameters $\bar{\eta} = 1$, $\Delta = 1$, $\tau_m = 20$ ms, $J_s = 7$, $J_c \in (-1.4, 7)$.

The mechanism behind the arousal of the bump state in the effective ring model (1.3) follows this same principle. In Fig. 1.5(c) we have recreated the same situation as in the two population system by appropriately modifying the Fourier coefficients of the connectivity kernel (1.4) to obtain the same values of the self and cross couplings appearing in (1.20). Similarly, once the cross inhibition is sufficiently high—which is equivalent to increasing the first Fourier coefficient, $J_1$—the stability of the spatially homogeneous state is lost as predicted by the eigenvalues of the linearized system (1.8), and the bump state emerges. The spatial profile of the bump state and the SHS are plotted in Fig. 1.5(d).

These results show that the interplay between excitation and inhibition is also capable of forming spatially inhomogeneous patterns. However, the resulting states are steady attractors as opposed to the limit cycles characterizing ING and PING oscillations. Therefore, as it was the case with spatially homogeneous states (SHS), BSs are also asynchronous states. Thus, the existence of such steady inhomogeneous states does not depend on synchronous spiking taking place in the network, but things may change when the state is perturbed or the stability of the BS is compromised. This may occur for example when temporal structure is introduced in the system, for example when assuming different time scales for each sub-population, or when temporal delays are considered. For a broad classification and study of the possible spatiotemporal patterns that emerge when delays are included in the neural field model see Roxin et al. (2005); Roxin and Montbrió (2011). Additionally, fast fluctuations in the external inputs may produce periods of transient synchronous activity as we will see in the following section.

## 1.2 Spike-synchrony in neural field models

The analytical results presented so far prove that neural fields are, indeed, powerful mathematical models due to their analytical amenability and their computational simplicity. However, as we introduced earlier in this chapter, their validity rests upon the constrain of considering asynchronous activity in the underlying network. The question is then, what type of dynamics would be produced when neurons are partially synchronized? Are traditional neural field models correctly describing the dynamics of networks of spiking neurons? In this section we perform numerical simulations of large networks of spiking neurons for the same network architectures presented in the previous section. We will only take into account the necessary elements

required to meet the experimental conditions described in the previous section for each specific spatiotemporal phenomenon, i.e. for describing ING and PING oscillations, and bump states.

The heuristic nature of the traditional firing rate models does not provide a clear relationship between the parameters in the rate model and those in the full network of spiking neurons. It is therefore difficult to design a suitable comparison between both approaches. Nonetheless, in this section we perform numerical simulations of a variety of spiking neuron models with current-based synapses as a way of justifying the universality of the observed phenomena. Yet, our main model of choice is the quadratic integrate-and-fire (QIF) neuron (Ermentrout and Kopell, 1986; Ermentrout, 1996) (see subsection 1.3.1 below), which we further discuss in the next section and serves as the foundation of the Neural Field Model derived in chapter 2. The general mathematical form of an integrate-and-fire model neuron follows (Abbott and Van Vreeswijk, 1993):

$$\tau_m \frac{dv}{dt} = f(v) + RI(t) \quad + \text{resetting rule involving } v_r \text{ and } v_p, \qquad (1.21)$$

where $f(v)$ is the function that shapes the dynamics of the specific model (LIF, QIF, EIF, etc.), and $RI(t)$ corresponds to changes on the membrane potential due to input currents $I$ ($R$ denotes a constant input resistance). The time scale of the dynamics of the neuron is determined by the value of the membrane time constant $\tau_m$. This model needs a resetting rule such that whenever the membrane potential reaches a given peak potential $v_p$, the neuron is reset to the reset potential $v_r$. The particular way in which the resetting is done, and its interpretation depends on the specific function $f(v)$ we use.

A detailed description on the particular models we use: leaky, quadratic and exponential integrate-and-fire models; as well as their numerical implementation is given in Appendix A and in section 2.D. We have also perform numerical simulations considering conductance-based synapses, which showed similar synchronization-related phenomena (see Appendix B.2). In summary, the most relevant features of the simulated networks are:

- All-to-all connectivity among neurons.
- Quenched heterogeneous populations, or identical populations under uncorrelated random inputs, i.e. gaussian white noise (GWN).
- No explicit delays.

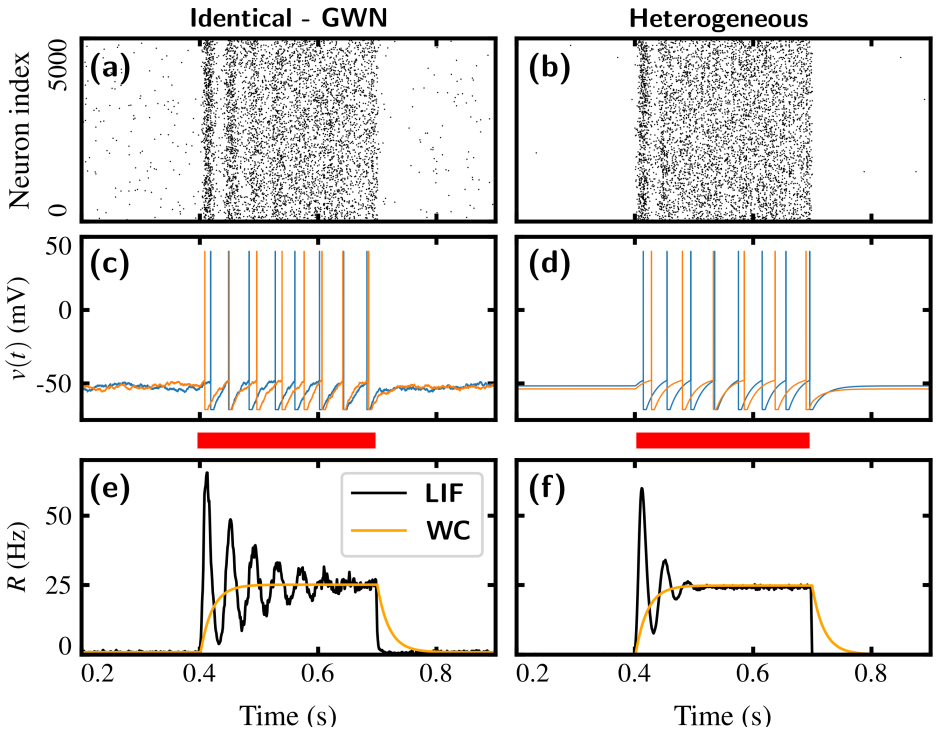


**Figure 1.6:** Fast transient response of a population of noisy (left panels) and heterogeneous (right panel) LIF model neurons [Eq. (1.21)] to an abruptly injected step current (red stripe). Panels (a,b) and (e,f) show the raster plots and instantaneous firing rate activities $R(t)$ of a population of $N = 5000$ LIF neurons. On the left, the population is composed of identical neurons subject to uncorrelated random inputs modeled as GWN of mean $\bar{\eta} = -2$ mV and width $\sigma = 2.0$ mV. On the right, neurons receive constant external that are distributed according to a normal distribution, $\mathcal{N}(-2, 1.4)$ mV. The orange lines in panels (e,f) correspond to the WC equation Eq. (1.5) with the transfer function of a LIF population [Eq. (A.1.4)]. Panels (c,d) show the membrane potential $v(t)$ of two randomly chosen neurons. See Appendix A.1 and Table A.1 for details of the numerical simulations and parameters of the individual LIF neurons. Time constant: $\tau_m = 20$ ms.

Additionally, the choice of microscopic parameters [Table A.1] is done such that most neurons are in the sub-threshold regime but close enough to the firing threshold.

We start by exploring a minimal working example of a network of **uncoupled** leaky integrate-and-fire (LIF) neurons, which implicitly voids any possible effect that synaptic kinetics or temporal delays could cause in

the dynamics of individual neurons, and as a consequence, in the collective response of the population. In this situation, in the steady state neurons are firing at their intrinsic frequency. If there is some degree of disorder in the network, such as random initial conditions, quenched heterogeneity or just noise, the steady state of the network will be characterized by random spiking of the neurons, or in other words, asynchronous activity.

In Fig. 1.6 a network obeying these conditions is shown, in which a step current is applied resulting in a rapid increase of the population activity followed by a damped oscillatory decay towards the equilibrium. Such transient dynamics are intrinsic to any neuronal population having some degree of heterogeneity, and in which a fraction of the population gets enough excitation to maintain them in the spiking regime. Particularly, the population on the left panels in Fig. 1.6 includes only identical neurons receiving uncorrelated random inputs modeled as gaussian white noise (GSW), whereas panels on the right show similar results for a heterogeneous network where neurons receive constant external currents distributed according to a gaussian distribution. This behavior is not exclusive of the LIF spiking neuron model, and can be observed in networks of both, phenomenological and biophysical, neuron models (see comment 1.2.1 for a similar example with QIF neurons). Moreover, their presence in brain tissue has been confirmed by experimental studies done *in vitro* preparations (see e.g Gerstner, 2000; Brunel et al., 2001; Silberberg et al., 2004; Naud and Gerstner, 2012). Yet, the WC model (1.5) shows a slow exponential transient towards the displaced equilibrium point [Fig. 1.6(e,f), orange line], as predicted by the linear stability analysis. This type of transient dynamics are a consequence of the synchronization and subsequent desynchronization processes happening at the population level, that cannot be captured by H-NFMs. However, in the high-noise limit, spiking neuron models respond relatively slowly to the input currents, as the synchrony at subthreshold levels is lost before neurons are able to cross the threshold. This diffusion limit, in which the future state of a neuron only depends on its present state, is often used to justify the validity of H-NFMs.

**Comment 1.2.1: Exact firing rate model for uncoupled QIF neurons**

In a recently published article, Montbrió et al. (2015) derived a set of low dimensional equations exactly describing the macroscopic dynamics of a network of quadratic integrate-and-fire neurons (QIF). These equations

are derived in section 1.3 but here we briefly discuss them for a network of uncoupled neurons in order to better understand why traditional firing rate models fail to capture the phenomenon depicted in Fig. 1.6; i.e., due to the fact that, as previously mentioned, they only track the mean macroscopic activity (in terms of the firing rate), ignoring the effect that neurons' sub-threshold dynamics may have in such processes.

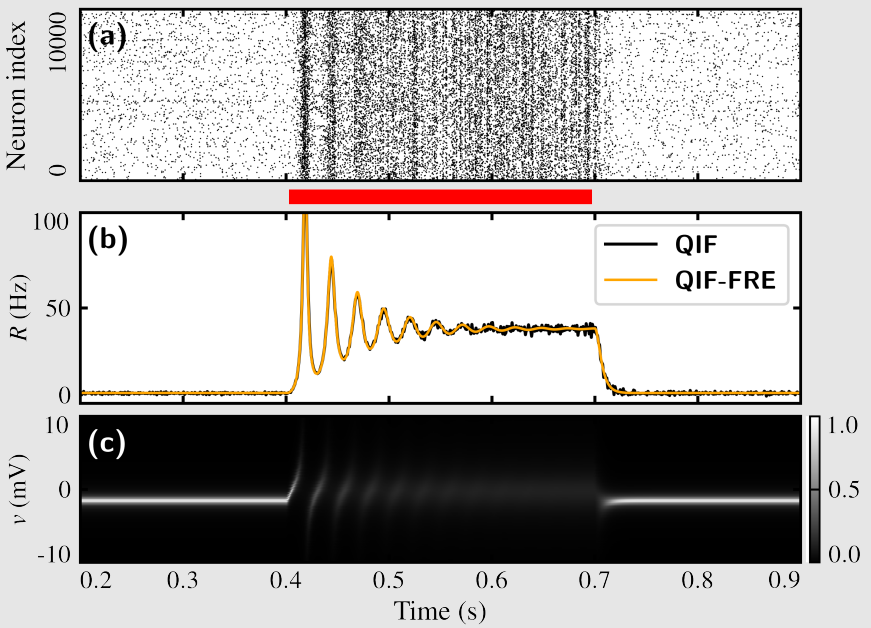


**Figure 1.7:** Transient activity of an uncoupled network of QIF neurons (1.22) under the influence of a step current (red stripe). Panels (a) and (b) show the raster and the firing rate of the population respectively. In panel (b) the orange thin line corresponds to simulations of the QIF firing rate equations (1.23). The color plot in panel (c) shows the time series of the distribution of membrane potentials of neurons.

In Fig 1.7 we recreate the same situation shown in the previous figure [Fig. 1.6]. A step current $P(t)$ is injected in a population of $N$ uncoupled QIF neurons, each characterized by the membrane potential $v_i$, $i = 1, \ldots, N$, and obeying the following dynamical equation

$$\tau_m \frac{dv_i}{dt} = v_i^2 + \eta_i + P(t) \quad + \text{resetting rule}, \tag{1.22}$$

where $\eta_i$ corresponds to external currents following a Lorentzian distribution $g(\eta)$ of mean $\bar{\eta}$ and half-width $\Delta$ (see Eq. (1.46)). The corresponding macroscopic firing rate equations are:

$$\tau_m \frac{dR}{dt} = \frac{\Delta}{\pi\tau_m} + 2RV, \tag{1.23a}$$

$$\tau_m \frac{dV}{dt} = V^2 + \bar{\eta} - (\pi\tau_m R)^2 + P(t). \tag{1.23b}$$

where $R(t)$ and $V(t)$ are the firing rate and the mean membrane potential of the neuronal population, respectively.

We can see that in this case, the results provided by the QIF firing rate equations (1.23) perfectly match the behavior of the QIF spiking network [Fig 1.7(b)]. What determines the success or the failure of these population models in capturing the synchronous activity of the population? This question is difficult to answer and has been tackled in numerous works (e.g. Cowan, 2014), however we can gain some intuition by looking to the specific shape of the equations (1.23).

As we can see, in contrast to the WC equations, the activity here is described by two coupled differential equations in terms of the macroscopic variables: $R$ and $V$. Specifically, the second equation (1.23b) resembles that of the individual QIF neuron (1.22) but with the additional negative feedback provided by the population firing rate itself, which prevents the explosive growth of the mean membrane potential. From the point of view of dynamical systems, the particular shape of Eqs. (1.23)—two differential equations plus the negative feedback from one variable to the other—establish the necessary conditions to be able to generate oscillations. In fact, as we will see in subsection 1.3.5, adding an additional synaptic equation to Eqs. (1.23) is enough to create the previously discussed E-I loop, that generates the ING oscillations (Devalle et al., 2017a).

The bottom panel in Fig.1.7 shows the time evolution of the distribution of membrane potentials of the network. The low activity state is characterized by a sharp distribution (very intense white) with the mean membrane potential below threshold (the threshold is at 0). The sharpness of the distribution is a measure of the level of activity, i.e. the firing rate $R$. The sharper the distribution the lower is the activity. To get a clearer picture of the shape of the distribution see Fig. 1.13. During

the application of the step current, the distribution suddenly widens, reflecting a growth in the firing rate, and is followed by a transient period of sharpening and widening, along with the periodic translation of the center value. This corresponds to the oscillatory behavior seen in panel (b) in the same figure [Fig. 1.7(b)]. Just before the perturbation ends, an equilibrium is reached in which the distribution is wide, indicating higher activity. Finally, once the external input is removed, it returns back to the initial low activity state characterized by the sharp distribution.

Here, we arrive at three general observations regarding the transient synchronization process shown in Figs. 1.6 and 1.7. First, it is observed in a completely uncoupled population of neurons, and thus it is independent of the choice of the connectivity scheme. Second, and related to the previous observation, it appears in the absence of synaptic kinetics or time delays. And third, it has a relevant impact on the macroscopic dynamics as seen in the population activity. We therefore conclude that such dynamics are an intrinsic property of networks of spiking neurons. In the following sections we numerically simulate the network motifs corresponding to the already mentioned ING, PING and the WTA mechanisms. And on the light of things, we expect to find dynamics not predicted by the traditional neural field models. Therefore, we continue numerically exploring the effects of synchronous activity in shaping the dynamics of networks of spiking neurons.

### ING oscillations in spiking neural networks

The simplest form of persistent oscillatory dynamics is given by the ING mechanism. Yet, we have seen that the neural field model (1.3) (or its simplified one-population version (1.13)) needs to include time delays in order to give rise to the I-I oscillatory loop. Let's see what happens in a network of spiking neurons.

Fig. 1.8 on the following page shows simulations for quadratic integrate-and-fire (QIF) and exponential integrate-and-fire (EIF) model neurons for the network structure in Fig. 1.3(a), where inhibitory neurons are recurrently coupled via chemical synapses. Since neurons are all-to-all connected, they receive a common mean field described by the same synaptic kinetics as that used for the WC model Eq. (1.9b). In those simulations, the oscillatory regime arises when the excitation is sufficiently increased (marked by the red thick line under the firing rate plot). Oscillations are characterized

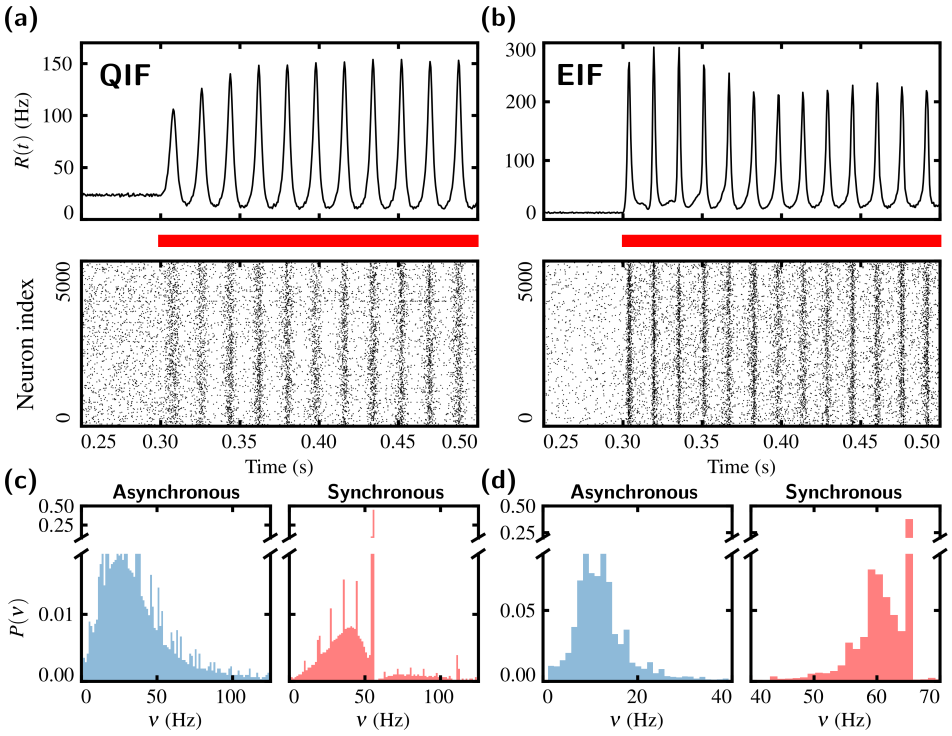


**Figure 1.8:** Networks of heterogeneous inhibitory neurons with synaptic kinetics [Eq. (1.9b)] ($\tau_d = 5$ ms) display macroscopic oscillations in the gamma range (ING oscillations) due to collective synchronization. Panels (a) and (b) show the time series of the firing rate and the rasters for the QIF and the EIF network, respectively. The red thick line indicates the period in which the excitation was increased producing the transition to the oscillatory regime. Panels (c) and (d) show the distributions of frequencies of single neurons for their respective network. In each case, the blue (left) distribution corresponds to the asynchronous regular (AR) regime, while the red (right) distribution corresponds to the synchronous regular (oscillatory) regime. Parameters: $\tau_m = 10$ ms, $J_{ii} = 21$, $\bar{\eta} = 5$ (during the AI regime). QIF: $\Delta = 1$; EIF: $\Delta = 0.5$.

by large population spikes in which large fractions of neurons participate, indicating the appearance of a synchronized state. This is further confirmed when looking to the distributions of frequencies of the single neurons in Figs. 1.8(c) and (d). During the asynchronous regime the distribution of frequencies (blue) is broad with a large fraction of the population firing in the 0-50 Hz range, as expected for an heterogeneous network. However, the abrupt transition to the oscillatory regime is characterized by an overall shift of the distribution towards a central and sharp peak corresponding to

the frequency of the macroscopic oscillations (red). Note the cut in the y-axis of both distributions which separate two different scales; the sharp peak is indeed around 25 times larger than the second highest value of the distribution.

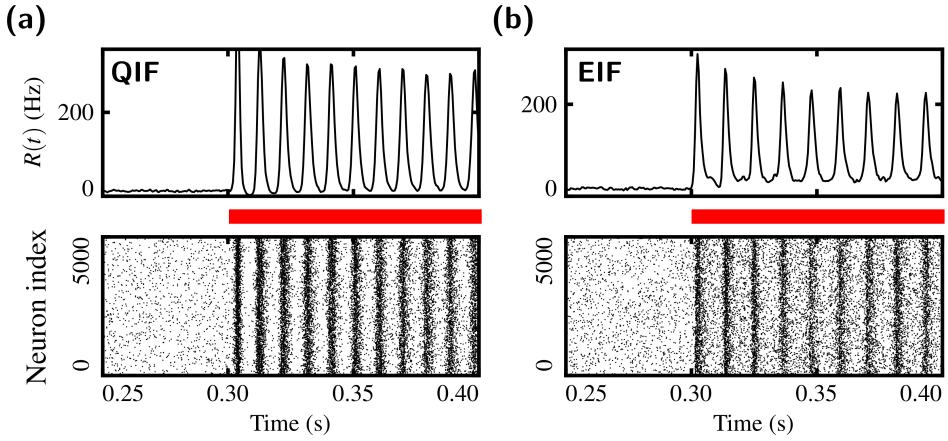


**Figure 1.9:** ING oscillations in networks of identical inhibitory neurons under GWN. Panels (a) and (b) show the time series of the firing rate and the rasters for the QIF and the EIF network, respectively. The red thick line indicates the period in which the excitation was increased producing the transition to the oscillatory regime. Parameters: $\tau_m = 10$ ms, $\sigma = 3$. QIF: $J_{ii} = 21$; EIF: $J_{ii} = 40$.

The heterogeneity in the neural network of Fig. 1.8 was introduced by distributing the external currents $\bar{\eta}_i$ according to a Lorentzian distribution [Eq. (1.46)]. The use of such particular distribution is justified later. However, we also tried using a Gaussian distribution of external currents, as well as identical neurons receiving random inputs modeled as gaussian white noise. Fig. 1.9 shows similar results as those in Fig. 1.8 but for identical neurons under GWN.

Notice that, contrary to the population model (1.13), spiking neuron networks do not require the addition of an explicit delay. It is clear then, that the oscillatory behavior in Fig. 1.8 is a direct manifestation of a synchronized state which is not captured by the H-NFM. ING oscillations constitute a first example of the failure of traditional neural field models to describe synchrony-related patterns arising in networks of spiking neurons. Equation (1.9) correctly describes the fixed points of the asynchronous states, however, stability under the dynamics of Eq. (1.9) does not guarantee stability of the original network of spiking neurons as these numerical simulations prove.

Similarly, the effective ring model (1.3) will not be able to capture ING oscillations arising on the SHS when synaptic kinetics are included. In contrast, the population model that we will present in section 1.3 is able to capture the sub-threshold dynamics of neurons, providing a good description of the macroscopic dynamics arising from this type of networks, as has already been proved by Devalle et al. (2017a).

**PING oscillations in spiking neural networks**

Similarly, we now show that traditional firing rate models [Eqs. (1.1)] do not correctly predict the arousal of PING oscillations. The population model discussed in subsubsection 1.1.1.2 required the inclusion of strong recurrent excitation in order to generate them, but here we show that a network of spiking neurons obeying the network scheme of Fig. 1.3(c), which considers only cross couplings, i.e. $J_{ii} = J_{ee} = 0$, displays robust macroscopic oscillations attributable to the interplay between excitatory and inhibitory neurons, where excitatory cells synchronize inhibitory cells and vice versa. A similar situation involving networks of theta neurons (1.29) has been studied by Börgers and Kopell (2003).

Once again, oscillations with frequency in the gamma range appear when the excitatory sub-population is sufficiently active, and thus faster than the inhibitory sub-population. This can be achieved by injecting a large enough current (marked by the red stripe in Fig. 1.10). Here, in contrast to the ING oscillations, the microscopic mechanism facilitating the synchronization of neurons is more subtle. In the asynchronous regime, the distributions of frequencies of the single neurons [Fig. 1.10(b) and (c)] are similar to those seen for the ING case. On the other hand, in the synchronous regime, the marginal distributions corresponding to the excitatory and inhibitory sub-populations have a remarkably different shape. This can be better seen in the case of QIF neurons, Fig. 1.10(c). The distribution of frequencies of the excitatory population is more dense on the left of the peak—around 40 Hz—, while the inhibitory one is mostly populated on the right of the peak. But, as soon as we consider the joint distribution of both sub-populations, we obtain a distribution displaying the stereotypical synchronization peak with deep valleys on its sides. This peculiar shape occurs when a fraction of the oscillators, that have similar intrinsic frequencies, are locked to a common average frequency. For the particular case of QIF and EIF neurons, this synchronization process can be thought as happening in a *two-stage* manner. Meaning that, the cooperative action of both excitatory and

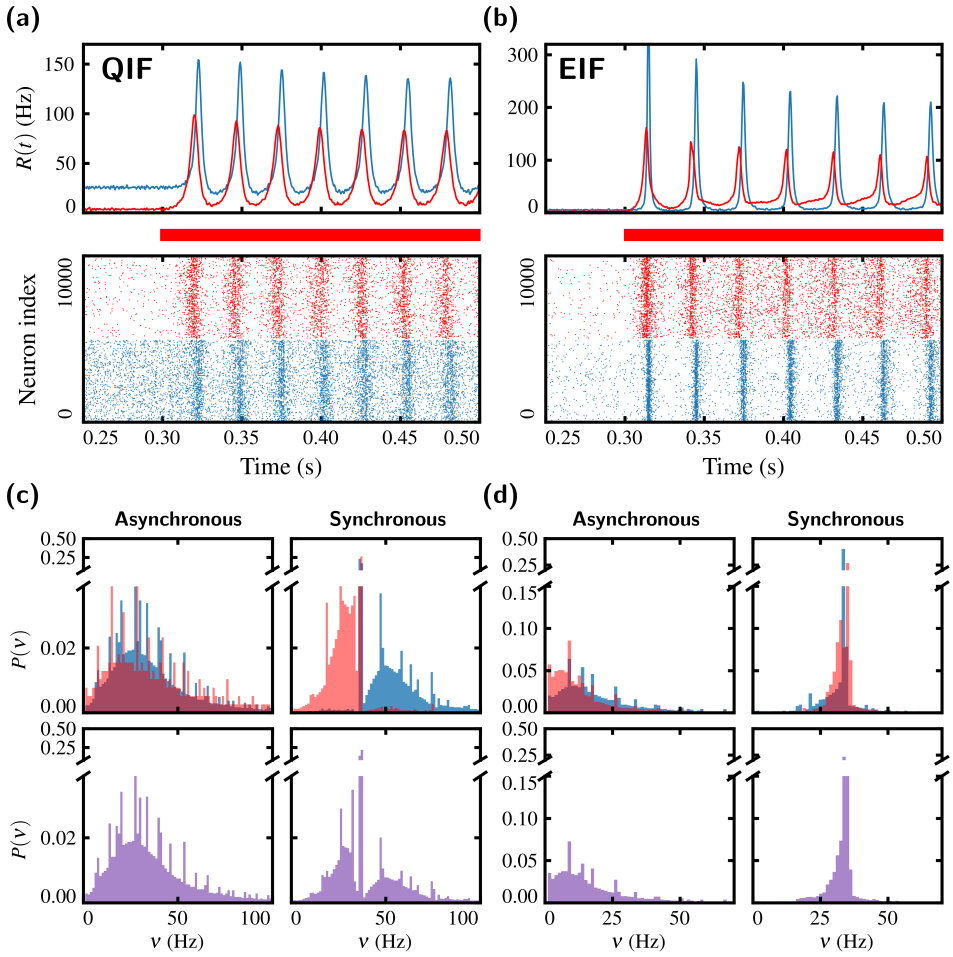


**Figure 1.10:** Networks of heterogeneous cross-coupled excitatory and inhibitory neurons display macroscopic oscillations in the gamma range (PING oscillations) due to collective synchronization. Panels (a) and (b) show the time series of the firing rate and the rasters of excitatory (red) and inhibitory (blue) populations, for the QIF and the EIF network, respectively. The red thick line indicates the time interval in which the excitatory population is injected with an external excitatory current increasing its level of activity, and thus producing the transition to the oscillatory regime. Panels (c) and (d) show the distributions of frequencies of single neurons for their respective network. In the top, red and blue distributions correspond to the excitatory and the inhibitory populations, respectively. In the bottom, their joint distribution is shown. For each model, QIF or EIF, the distribution on the left correspond to the asynchronous regular (AR) regime, while the distribution on the right correspond to the synchronous regular (oscillatory) regime. Parameters: $\tau_i = 10$ ms, $\tau_e = 20$ ms, $J_{ii} = J_{ee} = 0$, $\Delta = 1$ , $\bar{\eta}_i = 0$, $\bar{\eta}_e = 0$ (during the AI regime). QIF: $J_{ie} = 9$, $J_{ie} = 8$; EIF: $J_{ie} = 21$, $J_{ie} = 3$.

inhibitory population is needed. An equivalent situation has been studied in networks of Kuramoto oscillators by Montbrió and Pazó (2018).

These observations contrast with the results obtained from the stability analysis of Eqs. (1.1), where we have seen that recurrent excitation is crucial to obtain PING oscillations. Again, this fundamental discrepancy is a consequence of the inability of traditional firing rate models of capturing sub-threshold dynamics of neurons and its effects on the collective behavior of neuronal populations.

### Transient "standing-waves" in a ring model of spiking neurons

The mechanisms discussed so far (ING and PING) explain the generation of oscillatory dynamics in networks of local E-I sub-populations, but the same principles apply to oscillations emerging from the spatially homogeneous states (SHS) of spatially distributed networks. Note however, that PING oscillations always require separately treating the excitatory and inhibitory sub-populations, and therefore cannot be obtained by means of the effective network [lower panels in Fig. 1.1]. In any case, we have seen that traditional firing rate models fail to capture any of the presented phenomena, including the transient oscillations shown in Figs. 1.6 and 1.7.

We finish this section by exploring the response of a ring network of spiking neurons when spatially modulated perturbations are applied to the neuronal population. The network architecture is the same as the one depicted in Fig. 1.1(b): excitatory and inhibitory neurons are spatially distributed according to the variable $x$, and both sub-populations receive the same amount of synaptic activation at every moment, which allows us to describe the model in terms of an effective coupling [Eq. (1.4)] that combines both excitatory and inhibitory contributions. The simulations presented in Fig. 1.11 were performed following the same procedure as those shown in Fig. 1.2. There we saw that, perturbations of the homogeneous state (the flat state) of the neural field model (1.3) were followed by an exponential relaxation towards the equilibrium state. Here, perturbations of wavenumber $K$ produce transient standing waves [Fig. 1.11(a,b)], whose frequency and decay time depend on the corresponding mode $J_K$ of the connectivity kernel (1.4). The precise relation between the connectivity structure and the frequency of the decaying oscillations is the main subject of the next chapter. Such oscillations are again the macroscopic reflection of transient episodes of synchronization, equivalent to those seen in Figs. 1.6 and 1.7. Nevertheless, in this particular case the interplay between excitation

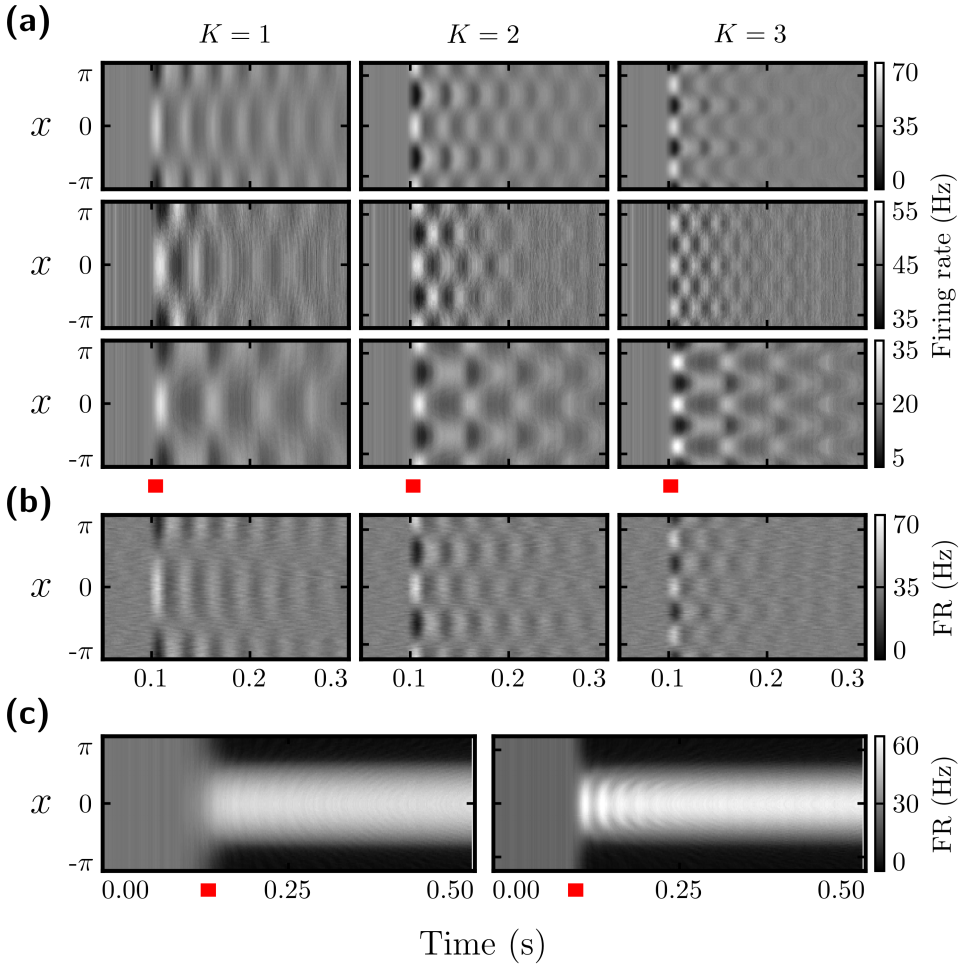


**Figure 1.11:** Transient episodes of spike synchrony in ring networks of spiking neurons as a result of brief spatially inhomogeneous perturbations (marked with a red square). **(a)** From top to bottom, LIF, QIF and EIF heterogeneous networks show decaying standing waves for perturbations of different wavenumbers, $K = 1, 2, 3$. **(b)** Equivalent simulations carried on in a network of identical LIF neurons under GWN show very similar responses. **(c)** Examples of the destabilization of the SHS into the bump state in heterogeneous networks of QIF (left) and EIF (right) neurons. In the right panel the bump is abruptly formed exhibiting an oscillatory behavior. See Appendix A.1 for details on the simulations.

and inhibition in the spatial dimension has a direct effect on the frequency of oscillations—and for some spiking neuron models, in the decay time. Notice that the observed phenomena is common to a variety of spiking neuron models (in Fig. 1.11(a) LIF, QIF and EIF), and for both heterogeneous and identical networks, Figs. 1.11(a) and (b), respectively.

In addition, we were interested in exploring the response of the bump to the already mentioned inhomogeneous perturbations. Panel (c) in Fig. 1.11 shows the emergence of the bump state for a network of QIF (left) and EIF (right) neurons when the SHS looses its stability. In the first case, the arousal of the bump is smooth, indicating that the bump state behaves as a stable "node", while in the second case (simulated in different conditions) the formation of the bump state is accompanied by a transient period of oscillatory dynamics. This latter effect is also seen in networks of QIF neurons and we discuss it in detail in subsection 2.3.4, but on the light of previous observations we may already suggest that their origin is the same as that of the decaying standing waves, i.e. transient episodes of synchronization.

Transient standing waves, observed in both the SH and bump states, are therefore one of the simplest phenomenon we can encounter in a spatially extended network of spiking neurons, which due to its underlying microscopic mechanism cannot be described by traditional neural field models. The extensive use of such models for studying a wide variety of cognitive processes, where oscillatory dynamics could play an important role, is what motivates us to further study the phenomenology related to the observed dynamics in Chapter 2. However, due to the lack of an appropriate low-dimensional description of such networks, an exhaustive study of the observed phenomena has been up to now unfeasible. Luckily, the newly derived firing rate model, briefly introduced in comment 1.2.1 and that we discuss next, allowed us to derive an equivalent exact neural field model for a network of QIF neurons, which facilitated the study of what we call *modes of oscillations* of a neural field model.

## 1.3 Firing rate model for QIF neurons (QIF-FRE)

As it was shown in the preceding section, traditional firing rate models fail to describe population dynamics when a significant fraction of the neurons

happens to fire synchronously. In this section we present a recently published set of exact macroscopic equations for quadratic integrate-and-fire neurons (QIF-FRE) which explicitly takes into account sub-threshold integration (Montbrió et al., 2015). In the next chapter we will expand this set of equations to an exact neural field model, and we will compare its dynamics with their equivalent microscopic representation, i.e. simulations of QIF neurons. Here, we also show that in the limit of slow synaptic kinetics the QIF-FREs reduce to an equation formally identical to the WC equation (1.5). Finally, we finish this chapter by reviewing the most relevant results obtained after the discovery of the QIF-FREs, and enumerate some of the questions that still remain open for research or that are currently being investigated.

### 1.3.1 Quadratic Integrate-and-Fire (QIF) model neuron

So far, we have performed numerical simulations using various models of integrate-and-fire neurons and we have seen similar qualitative behaviors for a wide range of conditions. All these models represent simplified versions of the Hodgkin-Huxley (HH) model with only standard spiking currents. In particular, they are examples of Class I excitability neurons, characterized by the presence of a saddle-node bifurcation on an invariant circle at the transition from quiescence to spiking. Near threshold the spiking dynamics are dominated by the time spent in the vicinity of the saddle-node itself, allowing for a formal reduction in dimensionality from the HH model to a reduced normal-form equation for a saddle-node bifurcation (Ermentrout and Terman, 2010; Ermentrout, 1996; Izhikevich, 2007).

This normal-form is also known as the **Quadratic** integrate-and-fire model which is a specific instance of the nonlinear integrate-and-fire model [Eq. (1.21)] where the voltage dependent function takes the form $f(v) = v^2$. Therefore the QIF neuron represents the canonical model for Class I neurons. The time evolution equation for the membrane potential may be written as (Hansel and Mato, 2001, 2003; Latham et al., 2000)

$$C\frac{du}{dt} = g_L\frac{(u-u_{th})\,(u-u_r)}{u_{th}-u_r} + I_u, \quad (+\text{ resetting rule}), \tag{1.24}$$

where $C$ is the cell capacitance, $g_L$ is the leak conductance and $I_u$ are input currents. Additional cell parameters are $u_{th}$ and $u_r$ which represent the threshold and resting potentials of the neurons, respectively. As it also happens with the other integrate-and-fire models, the generation of the spike requires a resetting rule. In numerical simulations, once the voltage reaches

a given peak value is manually reset to $u_r$. Mathematical analysis of the QIF neuron is greatly facilitated after simplifying this equation by performing a shift in the membrane potential and rescaling,

$$u' = u - \frac{u_{th} + u_r}{2} \quad \longrightarrow \quad v = \frac{u'}{u_{th} - u_r}, \tag{1.25}$$

reducing the QIF model Eq. (1.24) to

$$\tau_m \frac{dv}{dt} = v^2 + I, \quad (+ \text{ resetting rule}), \tag{1.26}$$

where $\tau_m = C/g_L$ is the membrane time constant, and $I$ are the rescaled (dimensionless) currents:

$$I = \frac{I_u}{g_L \left(u_{th} - u_r\right)} - \frac{1}{4}. \tag{1.27}$$

In the following we will use Eq. (1.26) when referring to the QIF model, and we will denote the (dimensionless) membrane potential of neuron $i$ with $v_i$.

Notice that the ODE describing the QIF neuron may grow without bound depending on the value of the input currents $I$. This behavior accounts for the generation of the spike, and therefore requires the use of the already mentioned resetting rule to return the neuron to the sub-threshold regime. The QIF model exhibits two possible dynamical regimes which depend on the sign of $I$. If $I < 0$ the neuron is said to be in the excitable regime, whereas for $I > 0$ the neuron is in the oscillatory regime. In the excitable regime, an initial condition $v(0) < \sqrt{-I}$ asymptotically approaches the resting potential $-\sqrt{I}$. On the other hand, initial conditions above the excitability threshold, $v(0) > \sqrt{-I}$, lead to an unbounded growth of the membrane potential. Specifically, if $v(0) \gg \sqrt{I}$, then the membrane potential reaches infinity approximately after a time $\tau_m/v(0)$. In numerical simulations, this divergence is usually avoided by implementing a resetting rule by hand. When the membrane potential $v$ reaches a certain peak value $v_p \gg 1$, the neuron is reset to the value $v_r \ll -1$ after a relative refractory period $\tau_m/v_p + \tau_m/v_p$. Moreover, in the oscillatory regime, $I > 0$, the neuron needs to be reset periodically with an approximate frequency $\nu = \sqrt{I}/(\tau\pi)$, provided $v_p \gg 1$. These dynamical features are summarized in Fig. 1.12 on the next page: top (bottom) panels correspond to the excitable (oscillatory) regime; left panels represent the phase portrait for each dynamical regime

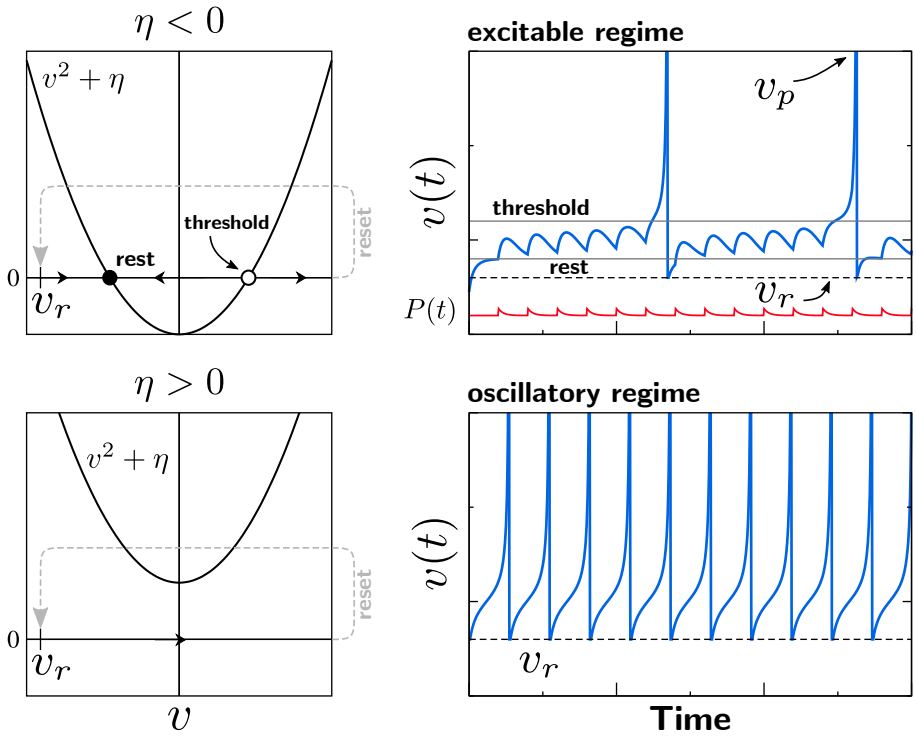


**Figure 1.12:** Schematic representation of the two possible regimes of the QIF neuron (1.26) with an input current $I = \eta + P(t)$. Top and bottom panels correspond to the excitable and oscillatory regimes, respectively. For each regime, left and right panels show the corresponding phase portrait and a representative time series, respectively. In the top right panel, a time varying external input $P(t)$ is plotted in red, which after some time drives the neuron's voltage across the threshold (○: unstable fixed point in the left panel) producing a spike. Then the voltage is reset (gray dashed path in the left panel) to $v_r$ which drives the neuron back to the rest potential (●: stable fixed point in the left panel). The effect of any perturbation $P(t)$ in the phase portrait leads to a vertical shift of the parabola, i.e. excitatory (inhibitory) currents shift the parabola upwards (downwards), with the subsequent displacement of the fix points. In the oscillatory regime there are no fixed points and therefore the neuron is firing with a constant frequency proportional to $\eta$.

while right panels show representative simulations of the dynamics of the QIF neurons in each case. Note that the current $I$ is a combination of the constant external current $\eta$ and the time varying input $P(t)$. Therefore even if the constant current in the top panels is negative, each pulse of the input current—in red—drives the voltage closer to the threshold value, which eventually leads to the emission of a spike.

**Theta neuron**

For a simplified mathematical analysis of the QIF model, one takes* $v_p \to +\infty$ and $v_r \to -\infty$, which then using the following change of variables

$$v(t) = \tan\left(\frac{\theta(t)}{2}\right), \tag{1.28}$$

transforms the QIF model into a phase model, called the Theta-Neuron model (Ermentrout and Kopell, 1986; Gutkin and Ermentrout, 1998; Hoppensteadt and Izhikevich, 1997),

$$\tau_m \frac{d\theta}{dt} = (1 - \cos\theta) + I\,(1 + \cos\theta)\,, \quad \theta \in (-\pi,\ \pi)\,. \tag{1.29}$$

This phase model has a strictly positive Phase Resetting Curve (PRC). Neurons exhibiting such PRCs are known as Type 1 neurons, indicating that (positive) perturbations always produce an advance (and not a delay) of their phase.

Because the theta model is a phase oscillator, it does not properly produce spikes. Therefore, the spike time is normally assumed to take place whenever the phase, $\theta(t)$, crosses $\theta = \pi$. Both models are mathematically equivalent in this limit, and numerical simulations of both models should give similar results.

In the next sections we derive the macroscopic equations for a population of QIF neurons following the work of Montbrió et al. (2015).

### 1.3.2 Continuity equation for a population of QIF neurons

Let us now consider a population of $N$ all-to-all coupled QIF neurons. The state of the system will be characterized by the neurons' membrane potentials $\{v_i\}_{i=1,\dots,N}$, each obeying Eq. (1.26)

$$\tau_m \frac{dv_i}{dt} = v_i^2 + I_i, \tag{1.30}$$

QIF neuron

*In order to mimic this limit in numerical simulations, it is convenient to take $v_r = -v_p$ with $v_p \gg 1$.

where the input currents $I_i$ will account for a constant external current, $\eta_i$, and for time varying inputs coming from within and outside the population,

$$I_i = \eta_i + \tau_m J_0 S(t) + P(t). \tag{1.31}$$

The external time varying inputs are denoted as $P(t)$ whereas the recurrent current $J_0 S(t)$ is equal to the synaptic weight $J_0$ times the mean synaptic activation $S(t)$ due to the firing activity of the population*,

$$S(t) = \frac{1}{N} \sum_{j=1}^{N} \sum_{k} \int_{-\infty}^{t} \alpha_{\tau_s} (t - t') \, \delta \left( t' - t_j^k \right) \, dt'. \tag{1.32}$$

Synaptic activation is the common mean field driving all neurons, which sums the changes in the current due to all the spiking activity occurring prior to time $t$. Each $k$th spike emitted by neuron $j$th is modeled as an instantaneous pulse happening at time $t = t_j^k$ which is represented by a Dirac delta $\delta \left( t - t_j^k \right)$. The pulse is then convoluted with a synaptic kernel $\alpha_{\tau_s}$ characterized by the time constant $\tau_s$.

In the limit of infinitely fast synapses (instantaneous rise and decay), $\tau_s \to 0$, the synaptic activation (1.32) is equivalent to the instantaneous population mean firing rate

$$R(t) = \lim_{\tau_s \to 0} \frac{1}{\tau_s} \frac{1}{N} \sum_{j=1}^{N} \sum_{k} \int_{t-\tau_s}^{t} \delta \left( t' - t_j^k \right) \, dt'. \tag{1.33}$$

#### 1.3.2.1 Continuous formulation

The application of a continuous formulation is justified by the *columnar organization* hypothesis. We assume that cortical cells can be grouped into "columns" of neurons with similar properties containing up to several thousand neurons (Hubel and Wiesel, 1968; Lund et al., 2003; Lodato and Arlotta, 2015). As a result, we may apply the thermodynamic limit in Eqs. (1.30), (1.31) and (1.33), and define the *membrane potential density* function $\rho (v|\eta, t)$. This approach has been also followed by e.g. Abbott and Van Vreeswijk (1993); Brunel and Hakim (1999); Fusi and Mattia (1999); Brunel (2000); Nykamp and Tranchina (2000); Omurtag et al. (2000). Thus,

*For clearer reading, abuse of notation often ignores the time convolution in the right hand side of Eq. (1.32).

at time $t$, the fraction of neurons with membrane potentials between $v_0$ and $v_0 + \Delta v$, and parameter $\eta$ is given by

$$\int_{v_0}^{v_0+\Delta v} \rho\left(v|\eta,t\right) dv. \tag{1.34}$$

Additionally, we assume the population to be heterogeneous by considering a distribution $g(\eta)$ for the external currents [$\eta \in (-\infty,\ \infty)$]. Hence, the total voltage density is

$$\int_{-\infty}^{\infty} \rho\left(v|\eta,t\right) g\left(\eta\right) d\eta, \tag{1.35}$$

and bringing back the limit $v_p \to \infty$ and $v_r \to \infty$, the conservation of the number of neurons implies

$$\int_{-\infty}^{\infty} \left( \int_{-\infty}^{\infty} \rho\left(v|\eta,t\right) g\left(\eta\right) d\eta \right) dv = 1, \quad \forall t. \tag{1.36}$$

We may now translate all this [Eqs. (1.30), (1.31), (1.33) and (1.36)] into the continuity equation

$$\frac{\partial \rho}{\partial t} + \frac{\partial}{\partial v} J\left(v|\eta,t\right) = 0, \tag{1.37}$$

where the probability flux $J\left(v|\eta,t\right)$ is the net fraction of neurons with parameter $\eta$ that crosses the value $v$ per unit time, and is equal to the density of neurons multiplied by the *velocity* of $v$ (right hand side of Eq. (1.30)), that is

$$J\left(v|\eta,t\right) = \frac{1}{\tau_m} \rho\left(v|\eta,t\right) \left(v^2 + \eta + \tau_m J_0 R + P\right). \tag{1.38}$$

The continuity equation describes the temporal evolution of the distribution of membrane potentials of the neuronal population, and therefore gives a complete dynamical description of the state of the system. However, it still represents an infinite dimensional system, in which the knowledge of the exact form of the distribution is crucial to obtain a precise description of the macroscopic dynamics.

### 1.3.3 Dimensionality reduction: Lorentzian Ansatz

What Montbrió et al. discovered, inspired by the work of Ott and Antonsen (2008) and later by Luke et al. (2013); So et al. (2014), was precisely that the

distribution of the membrane potentials followed a Lorentzian function (also known as Cauchy distribution). Therefore, by considering the Lorentzian ansatz (LA)

$$\rho\left(v|\eta,t\right)=\frac{1}{\pi}\frac{x\left(\eta,t\right)}{\left[v-y\left(\eta,t\right)\right]^{2}+x\left(\eta,t\right)^{2}} \tag{1.39}$$

the state of the system is completely characterized by **two macroscopic** magnitudes, $x$ and $y$ which have a direct relationship with physically meaningful macroscopic quantities related to the population activity. A similar, but approximate methodology is followed in many other population density models to infer the macroscopic behavior of populations of neurons*.

Notice that the firing rate of the population with a given $\eta$ is just the drift flux $J_{\mathrm{d}}(v_p|\eta,t)$ through the peak potential $v_p$ (when the spike is emitted). Therefore we have

$$R\left(\eta,t\right)=\frac{1}{\tau_m}\lim_{v_p\to\infty}\rho\left(v_p|\eta,t\right)\cdot\left.\frac{\partial v}{\partial t}\right|_{v_p}=\frac{x\left(\eta,t\right)}{\pi\tau_m}. \tag{1.40}$$

To obtain the **total firing rate** we need to integrate the latter quantity over all possible values of the external current, which gives

$$R\left(t\right)=\frac{1}{\pi\tau_m}\int_{-\infty}^{\infty}x\left(\eta,t\right)g\left(\eta\right)d\eta. \tag{1.41}$$

On the other hand, the remaining macroscopic quantity $y\left(\eta,t\right)$ is easily identified with the mean membrane potential, because, by definition, is the center† of the distribution of membrane potentials:

$$y\left(\eta,t\right)=\text{p.v.}\int_{-\infty}^{\infty}v\rho\left(v|\eta,t\right)dv, \tag{1.42}$$

and equivalently the **total mean membrane potential** is

$$V\left(t\right)=\int_{-\infty}^{\infty}y\left(\eta,t\right)g\left(\eta\right)d\eta. \tag{1.43}$$

*Of particular interest is the paper of Amari (1972), where he also obtained two macroscopic quantities related to the width and the center values of the distribution of membrane potentials

†Statistical moments of the Lorentzian distribution are not well-defined, nevertheless the central value exists and is well defined by its median value or its mode. It can be computed through the principal value: p.v. $\int_{-\infty}^{\infty}f(x)dx=\lim_{a\to\infty}\int_{-a}^{a}f(x)dx$.

**Comment 1.3.1: The interplay between the firing rate and the mean membrane potential: the distribution of membrane potentials**

For a particular distribution of external currents $g(\eta)$ (see Eq. (1.46) in the main text) the total distribution of membrane potentials becomes

$$\rho\left(v,t\right)=\frac{\tau_m R(t)}{\left(v-V(t)\right)^2+\left(\pi\tau_m R(t)\right)^2}. \tag{1.44}$$

It is worth commenting on the implications of these preliminary results as compare to traditional firing rate equations (1.5). Here we can see that the mean field approach collapses the infinite ODE system into two macroscopic quantities, and hence provides us with a description of the macroscopic dynamics in terms of two variables—$x$ and $y$, which are related to the firing rate, $R$, and the mean membrane potential, $V$, of the neuronal ensemble. In contrast, traditional firing rate models are described only by a single variable, i.e. the firing rate of the population.

In Fig. 1.13 an example of the evolution of the network activity under the influence of a time-varying external current, $P(t)$, is shown. The network consists on a heterogeneous ensemble of $N = 10^4$ uncoupled, $J_0 = 0$, QIF neurons [Eq. (1.30)]. At an approximate time $t = 0.15$ s, a slowly growing input current is injected into the population [Fig. 1.13(e)] producing a gradual increase in the firing rate. This change in the activity is very well reflected in the distributions of membrane potentials shown in Figs. 1.13(a,b,c), where we can see that for very low firing rates [Fig. 1.13(a)] the distribution is sharply centered at a low value of the membrane potential—black arrows delimit the full width at half maximum. The growing input gradually increases the sub-threshold voltages, displacing the center of the distribution. Simultaneously, the density of neurons crossing the threshold increases, and therefore so does the firing rate. This in turn, widens the distribution, as seen in Figs. 1.13(b) and 1.13(c). Finally, the conservation of neurons adds a constrain to the normalization of the distribution $\rho(v)$ [Eq. (1.44)], binding $x(t)$ to $y(t)$, or equivalently, establishing a functional relationship between $R(t)$ and $V(t)$.

This derivation suggests that a correct macroscopic description of the dynamics of spiking networks requires keeping track of the mean sub-threshold voltage along with the mean firing rate.

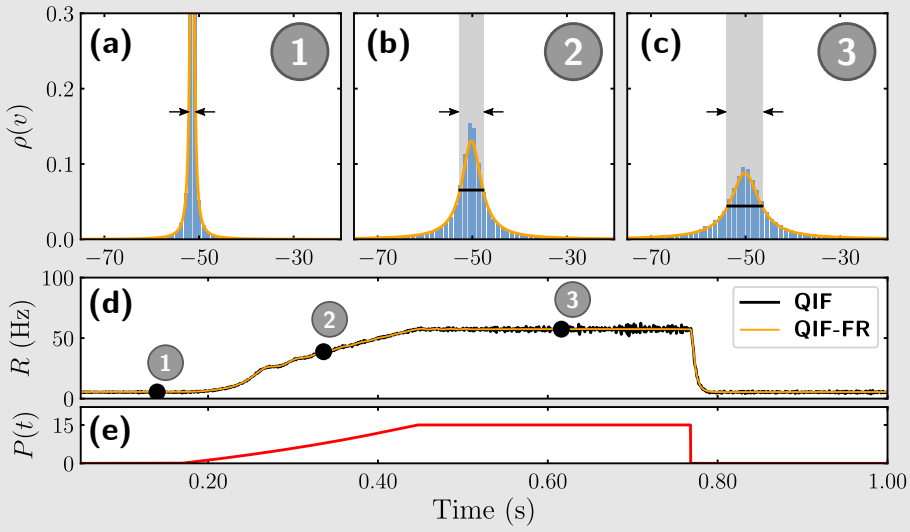


**Figure 1.13:** Macroscopic observables of the activity, such as the firing rate $R$ in panel (d), are directly related to the membrane potential distribution $\rho(v)$ [Eq. (1.44)]. Panels (a), (b) and (c) show the instantaneous distributions of membrane potentials for three selected instants of the network's evolution depicted in panel (d). The histograms are obtained by numerically simulating a network of $N = 10^4$ QIF neurons subject to a slowly time-varying perturbation $P(t)$, as shown in panel (e). The orange line in panels (a), (b) and (c) is the Lorentzian distribution (1.44) analytically obtained using the firing rate $R$ and mean membrane potential $V$ from Eqs. (1.47). It can be clearly seen that the half width at half maximum, $\gamma$ (not shown in panel (a)), is related to the firing rate of the neural activity by the simple relation $\gamma = \pi\tau_m R$. In panel (d) the black line corresponds to the firing rate measured from the network of QIF neurons, whereas the orange line has been simulated using Eqs. (1.47).

### 1.3.4 Solution to the continuity equation: QIF-FR equations

In order to solve the continuity equation (1.37), we plug in the LA (1.39) obtaining the following relation between $x$ and $y$

$$\frac{d}{dt}w(\eta,t) = i\left[\eta + \tau_m J_0 R(t) - w(\eta,t)^2 + P(t)\right], \tag{1.45}$$

where $w(\eta,t) \equiv x(\eta,t) + iy(\eta,t)$. Therefore the macroscopic state is exactly described by Eqs. (1.41), (1.43) and (1.45), establishing a system

of integro-differential equations*. However, for certain choices of the distribution of external currents, $g(\eta)$, the dimensionality of the system is further reduced. In particular, if we take $g(\eta)$ to be distributed according to a Lorentzian distribution of half width at half maximum $\Delta$ and centered at $\bar{\eta}$

$$g(\eta) = \frac{1}{\pi}\frac{\Delta}{(\eta-\bar{\eta})^2+\Delta^2}, \tag{1.46}$$

we can apply the residue theorem (see Appendix B.1.1 for a detailed derivation) to solve the integrals in Eqs. (1.41) and (1.43) which leads to the QIF-FREs in terms of $R = R(t)$ and $V = V(t)$:

$$\tau_m \frac{dR}{dt} = \frac{\Delta}{\pi\tau_m} + 2RV, \tag{1.47a}$$

$$\tau_m \frac{dV}{dt} = V^2 + \bar{\eta} + \tau_m J_0 R - (\pi\tau_m R)^2 + P(t). \tag{1.47b}$$

QIF-FREs

One of the main advantages of this model is its mathematical amenability, which allows us to perform the linear stability analysis in a few steps. The fixed points are:

$$V_* = -\frac{\Delta}{2\pi\tau_m R_*}, \tag{1.48a}$$

$$R_* = \frac{1}{\pi\tau_m\sqrt{2}}\sqrt{(\bar{\eta}+\tau_m J_0 R_*) + \sqrt{(\bar{\eta}+\tau_m J_0 R_*)^2+\Delta^2}}, \tag{1.48b}$$

where the self-consistent equation (1.48b) is actually a quartic equation

$$(\pi\tau_m)^2 R_*^4 - \tau_m J_0 R_*^3 - \bar{\eta} R_*^2 - \left(\frac{\Delta}{2\pi\tau_m}\right)^2 = 0, \tag{1.49}$$

that can be solved parametrically if needed. It also provides us with the **transfer function** or **f-I** curve of the QIF population which we used in previous sections:

$$\Phi(I) = \frac{1}{\pi\tau_m\sqrt{2}}\sqrt{I+\sqrt{I^2+\Delta^2}}, \tag{1.50}$$

*A detailed step-by-step derivation is provided in Appendix B.1.

where $I$ accounts for all inputs arriving to the population, including recurrent synaptic inputs $J_0 R$. The linear stability analysis of the fixed points [Eqs. (1.48)] gives the following eigenvalues

$$\lambda_{\pm} = \frac{-\Delta}{\pi \tau_m^2 R_*} \pm 2\pi R_* \sqrt{\frac{J_0}{2\pi^2 \tau_m R_*} - 1}. \tag{1.51}$$

The trace of the linearized system, $\mathrm{tr} = 4V_*$, is always negative, hence, all fixed points are stable. In addition, for parameters obeying $J_0 > 2\pi^2 \tau_m R_*$ the eigenvalues are always real, and therefore the fixed point $(R_*, V_*)$ is always a stable node. This condition gives us the boundary

$$\bar{\eta} = -\left(\frac{J_0}{2\pi}\right)^2 - \left(\frac{\pi \Delta}{J_0}\right)^2 \tag{1.52}$$

depicted in Fig. 1.14(a) with a dashed line. On the other hand, a saddle-node bifurcation occurs when $\lambda = 0$, or equivalently, at the critical coupling

$$J_0^c = 2\pi^2 \tau_m R_* + \frac{\Delta^2}{2\pi^2 \tau_m^3 R_*^3}, \tag{1.53}$$

which combining it with Eq. (1.49) gives the parametric boundary

$$(\bar{\eta}, J_0) = \left( -\left(\pi \tau_m R_*\right)^2 - 3\left(\frac{\Delta}{2\pi \tau_m R_*}\right)^2,\ 2\pi^2 \tau_m R_* + \frac{\Delta^2}{2\pi^2 \tau_m^3 R_*^3} \right), \tag{1.54}$$

represented with a black line in Fig. 1.14(a). This boundary encloses a region of bistability where a stable low activity node coexists with a stable high activity focus, giving rise to dynamics similar to that represented in Fig. 1.14(c).

For a more detailed analysis of the equations see Montbrió et al. (2015). The already discussed features of the model are summarized in Fig. 1.14.

**Damped oscillations due to transient synchronization**

As we had already advanced in Comment 1.2.1, one of the remarkable properties of these firing rate equations is the fact that one of the stable fixed points is a focus. This is a direct consequence of the single-cell spike generation and reset mechanism not captured in traditional firing rate equations.

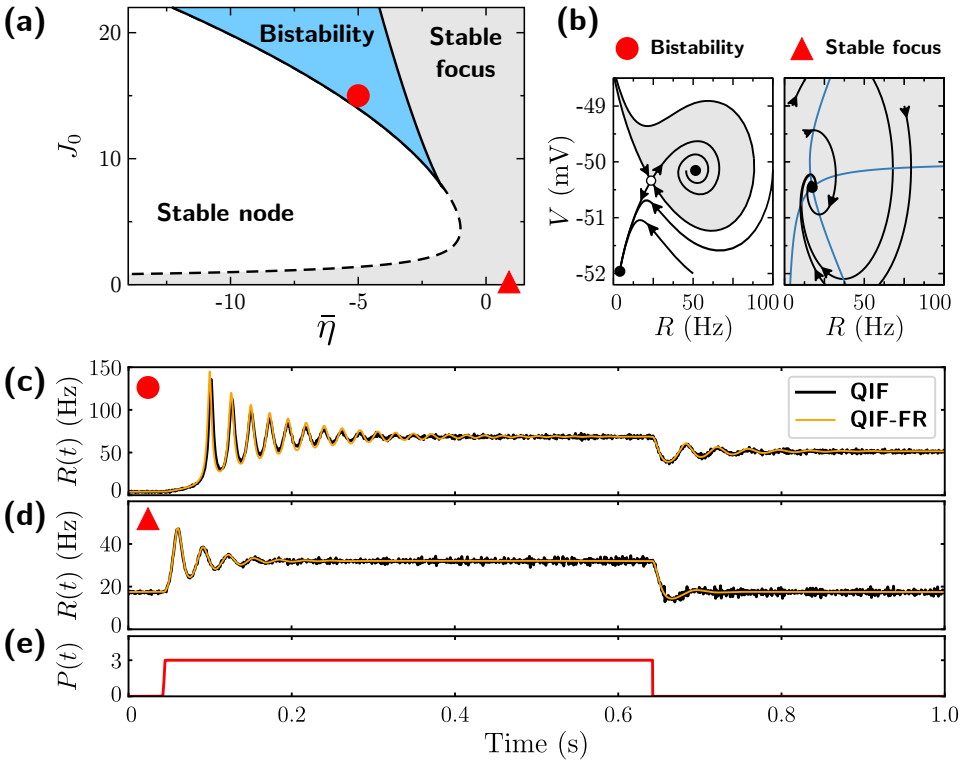


**Figure 1.14:** Phase diagram, phase portraits and time series of the quadratic integrate-and-fire firing rate model (1.47). **(a)** Phase diagram: the bistability region, in blue, is enclosed in a boundary defined by the locus of a saddle-node bifurcation, where the stable node and the focus coexist. **(b)** Phase portraits of the system; the bistable region (left) is denoted with a red circle located at $(\bar{\eta}, J_0) = (-5, 15)$ in panel (a), and the focus (right) is denoted with a red triangle at $(\bar{\eta}, J_0) = (1, 0)$ in panel (a). The gray shaded region marks the basin of attraction of the focus. Blue lines in the right phase portrait correspond to the nullclines. **(c) and (d)** Instantaneous firing rate of the QIF network [Eqs. (1.30) and (1.31)] exactly described by the QIF-FREs (1.47). Transient dynamics are generated by the step current $P(t)$ shown in panel **(e)**. Other parameters are: $\Delta = 1$, $\tau_m = 20$ ms. Voltages are shifted post simulation, such that the mean threshold is at $v_{th} = -50$ mV.

At this point we can make a simple analogy with the damped harmonic oscillator. In the absence of forcing, and in the underdamped regime, the harmonic oscillator responds with damped oscillations with a frequency corresponding to its natural frequency. Similarly, in the QIF-FREs, even without coupling, $J_0 = 0$, brief perturbations will generate damped oscil-

latory activity [Figs. 1.6, 1.7 and Fig. 1.14(c, d) above], with a "natural" frequency equal to the value of the firing rate $R_*$,

$$\omega_0 = R_* = \frac{1}{\pi\tau_m\sqrt{2}}\sqrt{\bar{\eta} + \sqrt{\bar{\eta}^2 + \Delta^2}} \tag{1.55}$$

which is proportional to: the membrane time constant, $\tau$, the heterogeneity of the network, $\Delta$, and the mean excitatory (or inhibitory) current $\bar{\eta}$. Moreover, the decay time after the perturbations is given by the real part of the complex-valued eigenvalue (1.51):

$$\tau_{\text{decay}} = \frac{\pi\tau_m^2 R_*}{\Delta}, \tag{1.56}$$

which is inversely proportional to the heterogeneity of the network.

In the harmonic oscillator, the damped oscillations are consequence of the interplay between the restoring force, which drives the system back to the fixed point, and the dissipative effect produced by friction. In the QIF-FREs, the restoring force is given by the spike generation and reset mechanism whereas the "dissipative" effect is related to the diffusion of neurons' individual phases due to heterogeneity; a feature that is explicitly reflected in the decay time (1.56).

The existence of a natural frequency establishes the necessary substrate for the generation not only of oscillatory dynamics, but also for a variety of other non-linear dynamics, such as resonance.

### 1.3.5 QIF-FREs with synaptic kinetics

So far, the presented QIF-FR model has been derived from a fully-connected network of spiking neurons were synaptic transmission is assumed to be instantaneous. We have seen that even in this limit, heterogeneous networks of spiking neurons exhibit transient episodes of synchronization leading to macroscopic damped oscillations. A similar oscillatory behavior is often reported in traditional firing rate models (Wilson and Cowan, 1972; Knight, 1972) and neural mass models (Jansen and Rit, 1995). However, the mechanism responsible of generating the dumped oscillations in the latter case is fundamentally different to that seen in the network of QIF neurons. On one hand, fast transients in spiking neuronal networks are attributable to the synchronized response of neurons, a feature which is successfully captured by the QIF-FREs. On the other hand, traditional firing rate models reproduce similar dynamics by heuristically introducing an effective temporal delay in

the equations. In the original work of Wilson and Cowan (1972), damped oscillations appear in the full model prior to the time *coarse graining* approximation, i.e. when synaptic kinetics are taken into account. And a similar approach is followed in more general *integral-equation* approaches and neural-mass models. As a consequence, the temporal scales determining the frequency of the oscillatory behavior in each approach are different. In the first case, the temporal scale is determined by the membrane time constant of neurons $\tau_m$, while in the second case an additional time constant, $\tau_d$, is introduced tied to the dynamics of the synapses. In contrast, once the connectivity is suppressed the synaptic dynamics are irrelevant, and traditional firing rate models loose any possibility of showing oscillatory dynamics [Fig. 1.6(b)] as predicted by the linear stability analysis of Eq. (1.5).

Analytically, this can be proved by appropriately comparing the WC model with the QIF-FREs. First, we we must add synaptic kinetics to the latter set of equations, and then we apply the same approximation done at the moment of deriving the WC model (1.5), i.e. the time coarse-graining or the limit of slow synapses. The derivation of the firing rate equations of a network of QIF neurons with synaptic kinetics is fundamentally equal. The starting point is again the QIF neuron model [Eqs. (1.30), (1.31) and (1.33)], where we now introduce an additional ODE describing the temporal evolution of the synaptic activation as in (1.9),

$$\tau_d \frac{dS}{dt} = -S + R, \tag{1.57}$$

where $\tau_d$ is the synaptic time constant. Note that, the total synaptic activation $S$ is a mean-field quantity, and consequently a macroscopic magnitude. Therefore the derivation of the macroscopic equations is identical, which yields the following QIF-FREs,

$$\tau_m \frac{dR}{dt} = \frac{\Delta}{\pi\tau_m} + 2RV, \tag{1.58a}$$

$$\tau_m \frac{dV}{dt} = V^2 + \bar{\eta} + \tau_m J_0 S - (\pi\tau_m R)^2 + P(t), \tag{1.58b}$$

$$\tau_d \frac{dS}{dt} = -S + R. \tag{1.58c}$$

#### 1.3.5.1 The limit of slow synapses: a low-pass filtered version of Eqs. (1.58)

The limit of slow synapses can be studied by assuming that synaptic processes are much slower than neuron's intrinsic dynamics, i.e. $\tau_d \gg \tau_m$, where $\tau_d$ represents the synaptic decay time. To formally describe this situation we first consider the following rescaling: $\tilde{\tau}_d = \varepsilon\tau_d$ and $\tilde{t} = \varepsilon t$ leading to the following system

$$\begin{aligned}
\varepsilon\tau_m \frac{dR}{d\tilde{t}} &= \frac{\Delta}{\pi\tau_m} + 2RV, \\
\varepsilon\tau_m \frac{dV}{d\tilde{t}} &= V^2 + \bar{\eta} + \tau_m J_0 S - (\pi\tau_m R)^2 + P\left(\tilde{t}\right), \\
\varepsilon \frac{\tilde{\tau}_d}{\varepsilon} \frac{dS}{d\tilde{t}} &= -S + R.
\end{aligned}$$

Now, by taking $\varepsilon \to 0$, the left hand sides of Eqs. (1.58a) and (1.58b) vanish, recovering the expressions obtained for the fixed points, $R(t) = \Phi\left(\bar{\eta} + \tau_m J_0 S\right)$, with $\Phi(I)$ being the transfer function (1.50), and $V$ obeying the fixed point equation (1.48a). Thus, the system is reduced to a single differential equation describing the evolution of the synaptic activation, rather than the firing rate,

$$\tau_d \frac{dS}{dt} = -S + \Phi\left(\bar{\eta} + \tau_m J_0 S\right). \tag{1.59}$$

This proves that the QIF-FREs (1.47) and the WC equation (1.9) have the same dynamics in the limit of slow synapses. However, as we could observe in Fig. 1.6, perturbations applied to uncoupled populations also generated fast oscillatory transients which were not capture by WC equations. Hence, even in this limit, fast fluctuations in external inputs can drive spike synchrony in the network, and consequently the slow synaptic approximation of the QIF-FREs breaks down. This contributes to previously shown results in suggesting that a correct description of spiking networks requires keeping track of the mean sub-threshold voltage along with the mean firing rate. Moreover, the temporal scale of the dynamics is now characterized by the synaptic time constant $\tau_d$, rather than the membrane time constant $\tau_m$, showing that this limit is indeed a low-pass filtered version of the firing rate equations and only holds for slowly varying dynamics.

Hence, Eq. (1.59) cannot generate damped oscillations, as we require at least a second order differential equation. We therefore could consider

second order synaptic kinetics, also known as double exponential synapses:

$$\tau_r \tau_d \frac{d^2 S}{dt} + (\tau_d + \tau_r) \frac{dS}{dt} + S = R \tag{1.60}$$

where the new time constant $\tau_r$ corresponds to the synaptic rise time. If we take $\tau_d = \tau_r$ we recover the so-called *alpha synapse*. Following the same approach above, we obtain

$$\tau_d \tau_r \frac{d^2 S}{d^2 t} + (\tau_d + \tau_r) \frac{dS}{dt} = -S + \Phi\left(\bar{\eta} + \tau_m J_0 S\right). \tag{1.61}$$

This model is formally equal to the Canonical neural-mass models (Freeman, 1975; Jansen and Rit, 1995; Coombes et al., 2014).

Summarizing, Eqs. (1.59) and (1.61) describe the dynamics of a network of QIF neurons in the limit of slow, first-order and second-order synapses, respectively. As such, this limit assumes that both the firing rate and the mean membrane potential decay rapidly to their fixed point values. However, this reduction holds provided that external inputs $P(t)$ are also slow enough. For rapid time varying inputs, the slow synapses limit breaks down, as synchronous activity is hardly filtered by the synaptic processes. Finally, note that the WC equation with second order synapses (1.61) is also capable of generating oscillations.

### 1.3.6 Recent development on the QIF-FR model

We finish this chapter by briefly enumerating some of the most relevant results linked to the QIF-FREs (1.47). The derivation of this model is closely related to the development done in systems of coupled oscillators, and particularly to the effort made in obtaining low dimensional descriptions of such networks. The derivation of the QIF-FREs is indeed substantially equivalent to the work of Luke et al. (2013) where they obtained a low dimensional representation of a heterogeneous network of Theta neurons (1.29) in terms of the Kuramoto order parameter. As such, in the literature it is common to find works where instead of the QIF model, they build upon the Theta model. Nevertheless, the conformal map presented in (Montbrió et al., 2015) allows one to easily go from one macroscopic representation to the other.

Among the most relevant applications involving a low dimensional representation of a network of QIF neurons, Laing (2015) derived a neural field model for QIF neurons incorporating gap-junctions which are thought to be

relevant in facilitating the synchronized activity of networks of inhibitory neurons (Bennett and Zukin, 2004; Gibson et al., 1999). Additionally, Ratas and Pyragas (2016) studied the emergence of self-sustained macroscopic oscillations in networks of conductance-based* QIF neurons and explored the effects that aging transition has over them. The same authors studied symmetry breaking processes (see subsubsection 1.1.1.3) in a model of two interacting populations of QIF neurons (Ratas and Pyragas, 2017). Also focused on studying the effect of E-I interactions, Dumont et al. (2017) applied the macroscopic firing rate model to study the macroscopic phase response curve (mPRC) of an excitatory-inhibitory neural network.

Focusing on a single population of inhibitory QIF neurons Pazó and Montbrió (2016) studied the effect of delays in shaping synchronization and the arousal of collective chaos. Similarly, Devalle et al. (2017a) studied the emergence of ING oscillations (see section 1.1.1.1 and 1.2) in a network of recurrently coupled inhibitory neurons incorporating synaptic kinetics, and proved that a spike synchrony mechanism is required in order to generate them.

On the other hand, Roulet and Mindlin (2016) followed a similar approach as in (Luke et al., 2013) to derive a macroscopic description of a population of excitatory-inhibitory neural oscillators described in terms of Adler's equations, and they compared the resulting dynamics with WC equations (1.1). In a more applied work, Byrne et al. (2017) expanded the mean field reduction of the population of theta neurons to account for synaptic kinetics, and to model the modulation in beta rhythms observed during motor tasks, attributed to the change in the synchrony of the underlying neural population firing patterns. Although the modeling is done in terms of the Theta model and the Kuramoto order parameter, they apply the conformal map of (Montbrió et al., 2015) to obtain meaningful macroscopic quantities that allows them to compare their results with experimentally obtained measures of brain activity. In a similar fashion, Laing (2018) studied the dynamics of networks of identical sinusoidally-coupled theta neurons (and similar models) for both instantaneous and *delayed* synapses. In contrast to the previous works, he extensively used the Watanabe/Strogatz ansatz for reducing the dimension of the studied networks.

Finally, it is worth mentioning the work of Laing (2014) in developing a

*Following a similar approach as in Ratas and Pyragas (2016), in Appendix B.2 we derive the firing rate model for a network of QIF neurons with conductance-based synapses, and simulate a network of excitatory and inhibitory neurons displaying the aforementioned PING oscillations.

neural field model for a network of theta neurons following the derivation of (Luke et al., 2013). There, Laing considered the coupling to be mediated by "pulselike" functions. By means of the Ott-Antonsen ansatz (Ott and Antonsen, 2008) he obtained a complex-valued nonlocal partial differential equation describing the dynamics of the Kuramoto order parameter of the population of theta neurons.

In the following chapter we follow a similar approach to derive a neural field model of a network of QIF neurons allowing us to thoroughly study the synchronization-related phenomena observed in the spatially distributed network presented in 1.2, i.e. the decaying standing waves [Fig. 1.11].

CHAPTER 2

# Synchrony-induced modes of oscillation of a neural field model

Esnaola-Acebes, J. M., Roxin, A., Avitabile, D., and Montbrió, E. (2017). Synchrony-induced modes of oscillation of a neural field model. *Physical Review E*, 96(5):052407



> *"There is geometry in the humming of the strings. There is music in the spacing of the spheres."*
>
> — Pythagoras.

**Abstract:** We investigate the modes of oscillation of heterogeneous ring-networks of quadratic integrate-and-fire (QIF) neurons with non-local, space-dependent coupling. Perturbations of the equilibrium state with a particular wave number produce transient standing waves with a specific temporal frequency, analogously to those in a tense string. In the neuronal network, the equilibrium corresponds to a spatially homogeneous, asynchronous state. Perturbations of this state excite the network's oscillatory modes, which reflect the interplay of episodes of synchronous spiking with the excitatory-inhibitory spatial interactions. In the thermodynamic limit, an

exact low-dimensional neural field model (QIF-NFM) describing the macroscopic dynamics of the network is derived. This allows us to obtain formulas for the Turing eigenvalues of the spatially homogeneous state, and hence to obtain its stability boundary. We find that the frequency of each Turing mode depends on the corresponding Fourier coefficient of the synaptic pattern of connectivity. The decay rate instead is identical for all oscillation modes as a consequence of the heterogeneity-induced desynchronization of the neurons. Finally, we numerically compute the spectrum of spatially inhomogeneous solutions branching from the Turing bifurcation, showing that similar oscillatory modes operate in neural bump states and are maintained away from onset.

## 2.1 Introduction

Since the pioneering work of Wilson and Cowan (1973), Amari (1974, 1977), and Nunez (1974), continuum descriptions of neuronal activity have become a powerful modeling tool in neuroscience (Ermentrout, 1998; Coombes, 2005; Ermentrout and Terman, 2010; Bressloff, 2012; Coombes et al., 2014; Deco et al., 2008). Given that the number of neurons in a small region of cortex is very large, these descriptions consider neurons to be distributed along a continuous spatial variable and the macroscopic state of the network to be described by a single, space-dependent, firing rate variable. The resulting neural field model (NFM) generally has the form of a continuous first order integro-differential equation, greatly facilitating the computational and mathematical analysis of the dynamics of large neuronal networks.

NFMs do not generally represent proper mathematical reductions of the mean activity of a network of spiking neurons. Nevertheless, NFMs have proven to be remarkably accurate in qualitatively capturing the main types of dynamical states seen in networks of large numbers of asynchronous spiking neurons. For example, it is well known that, in local networks of spiking neurons, differences between excitatory and inhibitory neurons can lead to oscillations (Wilson and Cowan, 1972; Ermentrout, 1994; Brunel and Wang, 2003). The generation of these oscillations does not depend on the spatial character of the network and hence can be observed in non-spatially dependent firing rate models (Ermentrout, 1994). When the pattern of synaptic connectivity depends on the distance between neurons, NFMs show that these differences between excitation and inhibition can lead to the emergence of oscillations and waves (Amari, 1977; Pinto and Ermentrout,

2001a). Similar patterns can also be found in NFMs with spatially dependent delays —modeling the effect of the finite velocity propagation of action potentials (Wilson and Cowan, 1973; Jirsa and Haken, 1997)— as a great deal of theoretical work indicates (see e.g. Coombes et al., 2003; Atay and Hutt, 2004; Coombes and Laing, 2009; Zhang, 2007; Hutt, 2008; Touboul, 2012; Veltz, 2013; Dijkstra et al., 2015).

In some cases the spatiotemporal dynamics of NFMs has been directly compared to that observed in analogous networks of spiking neurons (Roxin et al., 2005; Battaglia et al., 2007; Roxin and Montbrió, 2011). In this work it was found that non-space-dependent delays predict the existence of many of the spatiotemporal patterns observed in asynchronous networks of spiking neurons with nonlocal, space-dependent interactions. The success of NFMs in describing these patterns depends crucially on the spiking activity being highly asynchronous. In fact, it is well known that neural field descriptions fail to describe states characterized by a high degree of spike synchronization (see e.g Schaffer et al., 2013).

Here we report a spatiotemporal dynamical feature of heterogeneous networks of spiking neurons with nonlocal interactions that, to the best of our knowledge, have been so far unexplored. We show that ring networks of spiking neurons display a number of discrete modes of oscillation, resembling those of a tense string. These modes are exclusively due to transient episodes of synchronous spiking and not due to the different time scales between excitation and inhibition or to the presence of any propagation or synaptic delay.

Traditional NFMs do not describe these synchrony-induced oscillations. Therefore, to investigate and characterize them, we apply a recent method to derive the firing rate equations of a globally coupled heterogeneous population of quadratic integrate-and-fire (QIF) neurons (Montbrió et al., 2015). This method, based on the so-called Ott-Antonsen theory (Ott and Antonsen, 2008, 2009; Ott et al., 2011), leads to an exact macroscopic description of the network in terms of two macroscopic variables: the mean firing rate and the mean membrane potential. The resulting mean-field model exactly describes any state of the system, including synchronous states. Here we extend the local firing rate model in (Montbrió et al., 2015), to include nonlocal, instantaneous interactions. The resulting neural field model for heterogeneous QIF neurons (QIF-NFM) clearly displays the synchrony-induced oscillatory modes observed in simulations of spiking neurons. We then thoroughly investigate the QIF-NFM by means of both a linear and nonlinear stability analysis of the spatially homogeneous state. The analysis

reveals the presence of an infinite number of oscillation modes, linked to the Fourier components of the spatial pattern of synaptic connections. The analysis also shows that all modes decay to the unpatterned state with the same rate, which depends on the degree of heterogeneity in the network. Finally, we investigate the spectrum of the spatially inhomogeneous solutions of the QIF-NFM and find similar oscillatory modes also linked to transient episodes of spike synchronization.

## 2.2 Synchrony-induced modes of oscillation in Networks of QIF Neurons

Figure 2.1(a) shows a schematic representation of the spiking neuron network under investigation. The model consists of $N$ excitatory (red triangles) and $N$ inhibitory (blue circles) neurons evenly distributed in a ring and characterized by the spatial discrete variables $\phi_j \in [-\pi, \pi)$ with $\phi_j = \frac{2\pi j}{N} - \pi,\ j = 1, \ldots, N$, as shown in Fig. 2.1(a). Any neuron in the network interacts with all the other neurons via the distance-dependent coupling function $J^{e,i}_{jk} = J^{e,i}(|\phi_j - \phi_k|)$, where indices $e, i$ denote excitatory and inhibitory connections, respectively. The synaptic projections of the $j$th excitatory and inhibitory neurons (located at $\phi_j$) to other two nearby neurons are also schematically represented in Fig. 2.1(a).

The ring architecture of the network allows one to express the excitatory and inhibitory connectivity patterns in Fourier series as

$$J^{e,i}(\phi) = J^{e,i}_0 + 2\sum_{K=1}^{\infty} J^{e,i}_K \cos(K\phi). \tag{2.1}$$

Figure 2.1(b) shows a particular synaptic connectivity pattern in which excitatory neurons form strong, short-range connections, whereas inhibitory projections are weaker and wider. The state of the excitatory ($e$) and inhibitory ($i$) neurons is determined by the (dimensionless) membrane potentials $\{v^{e,i}_j\}_{j=1,\ldots,N}$, which are modeled using the Quadratic Integrate and Fire (QIF) model Ermentrout and Kopell (1986); Izhikevich (2007)

$$\tau \frac{dv^{e,i}_j}{dt} = (v^{e,i}_j)^2 + I^{e,i}_j, \quad \text{(+ resetting rule)}. \tag{2.2}$$

where $\tau$ is the cell's membrane time constant and $v_r$ and $v_p$ correspond to the reset and peak potentials of the QIF neurons, respectively —in numerical simulations we consider $\tau = 20$ ms.

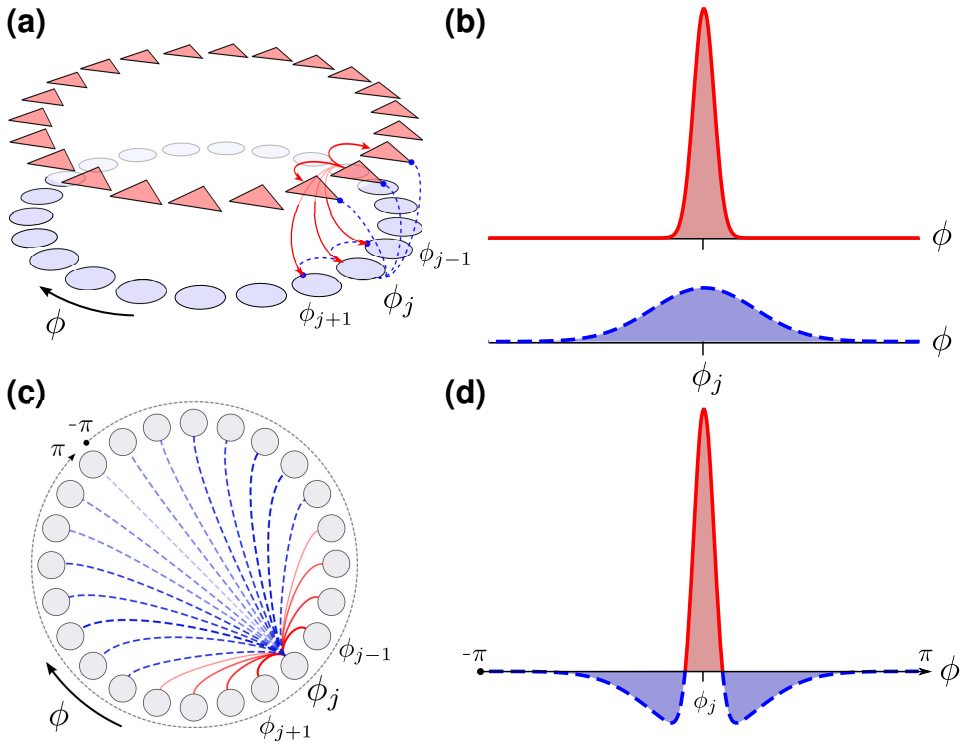


**Figure 2.1:** Schematic representation of the ring network and coupling architecture under study. Panel (a) shows $N$ excitatory (red triangles) and $N$ inhibitory (blue circles) neurons arranged on a ring. The location of neurons is parameterized by the angular variable $\phi_j = \frac{2\pi j}{N} - \pi$, $j = 1, \ldots, N$. Red (solid) and blue (dashed) lines indicate synaptic connections between neuron pairs $(\phi_j, \phi_k)$. An example of the excitatory and inhibitory space-dependent connectivity kernels Eqs. (2.1) are shown in panel (b) where the abscissa represents the distance $|\phi_k - \phi_j|$ between neurons $j$ and $k$. Panel (c) represents an effective model in which pairs of excitatory/inhibitory neurons located at a certain location $\phi_k$ are modeled as single neurons. The effective pattern of synaptic connectivity is obtained subtracting the inhibitory pattern from the excitatory one, as show in panel (d).

The QIF neuron has two possible dynamical regimes depending on the (dimensionless) input current $I_j^{e,i}$. If $I_j^{e,i} < 0$, the neuron is in the excitable regime, while for $I_j^{e,i} > 0$ the neuron is in the oscillatory regime. In the excitable regime, an initial condition $v_j^{e,i}(0) < \sqrt{-I_j^{e,i}}$, asymptotically approaches the resting potential $-\sqrt{-I_j^{e,i}}$. On the other hand, initial conditions above the excitability threshold, $v_j^{e,i}(0) > \sqrt{-I_j^{e,i}}$, lead to an un-

bounded growth of the membrane potential. Specifically, if $v_j^{e,i}(0) \gg \sqrt{I_j^{e,i}}$, then the membrane potential reaches infinity approximately after a time $\tau/v_j^{e,i}(0)$. In practice, to avoid this divergence, we consider the following resetting rule: When the neuron's membrane potential $v_j^{e,i}$ reaches a certain peak value $v_p \gg 1$, the neuron is reset to a the new value $v_r = -v_p$ after a refractory period $2\tau/v_p$. On the other hand, if $I_j^{e,i} > 0$, then the neuron is in the oscillatory regime and needs to be reset periodically. If $v_p \gg 1$, the frequency of the oscillatory neurons is approximately $f_j = \sqrt{I_j}/(\tau\pi)$. Finally, the current $I_j^{e,i}$ is defined as

$$I_j^{e,i} = \eta_j^{e,i} + \tau S_j^e(t) + \tau S_j^i(t) + P_j^{e,i}(t). \tag{2.3}$$

Here, $\eta_j^{e,i}$ is a constant external current, which varies from neuron to neuron. The terms $P^{e,i}(t)$ are time-varying common inputs, and $S_j^{e,i}(t)$ are the mean excitatory (positive) and inhibitory (negative) synaptic activities representing all the weighted inputs received by neuron $j$ due to spiking activity in the network:

$$S_j^{e,i}(t) = \pm \sum_{k=1}^{N} \frac{J_{jk}^{e,i}}{2\pi N} \sum_{l \backslash t_k^l < t} \frac{1}{\tau_s} \int_{t-\tau_s}^{t} dt' \delta^{e,i}(t' - t_k^l), \tag{2.4}$$

where $\tau_s$ represents the synaptic processing time and $t_k^l$ is the time of the $l$th spike of the excitatory/inhibitory $k$th neuron. Positive and negative signs correspond to $S_j^e$ and to $S_j^i$, respectively.

We performed numerical simulations of the QIF model Eqs. (2.2) and (2.3) for a network of heterogeneous neurons, see Fig. 2.2, and Appendix 2.D for details of the numerical simulations. In all cases, the system is initially at a spatially homogeneous state (SHS). At time $t = 50$ ms, a brief (10 ms) and small current pulse $P_j^e$ is applied either to all excitatory neurons [Figs. 2.2(a) and 2.2(b)] or to both excitatory and inhibitory neurons. The left and right panels show perturbations of the first spatial modes, respectively —see Appendix D for the specific form of the perturbations. Note that, after the perturbation, the system decays to the homogeneous state showing oscillations, which resemble standing waves. Note that the frequency of these oscillations is different for each mode, while the decay rate is similar in the two cases. We also performed simulations of networks of QIF neurons (i) with quenched Gaussian heterogeneity (ii) subject to independent Gaussian noise processes, and found similar results (not shown). To the best of our knowledge, these oscillations have not yet been investigated in the literature.

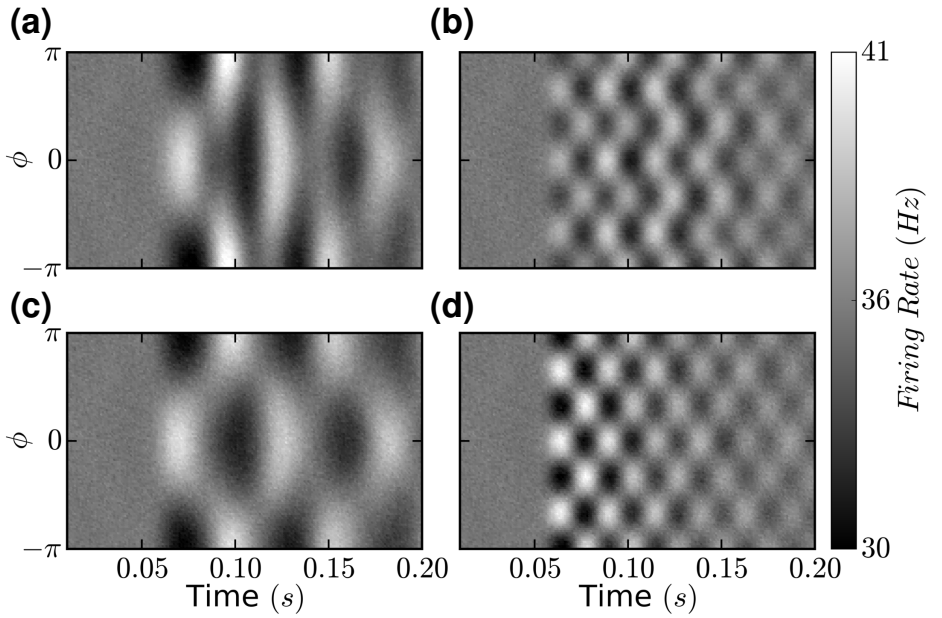


**Figure 2.2:** Transient episodes of spike synchrony in heterogeneous ring networks of $N = 2.5 \cdot 10^5$ excitatory and $N = 2.5 \cdot 10^5$ inhibitory QIF neurons, Eqs. (2.2) and (2.3), as a result of spatially inhomogeneous perturbations applied at time $t = 0.05$ s. In Panels (a) and (b) only excitatory neurons are perturbed. In panels (c) and (d) all neurons are perturbed. In panels (a) and (c) the perturbation has wave number $K = 1$; in panels (b) and (d) the perturbation has wave number $K = 3$. Other parameters are $\Delta = 1$, $\tau = 20$ ms, and $\bar{\eta} = 5$. All Fourier components of the connectivity Eq. (2.1) were $J_K^{e,i} = 0$, except $J_0^e = 23$, $J_1^e = 10$, $J_2^e = 7.5$, $J_3^e = -2.5$, $J_0^i = 23$.

## 2.3 Neural Field model for quadratic integrate and fire neurons

In the following, we aim to investigate the nature and origin of the spatiotemporal patterns shown in Fig. 2.2. To analyze them, we derive the NFM corresponding to the thermodynamic ($N \to \infty$) and continuum limits of the network of QIF neurons [Eqs. (2.2) and (2.3)]. In additon we also take the limit $v_p \to \infty$, so that the QIF model (2.2) is equivalent to the so-called theta-neuron model (Ermentrout and Kopell, 1986; Izhikevich, 2007). This leads to an exact neural field model for a network of QIF neurons (QIF-NFM). The detailed derivation is performed in Appendix 2.A, and closely

follows that of Montbrió et al. (2015). The reduction in dimensionality is achieved considering that the currents $\eta^{e,i}$ —which, after performing the thermodynamic limit, become continuous random variables— are distributed according to a Lorentzian distribution of half-width $\Delta$ and centered at $\bar{\eta}$,

$$g(\eta^{e,i}) = \frac{\Delta}{\pi} \frac{1}{(\eta^{e,i} - \bar{\eta})^2 + \Delta^2}. \tag{2.5}$$

The QIF-NFM is

$$\begin{aligned} \tau \frac{\partial R^{e,i}}{\partial t} &= \frac{\Delta}{\pi\tau} + 2R^{e,i}V^{e,i}, & \text{(2.6a)} \\ \tau \frac{\partial V^{e,i}}{\partial t} &= (V^{e,i})^2 + \bar{\eta} - (\pi\tau R^{e,i})^2 + \tau S(\phi) \\ &\quad + P^{e,i}(\phi, t). & \text{(2.6b)} \end{aligned}$$

and exactly describes the time evolution of the mean firing rate $R^{e,i}(\phi)$ and the population's mean membrane potential $V^{e,i}(\phi)$ of the excitatory and inhibitory populations at any location $\phi$ of the ring —to facilitate the notation we have avoided explicitly writing the dependence of these variables on $\phi$. In the limit of instantaneous synapses, $\tau_s \to 0$ in Eqs. (2.4), the excitatory and inhibitory contributions of the mean field $S(\phi) = S^e(\phi) + S^i(\phi)$ reduce to $S^{e,i}(\phi) = \pm \frac{1}{2\pi} \int_{-\pi}^{\pi} J^{e,i}(\phi - \phi') R^{e,i}(\phi') d\phi'$.

### 2.3.1 Effective QIF-NFM

The analysis of the QIF-NFM Eq. (2.6) is greatly simplified considering that excitatory and inhibitory neurons have identical single-cell properties. This scenario is schematically represented in Figs. 2.1(c) and 2.1(d). If we set $P^e(\phi, t) = P^i(\phi, t) = P(\phi, t)$, and restrict our attention to solutions of Eqs. (2.6) satisfying $R^e(\phi, t) = R^i(\phi, t) \equiv R(\phi, t)$ and $V^e(\phi, t) = V^i(\phi, t) \equiv V(\phi, t)$, then we obtain an effective QIF-NFM in variables $R$ and $V$,

$$\begin{aligned} \tau \frac{\partial R}{\partial t} &= \frac{\Delta}{\pi\tau} + 2RV, & \text{(2.7a)} \\ \tau \frac{\partial V}{\partial t} &= V^2 + \bar{\eta} - (\pi\tau R)^2 + \tau S(\phi) + P(\phi, t). & \text{(2.7b)} \end{aligned}$$

In this case, the mean field reduces to

$$S(\phi) = \frac{1}{2\pi} \int_{-\pi}^{\pi} \left[ J_0 + 2 \sum_{K=1}^{\infty} J_K \cos(K(\phi' - \phi)) \right] R(\phi') d\phi', \tag{2.8}$$

with the new Fourier coefficients $J_K$, which are related to those in Eq. (2.1) as $J_K = J_K^e - J_K^i$, with $K = 0, 1, \ldots$, see Fig. 2.1(d). Solutions to Eqs. (2.6) need not satisfy the condition $R^e = R^i$ and $V^e = V^i$, but the reduced system Eqs. (2.7) captures the mechanism behind the oscillatory behavior observed in the model. Note that, in Figs. 2.2(a) and 2.2(b), we perturbed the (SHS) of the system [Eqs. (2.2) and (2.3)] using a current pulse to all excitatory neurons. The resulting dynamics is only captured by the full system [Eqs. (2.6)] and not by the effective neural field [Eqs. (2.7)]. However, we next show that the existence of the spatial oscillatory modes observed in Fig. 2.2 is exclusively linked to the dynamics in the reduced manifold defined by Eqs. (2.7) and (2.8).

### 2.3.2 SHS and their stability: Synchrony-induced modes of oscillation

In the following we investigate the stability of the stationary SHS of the QIF-NFM against spatial perturbations. The detailed linear stability analysis of both the complete model [Eqs. (2.6)], and the reduced one [Eqs. (2.7)] are provided in Appendix 2.B.

In absence of external inputs, $P(\phi, t) = 0$, the steady states of Eqs. (2.7) —and also of Eqs. (2.6)—satisfy $V_*(\phi) = -\Delta/[2\pi\tau R_*(\phi)]$, and

$$R_*(\phi) = \Phi\left(\bar{\eta} + \tau S_*(\phi)\right) \tag{2.9}$$

with $\Phi(x) = \sqrt{x + \sqrt{x^2 + \Delta^2}}/(\sqrt{2}\pi\tau)$. In Eq. (2.9), the term $S_*(\phi)$ is the mean field [Eq. (2.8)] evaluated at $R_*(\phi)$. For SHS, the mean field [Eq. (2.8)] becomes spatially independent, $S_*(\phi) = S_* = J_0 R_*$, and Eq. (2.9) becomes a quartic equation for the variable $R_*$. To further simplify the analysis, hereafter we consider parameter ranges where Eq. (2.9) has a single positive root. Accordingly, we consider a balanced kernel, $J_0 = 0$ so that Eq. (2.9) has $S_* = 0$ and explicitly determines the value of the fixed point $R_*$.

The steady states of the SHS of Eq.(2.7) coincide with those of a single population of neurons (Montbrió et al., 2015). However, the stability of the SHS of the QIF-NFM to inhomogeneous perturbations depends on the spatial character of the connectivity kernel Eq. (2.1). The linear stability analysis of the SHS gives a countably infinite set of eigenvalues associated

to the stability of perturbations with wave number* $K$.

$$\lambda_{K\pm} = -\frac{\Delta}{\pi\tau^2 R_*} \pm 2\pi R_* \sqrt{\frac{J_K}{2\pi^2\tau R_*} - 1},\ (K = 0, 1, 2\dots) \qquad (2.10)$$

This equation is the main result of this work, and explains the synchronization patterns shown in Fig. 2.2. Note that the eigenvalues Eq. (2.10) may be real or complex, indicating nonoscillatory or oscillatory dynamics of the evolution of perturbations of wave number $K$, respectively. In particular, perturbations of any given spatial mode $K$ are oscillatory if the condition $J_K < 2\pi^2\tau R_*$ is fulfilled. Notably, all complex eigenvalues have the same decay rate to the SHS, since $\mathrm{Re}(\lambda_{K\pm}) = -\Delta/(\pi\tau^2 R_*)$ for all of them. Specifically, the decay rate is proportional to the degree of quenched heterogeneity $\Delta$. This reflects the fact that the decay in the oscillations is in fact a desynchronization mechanism due to the distribution of inputs that the cells receive.

Substituting Eq. (2.9) with $J_0 = 0$ into Eq. (2.10), it is straightforward to find the boundary

$$J_K^o = \sqrt{2}\pi\sqrt{\bar{\eta} + \sqrt{\bar{\eta}^2 + \Delta^2}}, \qquad (2.11)$$

separating the parameter space into regions where standing waves of wave number $K$ are, or are not, observed. This boundary is depicted with a dotted line in the phase diagram Fig. 2.3, together with a schematic representation of the location of the eigenvalues $\lambda_{K\pm}$ in the complex plane (red crosses, see also Fig. 2.5(a)). A given oscillatory mode $K$ has an associated frequency

$$\nu_K = \frac{1}{2\pi}|\mathrm{Im}(\lambda_{K\pm})|,$$

which differs from one another depending on the corresponding Fourier coefficients $J_K$ of the patterns of synaptic connectivity Eq. (2.1). Therefore, spatial perturbations of wave number $K$ produce standing waves of neural activity of frequency $\nu_K$. Locally excitatory coupling $J_K > 0$ slows down

* The stability analysis of the original Eqs. (2.6) gives two additional complex eigenvalues for each oscillatory mode $K$. These eigenvalues are degenerated and are associated to the oscillatory modes of the uncoupled neuronal system, that is they coincide with (2.10) with $J_K^{e,i} = 0$. Additionally, due to the translational invariance of the SHS solutions, each of the eigenvalues Eq. (2.10) is two-times degenerated, corresponding to even and odd perturbations. See Appendix 2.B for the detailed linear stability analysis of the QIF-NFM Eqs. (2.6).

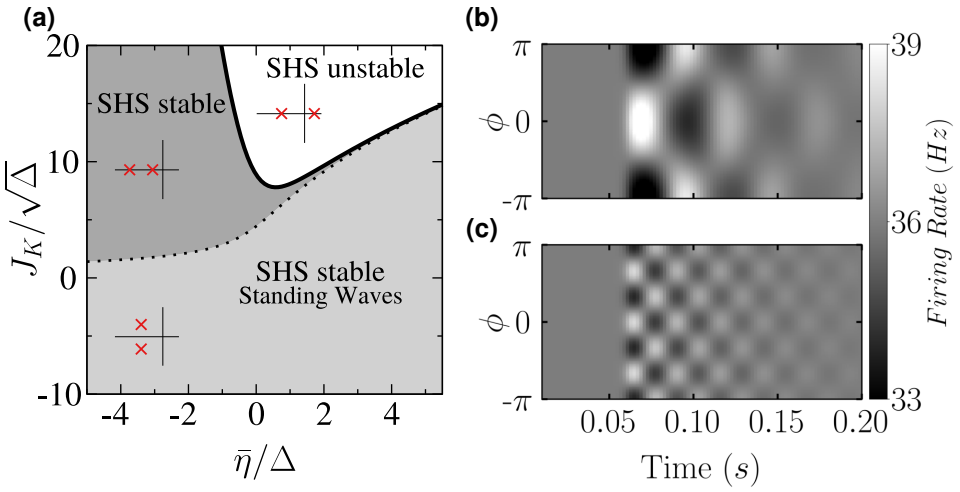


**Figure 2.3:** (a) Phase diagram of Eqs. (2.7) (with $J_0 = 0$) showing the regions of stability of the SHS, determined by the eigenvalues Eq. (2.10). Spatial perturbations of wave number $K > 0$ show oscillatory and nonoscillatory decay to the spatially homogeneous state in the light-shaded and dark-shaded regions of the diagram, respectively. The eigenvalues $\lambda_{K\pm}$ associated with the $K$th mode are schematically represented in the complex plane (red crosses) for the three qualitatively different regions of the phase diagram. Right panels show the response of the Eqs. (2.7) with $J_1 = 10$, $J_2 = 7.5$, $J_3 = -2.5$ and $J_K = 0$ ($K \neq 1, 2, 3$), $\bar{\eta} = 4.5$, $\Delta = 1$, and $\tau = 20$ ms, to a perturbation of the (b) $K = 1$ and (c) $K = 3$ spatial modes. Both perturbations produce standing waves with frequency and decay rate described by Eqs (2.10). In the white region, limited by the curve Eq. (2.11), these perturbations grow and lead to a bump state (BS) with $K$ bumps (see Fig. 2.4).

these oscillations and eventually suppresses them, whereas locally inhibitory coefficients $J_K < 0$ are able to generate arbitrarily fast oscillations (in particular, note that all modes with $J_K = 0$ are oscillatory with frequency $\nu = R_*$, which coincides with the mean firing rate of the uncoupled neurons).

Indeed, in Fig. 2.2(d), a perturbation of wave number $K = 3$ produced standing waves, since $J_3$ was negative. The frequency of these oscillations was fast compared to that of Fig. 2.2(c), where the exited mode was the first one $K = 1$ and given that the $J_1$ was positive. However, note that in both cases the decay to the SHS is similar, as predicted by the eigenvalues Eq. (2.10). This indicates that the desynchronization process occurs faster when the diversity $\Delta$ of neurons is increased, and this process does not depend on the oscillation mode being excited. Finally, in Figs. 2.3(b) and 2.3(c) we show numerical simulations of the QIF-NFM [Eq. (2.7)] using

the same parameters as those of Fig. 2.2(c) and 2.2(d), and the agreement is good.

### 2.3.3 Turing bifurcation and nonlinear stability of the SHS

As $J_K$ is increased, the frequency $\nu_K$ of a given oscillatory mode decreases and eventually it ceases to oscillate. Further increases in $J_K$ may destabilize the homogeneous state, via a pattern-forming (Turing) bifurcation. This instability leads to states with spatially modulated firing rate, sometimes referred to as Bump States (BS). Substituting the fixed point (2.9) in Eq. (2.10), and imposing the condition of marginal stability $\lambda_{K+} = 0$, we find the stability boundaries corresponding to a $K$-spatial mode

$$J_K^T = 2\pi \sqrt{\frac{2\bar{\eta}^2 + 2\Delta^2}{\bar{\eta} + \sqrt{\bar{\eta}^2 + \Delta^2}}}. \tag{2.12}$$

The Turing bifurcation boundary, Eq. (2.12), corresponds to the solid line in Figs. 2.3(a) and 2.4(a). Additionally, in Appendix 2.C, we conducted a weakly nonlinear analysis and derived the small-amplitude equation [Eq. (2.C.20)] corresponding to the bump solution bifurcating from the SHS. The amplitude equations determine if the Turing bifurcation is supercritical, or if it is subcritical and bistability between SHS and bump states is expected to occur. The results of this analysis are summarized in Fig. 2.4(b).

In addition, we performed numerical simulations of the QIF-NFM (2.7) and indeed found coexistence of SHS and bump states in the blue-shaded regions limited by solid and dashed curves in Fig. 2.4(a). These lines meet at two codimension-2 points (where the Turing bifurcation line changes color) that agree with the results of the weakly nonlinear analysis. Moreover, we computed numerically a bifurcation diagram of the NFM, using the spectral method developed in (Rankin et al., 2014) and available with (Avitabile, 2016). The results, presented in Fig. 2.4(c) confirm that the unstable BS bifurcates subcritically for the SHS. The unstable BS then meets a stable BS —solid blue (light gray) line— at a fold bifurcation.

### 2.3.4 Synchrony-induced transient oscillations in bump states

To investigate whether the synchrony-induced oscillatory modes are also present in the stationary BS, we computed their spectrum. The gray points

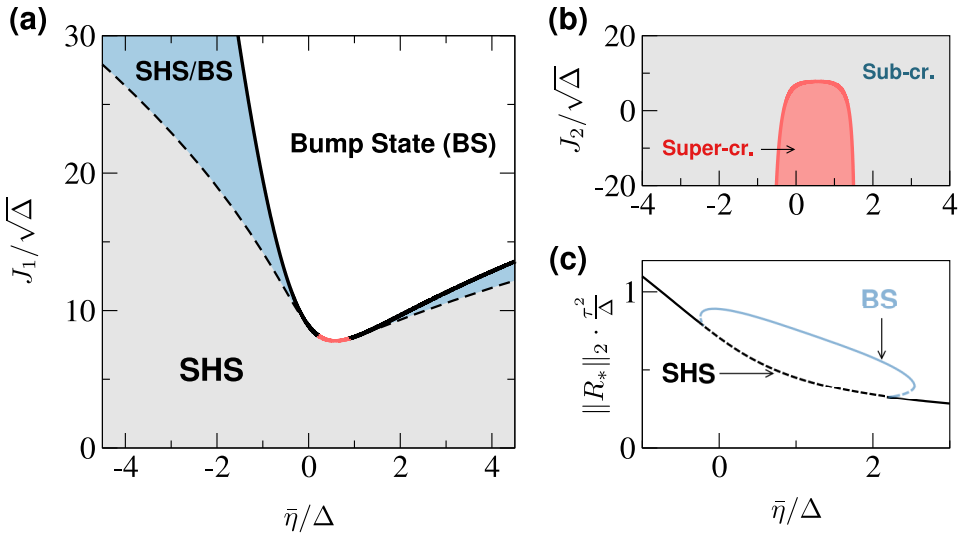


**Figure 2.4:** (a) Phase diagram of the QIF-NFM [Eqs. (2.7)] with $J_2 = 7.5$, $J_3 = -2.5$, $J_K = 0$ for $K > 3$, and $\Delta = 1$. Solid line: Supercritical [red (gray)] and Subcritical (black) Turing bifurcation boundary Eq. (2.12). Dashed lines: saddle-node bifurcation of bumps (numerical). (b) Diagram —obtained using a weakly nonlinear analysis— showing the regions where the Turing bifurcation is supercritical or subcritical for $J_1 = 10$, $J_3 = -2.5$, and $J_K = 0$. (c) Bifurcation diagram (rescaled) $\|R_*\|_2 = (2\pi)^{-1} \int_{-\pi}^{\pi} |R_*(\phi)|^2 d\phi$ vs. $\bar{\eta}$, for $J_1 = 10$. Solid/dashed black lines: stable/unstable SHS. Solid/dashed blue lines: stable/unstable bump states (BS).

in Fig. 2.5(a) show the spectrum of the unstable Bump near the subcritical Turing bifurcation of wave number $K = 1$. Additionally, the red crosses in Fig. 2.5(a) are the eigenvalues of the SHS state Eq. (2.10). The profile of the unstable bump is only very weakly modulated, see Fig. 2.5(c), and hence the spectrum of the BS is very close to that of the SHS, given by the eigenvalues $\lambda_K$. All these eigenvalues are complex, except two real eigenvalues, which correspond to the $K = 1$ mode. One of these eigenvalues is negative and the other is very close to zero and positive, indicating that the SHS is unstable.

Additionally, it is important to note that in Fig. 2.5 we have taken $J_K = 0$ for all $K$ except for $K = 1, 2, 3$, and hence there is an infinite number of eigenvalues ($\lambda_0$ and $\lambda_{4,5,\ldots}$) that are all complex and identical. In Fig. 2.5(a) the eigenvalues of the unstable BS seem to form a continuous band precisely around these infinitely degenerated eigenvalues and their complex conjugates. These continuous bands grow in size as one moves away from

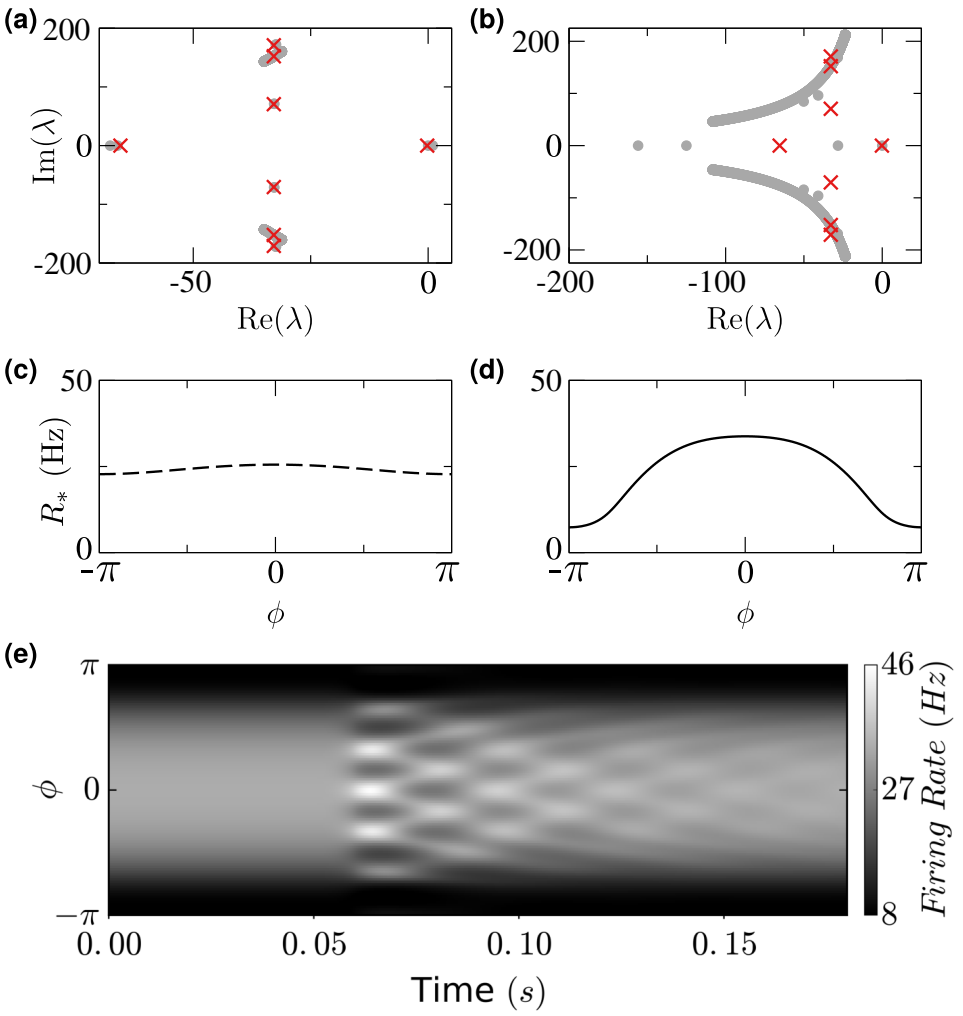


**Figure 2.5:** Spectrum [(a) and (b)] and firing rate profiles [(d) and (c)] of an unstable [(a) and (c)] and stable [(b) and (d)] bump states of the QIF-NFM [Eqs. (2.7)]. In panels (a) and (b) the eigenvalues Eq. (2.10) are superimposed with red crosses. Panel (e) shows a numerical simulation of the BS of panel (d). At $t = 0.05$ s, a perturbation of wave number $K = 6$ is applied. Parameters are $J_0 = 0$, $J_1 = 10$, $J_2 = 7.5$, $J_3 = -2.5$, $J_K = 0$ for $K > 3$, $\Delta = 1$, $\tau = 20$ ms. Panels (a) and (c): $\bar{\eta} = 2.2120$; panels (b), (d) and (e): $\bar{\eta} = 2.1828$.

the Turing bifurcation, as it can be seen in the spectrum of the stable bump depicted in Fig. 2.5(b) —here red crosses also correspond to the eigenvalues of the SHS state Eq. (2.10). These results show that all the complex eigenvalues linked to the oscillatory modes of the SHS remain complex, suggesting

that, in general, similar synchronization-induced oscillations may be present in stationary, spatially inhomogeneous neural patterns.

Finally, to illustrate this, in Fig. 2.5(e) we performed a numerical simulation of the QIF-NFM Eqs. (2.7), and perturbed the BS shown in Fig. 2.5(d) with a spatially inhomogeneous perturbation corresponding to the mode ($K = 6$). The perturbation decays to the BS showing a pattern that resembles that of Fig. 2.2. However here, the regions of the ring with the maximum values of $R_*$ —around $\phi = 0$, in Figs. 2.2(d) and 2.2(e)— oscillate at high frequencies and these oscillations slow down as $\phi \to \pm\pi$. The spectrum of the stable BS Fig. 2.5(b) also indicates that the decay of the fast oscillations (located at the central part of the bump, $\phi = 0$) is slow compared to that of the slow oscillations.

## 2.4 Conclusions

We have reported the existence of a class of oscillatory modes in spatially distributed networks of heterogeneous spiking neurons. These modes of oscillation reflect the transient episodes of spike synchronization among the neurons and are not captured by traditional NFMs.

To investigate these oscillation modes we derived a novel NFM for QIF neurons [Eqs. (2.6)]. Alternately, and invoking the Ott-Antonsen theory for populations of pulse-coupled theta neurons (Luke et al., 2013; So et al., 2014), Laing (2014) recently derived a NFM that is equivalent to the effective QIF-NFM. In Laing's work—like in other recent related papers on pulse-coupled oscillators (Pazó and Montbrió, 2014; O'Keeffe and Strogatz, 2016; Chandra et al., 2017; Coombes and Byrne, 2019; Byrne et al., 2017; Gallego et al., 2017)— the resulting low-dimensional description is in terms of the complex Kuramoto order parameter. In contrast, the mean field description adopted here (in terms of mean firing rates and membrane potentials) greatly simplifies the analysis, allowing us to analytically investigate the linear and nonlinear stability of the spatially homogeneous states of the QIF-NFM.

This analysis reveals two important features: (i) The frequency of each oscillation mode only depends on the corresponding Fourier coefficient of the synaptic pattern of connectivity, and (ii) the decay rate is exactly the same for all modes and is due to a desynchronization mechanism which depends on the degree of quenched heterogeneity. We also numerically investigated networks of identical QIF neurons subject to noise and found similar results (not shown). In this case, the desynchronization reflects an

underlying phase diffusion proportional to the noise strength. Finally, we investigated the existence and stability of bump states, which bifurcate from the spatially homogeneous states via Turing bifurcations. The spectrum of such bump states has a continuous part off the real axis, indicating that similar synchronization-induced oscillatory modes also operate in neural bump states.

Interesting directions of further study are the analysis of the QIF-NFM [Eq. (2.6)] considering different membrane time constants $\tau$, (or different main currents $\bar{\eta}$) for excitatory and inhibitory neurons. As proved recently (Avitabile et al., 2017), NFMs with time-scale separation display a rich variety of robust spatiotemporal patterns, which may also be supported by our model. Also, recent work has been done to extend the local firing rate equations derived in (Montbrió et al., 2015) to include fixed synaptic delays (Pazó and Montbrió, 2016) and synaptic kinetics (Ratas and Pyragas, 2016; Devalle et al., 2017a)—see also (Coombes and Byrne, 2019; Byrne et al., 2017). This work shows that time delays due to synaptic processing generally lead to the emergence of self-sustained oscillations due to collective synchronization. Extending the QIF-NFM [Eq. (2.6)] to account for the synaptic time delays caused by synaptic processing may lead to spatiotemporal phenomena not previously observed in traditional NFMs.

# Chapter Appendices

## 2.A Derivation of the QIF neural field model (QIF-NFM)

Our derivation closely follows that of (Montbrió et al., 2015), but it needs to be extended to include the spatial dimension. Similar extensions from a single population of phase oscillators to a one-dimensional, spatially distributed network with nonlocal coupling have been done in (Laing, 2014, 2015, 2016b,a, 2009; Omel'chenko, 2013; Omel'chenko et al., 2014; Kawamura, 2014).

Considering the thermodynamic limit $N \to \infty$, we can drop the indexes in Eqs. (2.2) and (2.3) and define the density function $\rho^{e,i}(v^{e,i}|\eta^{e,i}, t, \phi)$ such that $\rho^{e,i}(v^{e,i}|\eta^{e,i}, t, \phi)dv^{e,i}d\eta^{e,i}d\phi$ describes the fraction of neurons located between $\phi$ and $\phi+d\phi$, with membrane potentials between $v^{e,i}$ and $v^{e,i}+dv^{e,i}$ and parameters between $\eta^{e,i}$ and $\eta^{e,i} + d\eta^{e,i}$ at time $t$. Accordingly, parameter $\eta^{e,i}$ becomes now a continuous random variable with probability density function $g(\eta^{e,i})$. For the sake of simplicity, we assume identical distributions for both excitatory and inhibitory populations $g\left(\eta^{e,i}\right) = g\left(\eta\right)$. The total voltage density at location $\phi$ and time $t$ is given by $\int_{-\infty}^{\infty} \rho^{e,i}(v^{e,i}|\eta, t, \phi)\ g(\eta)\ d\eta$.

Conservation of the number of neurons at each $\phi$ value is described by the continuity equation

$$\partial_t \rho^{e,i} = -\partial_v \left[ \left( \left(v^{e,i}\right)^2 + \eta + \tau S(\phi, t) + P^{e,i}(\phi, t) \right) \rho^{e,i} \right],$$

where we have explicitly included the velocity given by Eqs. (2.2) and (2.3) and $S\left(\phi, t\right) = S^e\left(\phi, t\right) + S^i\left(\phi, t\right)$ represents the total synaptic activity. Next we invoke the Ott-Antonsen theory (Ott and Antonsen, 2008), by means of the Lorentzian Ansatz (LA) (Montbrió et al., 2015)

$$\rho^{e,i}(v^{e,i}|\eta, t, \phi) = \frac{1}{\pi} \frac{x^{e,i}(\phi, \eta, t)}{\left[v^{e,i} - y^{e,i}(\phi, \eta, t)\right]^2 + x^{e,i}(\phi, \eta, t)^2}, \tag{2.A.1}$$

which solves the continuity equation. The width $x^{e,i}(\phi, \eta, t)$ of the LA is related to the firing rate $R^{e,i}$ of the neural populations. Indeed, for each $\eta$ value at time $t$, $R^{e,i}(\phi, \eta, t)$ can be evaluated noting that neurons fire at a rate given by the probability flux at infinity: $R^{e,i}(\phi, \eta, t) = \rho^{e,i}(v^{e,i} \to \infty|\eta, t, \phi)\dot{v}^{e,i}(v^{e,i} \to \infty|\eta, t, \phi)$. The limit $v^{e,i} \to \infty$ on the right-hand side

of this equation can be evaluated within the LA and gives: $x^{e,i}(\phi,\eta,t) = \pi\tau R^{e,i}(\phi,\eta,t)$. The total firing rate at a particular location $\phi$ of the ring is then

$$R^{e,i}(\phi,t) = \frac{1}{\tau\pi}\int_{-\infty}^{\infty} x^{e,i}(\phi,\eta,t)g(\eta)d\eta. \tag{2.A.2}$$

Additionally, the quantity $y^{e,i}(\eta,t)$ is, for each value of $\eta$, the mean of the membrane potential $y^{e,i}(\phi,\eta,t) = \text{P.V.}\int_{-\infty}^{\infty}\rho^{e,i}(v^{e,i}|\eta,t,\phi)v^{e,i}\,dv^{e,i}$. Therefore, this variable is related to the mean membrane potential of the neuronal population at $\phi$ by

$$V^{e,i}(\phi,t) = \int_{-\infty}^{\infty} y^{e,i}(\phi,\eta,t)g(\eta)d\eta. \tag{2.A.3}$$

Substituting the LA (2.A.1) into the continuity equation, we find that, for each value of $\eta$, the variables $x^{e,i}(\phi)$ and $y^{e,i}(\phi)$ must obey two coupled equations which can be written in complex form as

$$\begin{aligned}\tau\partial_t w^{e,i}(\phi,\eta,t) = i\big[&\eta + \tau S(\phi,t) - \left(w^{e,i}\right)^2(\phi,\eta,t)\\ &+ P^{e,i}(\phi,t)\big],\end{aligned} \tag{2.A.4}$$

where $w^{e,i}(\phi,\eta,t) \equiv x^{e,i}(\phi,\eta,t) + iy^{e,i}(\phi,\eta,t)$. If $\eta$ are distributed according to a Lorentzian distribution Eq. (2.5), the integrals in (2.A.2) and (2.A.3) can then be evaluated closing the integral contour in the complex $\eta$-plane, and using the Cauchy residue theorem. Then the firing rate and mean membrane potential depend only on the value of $w^{e,i}$ at the pole of $g(\eta)$ in the lower half $\eta$-plane: $\pi\tau R^{e,i}(\phi,t) + iV^{e,i}(\phi,t) = w^{e,i}(\phi,\bar{\eta}-i\Delta,t)$, and, as a result, (2.A.4) must be evaluated only at $\eta = \bar{\eta} - i\Delta$ to obtain the neural field equations [Eq. (2.6)]*

These equations can be nondimensionalized by rescaling variables and time as (note the difference between $v_j^{e,i}$, the membrane potential of a single neuron $j$, and the mean membrane potential $v^{e,i}$):

$$R^{e,i} = \frac{\sqrt{\Delta}}{\tau}r^{e,i}\ ,\ V^{e,i} = \sqrt{\Delta}\,v^{e,i}\ ,\ t = \frac{\tau}{\sqrt{\Delta}}\tilde{t}, \tag{2.A.5}$$

* The derivation of the QIF-NFM Eq. (2.6) can be readily extended to account for population of excitatory and inhibitory neurons of different sizes, i.e. $N^e \neq N^i$. This can be always achieved by rescaling the relative contributions of the excitatory and inhibitory mean fields as $S(\phi) = p^e S^e(\phi) + p^i S^i(\phi)$, where $p^e = 2N^e/\left(N^e+N^i\right)$ and $p^i = 2N^i/\left(N^e+N^i\right)$. In the case of the effective model Eq. (2.7), this implies that Fourier coefficients in Eq. (2.8) need to be changed as $J_K = p^e J_K^e - p^i J_K^i$.

and parameters as:

$$J_K^{e,i} = \sqrt{\Delta}\, j_K^{e,i},\ \bar{\eta} = \Delta\tilde{\eta},\ P^{e,i}(\phi,t) = \Delta\tilde{P}^{e,i}(\phi,\tilde{t}). \tag{2.A.6}$$

The resulting dimensionless NFM is then

$$\begin{aligned} \dot{r}^{e,i} &= \frac{1}{\pi} + 2v^{e,i}r^{e,i}, && \text{(2.A.7a)} \\ \dot{v}^{e,i} &= \left(v^{e,i}\right)^2 + \tilde{\eta} - \pi^2\left(r^{e,i}\right)^2 + s(\phi,\tilde{t}) && \text{(2.A.7b)} \\ &\quad + \tilde{P}^{e,i}(\phi,\tilde{t}), \end{aligned}$$

where the overdot represents derivation with respect the nondimensional time $\tilde{t}$ and the mean field is

$$\begin{aligned} s(\phi,\tilde{t}) =& \frac{1}{\pi}\int_{-\pi}^{\pi}\left[\frac{j_0^e}{2} + \sum_{K=1}^{\infty} j_K^e \cos(K(\phi'-\phi))\right] r^e(\phi',\tilde{t})d\phi' \\ &- \frac{1}{\pi}\int_{-\pi}^{\pi}\left[\frac{j_0^i}{2} + \sum_{K=1}^{\infty} j_K^i \cos(K(\phi'-\phi))\right] r^i(\phi',\tilde{t})d\phi'. \end{aligned} \tag{2.A.8}$$

## 2.A.1 Effective NFM

Considering $\tilde{P}^{e,i}(\phi,\tilde{t}) = \tilde{P}(\phi,\tilde{t})$ in Eqs. (2.A.7), the system

$$\begin{aligned} \dot{r} &= \frac{1}{\pi} + 2vr, && \text{(2.A.9a)} \\ \dot{v} &= v^2 + \tilde{\eta} - \pi^2 r^2 + s(\phi,\tilde{t}) + \tilde{P}(\phi,\tilde{t}), && \text{(2.A.9b)} \end{aligned}$$

with the mean field

$$s(\phi,t) = \frac{1}{\pi}\int_{-\pi}^{\pi}\left[\frac{j_0}{2} + \sum_{K=1}^{\infty} j_K \cos(K(\phi'-\phi))\right] r(\phi',t)d\phi'. \tag{2.A.10}$$

and

$$j_K = j_K^e - j_K^i,$$

has identical symmetric solutions as the original Eqs.(2.A.7), i.e.

$$r^e(t) = r^i(t) = r(t), \quad v^e(t) = v^i(t) = v(t).$$

## 2.B Linear stability analysis of the SHS

### 2.B.1 Linear stability of the effective QIF-NFM Eq. (2.7)

The homogeneous steady state is given by the solution of Eq. (2.9) when $R_*(\phi) = R_*$. This is equivalent to $S_*(\phi) = S_* = J_0 R_*$ that in dimensionless form is

$$\pi^2 r_*^4 - j_0 r_*^3 - \tilde{\eta} r_*^2 - \frac{1}{4\pi^2} = 0. \tag{2.B.1}$$

This equation is greatly simplified assuming $j_0 = 0$ and gives

$$r_* = \frac{1}{\pi\sqrt{2}} \sqrt{\tilde{\eta} + \sqrt{\tilde{\eta}^2 + 1}}. \tag{2.B.2}$$

The stability of homogeneous steady-state solutions can be analyzed studying the evolution of the small (even) perturbations ($\epsilon \ll 1$) of the SHS

$$r(\phi, t) = r_* + \epsilon \sum_{K=0}^{\infty} a_K(t) \cos(K\phi), \tag{2.B.3a}$$

$$v(\phi, t) = v_* + \epsilon \sum_{K=0}^{\infty} b_K(t) \cos(K\phi). \tag{2.B.3b}$$

Substituting (2.B.3) into the mean field (2.A.10), we obtain a perturbed mean field around $s_*(\phi)$

$$s(\phi, t) = s_*(\phi) + \epsilon \sum_{K=0}^{\infty} j_K a_K(t) \cos(K\phi). \tag{2.B.4}$$

Linearizing Eqs. (2.A.9) around the fixed point $(r_*, v_*)$, gives

$$\sum_{K=0}^{\infty} \mu_K a_K \cos(K\phi) = 2 \sum_{K=0}^{\infty} [r_*(\phi) b_K + v_*(\phi) a_K] \cos(K\phi), \tag{2.B.5}$$

$$\sum_{K=0}^{\infty} \mu_K b_K \cos(K\phi) = \sum_{K=0}^{\infty} \left[2 v_*(\phi) b_K + (j_K - 2\pi^2 r_*(\phi)) a_K\right] \cos(K\phi),$$

where we have used the ansatz $a_K(t) = a_K e^{\mu_K t}$ and $b_K(t) = b_K e^{\mu_K t}$, where $\mu_K$ represents the dimensionless eigenvalue of the $K$th mode. For

SHS states, $(r_*(\phi), v_*(\phi)) = (r_*, v_*)$, the modes in Eqs. (2.B.6) decouple and, for a given mode $K$, we find the linear system

$$\mu_K \begin{pmatrix} a_K \\ b_K \end{pmatrix} = L_* \begin{pmatrix} a_K \\ b_K \end{pmatrix}, \tag{2.B.6}$$

with:

$$L_* = \begin{pmatrix} 2v_* & 2r_* \\ j_K - 2\pi^2 r_* & 2v_* \end{pmatrix}. \tag{2.B.7}$$

Equation (2.B.6) has a general solution:

$$\begin{pmatrix} a_K(\tilde{t}) \\ b_K(\tilde{t}) \end{pmatrix} = A_+ \mathbf{u}_+ e^{\mu_{K+}\tilde{t}} + A_- \mathbf{u}_- e^{\mu_{K-}\tilde{t}}, \tag{2.B.8}$$

where $A_\pm$ are arbitrary constants. The eigenvalues $\mu_{K\pm}$ are given by

$$\mu_{K\pm} = -\frac{1}{\pi r_*} \pm 2\pi r_* \sqrt{\frac{j_K}{2\pi^2 r_*} - 1}, \tag{2.B.9}$$

with eigenvectors

$$\mathbf{u}_\pm = \begin{pmatrix} \pm 1 \\ \sqrt{\frac{j_K}{2r_*} - \pi^2} \end{pmatrix}. \tag{2.B.10}$$

In terms of the dimensional variables and parameters (2.A.5) and (2.A.6), the eigenvalues (2.B.9) are $\lambda_k t = \mu_k \tilde{t}$, and thus $\lambda_k = \sqrt{\Delta}\mu_k/\tau$, which gives the eigenvalues Eq. (2.10) in the main text.

## 2.B.2 Linear stability of the full QIF-NFM

For the full QIF-NFM Eq. (2.6), the perturbation around the SHS state has the form

$$\begin{aligned} r^{e,i}(\phi, t) &= r_* + \epsilon \sum_{K=0}^{\infty} a_K^{e,i}(t) \cos(K\phi), \\ v^{e,i}(\phi, t) &= v_* + \epsilon \sum_{K=0}^{\infty} b_K^{e,i}(t) \cos(K\phi). \end{aligned}$$

In this case, the linear stability of the SHS state with respect to perturbations of the $K$-spatial mode is determined by the characteristic equation

$$\lambda_K \begin{pmatrix} a_K^e \\ b_K^e \\ a_K^i \\ b_K^i \end{pmatrix} = \begin{pmatrix} 2v_* & 2r_* & 0 & 0 \\ j_K^e - 2\pi^2 r_* & 2v_* & -j_K^i & 0 \\ 0 & 0 & 2v_* & 2r_* \\ j_K^e & 0 & -j_K^i - 2\pi^2 r_* & 2v_* \end{pmatrix} \begin{pmatrix} a_K^e \\ b_K^e \\ a_K^i \\ b_K^i \end{pmatrix} \tag{2.B.11}$$

For each $K$ mode, the linearized system has a general solution

$$\begin{pmatrix} a^e_K(\tilde{t}) \\ b^e_K(\tilde{t}) \\ a^i_K(\tilde{t}) \\ b^i_K(\tilde{t}) \end{pmatrix} = A_+ \quad \mathbf{u}_{K+} e^{\mu_{K+}\tilde{t}} + A_- \mathbf{u}_{K-} e^{\mu_{K-}\tilde{t}} + \\ B_+ \quad \mathbf{u}_{K\perp} e^{\mu_\perp \tilde{t}} + B_- \bar{\mathbf{u}}_{K\perp} e^{\bar{\mu}_\perp \tilde{t}}, \tag{2.B.12}$$

where $A_\pm$ and $B_\pm$ are arbitrary constants. The eigenvectors

$$\mathbf{u}_{K\pm} = \begin{pmatrix} \pm 1 \\ \sqrt{\frac{j^e_K - j^i_K}{2r_*} - \pi^2} \\ \pm 1 \\ \sqrt{\frac{j^e_K - j^i_K}{2r_*} - \pi^2} \end{pmatrix}. \tag{2.B.13}$$

have eigenvalues

$$\mu_{K\pm} = -\frac{1}{\pi r_*} \pm 2\pi r_* \sqrt{\frac{j^e_K - j^i_K}{2\pi^2 r_*} - 1}. \tag{2.B.14}$$

These eigenvalues coincide with those of the reduced system (2.B.9), and are associated with the standing waves shown in Fig. 2.2. Additionally, the eigenvector

$$\mathbf{u}_{K\perp} = \begin{pmatrix} i j^i_K \\ \pi j^i_K \\ i j^e_K \\ \pi j^e_K \end{pmatrix}, \tag{2.B.15}$$

and its complex conjugate $\bar{\mathbf{u}}_{K\perp}$, with the associated eigenvalue

$$\mu_\perp = -\frac{1}{\pi r_*} + i 2\pi r_*, \tag{2.B.16}$$

and its complex conjugate $\bar{\mu}_\perp$, correspond to modes of oscillation of the uncoupled system. Indeed, note that the eigenvalues (2.B.16) are independent of the connectivity, and correspond to oscillatory modes which are already present in a single population of uncoupled neurons —note that eigenvalues (2.B.14) reduce to (2.B.16) for all the modes with $j_K = j^e_K - j^e_K = 0$.

## 2.C Small-amplitude equation near the Spatially Homogeneous State

### 2.C.1 Critical eigenvectors

Right at the bifurcation, the only undamped mode is the critical one given by $\mathbf{u}_+$ in (2.B.10), that reduces to the critical eigenmode:

$$\mathbf{u}_c = \begin{pmatrix} r_* \\ -v_* \end{pmatrix}. \tag{2.C.1}$$

At criticality, the critical eigenmode of $L_*$ satisfies

$$L_{*c}\mathbf{u}_c = 0,$$

where $L_{*c}$ corresponds to the operator (2.B.7) evaluated at $j_K = j_{Kc}$. The left critical eigenvector of the operator $L_{*c}$ is then defined as

$$\mathbf{u}_c^\dagger L_{*c} = 0,$$

which gives

$$\mathbf{u}_c^\dagger = \pi \begin{pmatrix} -v_* \\ r_* \end{pmatrix}^T, \tag{2.C.2}$$

where the constant has been taken to normalize the eigenvectors, so that they satisfy $\mathbf{u}_c^\dagger \mathbf{u}_c = 1$.

### 2.C.2 Amplitude equation

Except for initial transients, the amplitude of the bifurcating solution at criticality is expected to contain only the component $\mathbf{u}_{+c}$. In the following we derive a small-amplitude equation for the bump solutions using multiple-scale analysis, (Kuramoto, 1984, see e.g.). First, let the solution of Eqs. (2.A.9) be written as the perturbation expansion

$$\begin{pmatrix} r(\phi,\tilde{t}) \\ v(\phi,\tilde{t}) \end{pmatrix} = \begin{pmatrix} r_* \\ v_* \end{pmatrix} + \epsilon \begin{pmatrix} r_\epsilon(\phi,\tilde{t},\tilde{T}) \\ v_\epsilon(\phi,\tilde{t},\tilde{T}) \end{pmatrix} + \epsilon^2 \begin{pmatrix} r_{\epsilon\epsilon}(\phi,\tilde{t},\tilde{T}) \\ v_{\epsilon\epsilon}(\phi,\tilde{t},\tilde{T}) \end{pmatrix} + \dots \tag{2.C.3}$$

where $(r_*, v_*)$ is the state SHS given by the solutions of (2.B.1), and $\epsilon \ll 0$ is a small parameter, which measures the distance from the Turing bifurcation. In addition, we define a long time scale, $\tilde{T} = \epsilon^2 \tilde{t}$, that is considered to be

independent of $\tilde{t}$. Accordingly, the differential operator in Eqs. (2.A.9) may be replaced by:

$$\partial_{\tilde{t}} \to \partial_{\tilde{t}} + \epsilon^2 \partial_{\tilde{T}}.$$

Since the asymptotic expansion is going to be performed in the vicinity of a stationary bifurcation, we set $\partial_{\tilde{t}} = 0$ so that the only temporal variations occur with the slow time scale $\tilde{T}$.

Additionally, in our analysis we use the parameter $j_1$ as the bifurcation parameter, and we write it as

$$j_1 = j_1^T + \epsilon^2 \delta j_1, \tag{2.C.4}$$

where $j_1^T$ is the critical value of $j_1$ at which the Turing bifurcation occurs, given by Eq. (2.11), with $K = 1$. Accordingly, the (nondimensionalized) connectivity footprint (2.1) is

$$j(\phi) = j_c(\phi) + 2\epsilon^2 \delta j_1 \cos\phi, \tag{2.C.5}$$

with

$$j_c(\phi) = j_0 + 2j_1^T \cos\phi + 2\sum_{K=2}^{\infty} j_K \cos(K\phi), \tag{2.C.6}$$

where $j_K < j_{Kc}$ for $K \neq 1$. To simplify the notation, we hereafter omit to explicitly write the dependence of $r_{\epsilon,\epsilon\epsilon,\ldots}$ and $v_{\epsilon,\epsilon\epsilon,\ldots}$ on the variables $\tilde{t}, T$ and $\phi$. Substituting (2.C.3) and (2.C.5) into the mean field (2.A.10):

$$\begin{aligned}
s(\phi) &= \frac{1}{2\pi}\int_{-\pi}^{\pi} (r_* + \epsilon r_\epsilon + \epsilon^2 r_{\epsilon\epsilon} + \ldots) j_c(\phi - \phi') d\phi' \\
&\quad + \epsilon^2 \frac{1}{\pi}\int_{-\pi}^{\pi} (r_* + \epsilon r_\epsilon + \epsilon^2 r_{\epsilon\epsilon} + \ldots)\, \delta j_1 \cos(\phi - \phi') d\phi' \\
&\equiv \langle r_* + \epsilon r_\epsilon + \epsilon^2 r_{\epsilon\epsilon} + \ldots \rangle_c \\
&\quad + 2\epsilon^2 \langle r_* + \epsilon r_\epsilon + \epsilon^2 r_{\epsilon\epsilon} + \ldots \rangle \qquad (2.C.7) \\
&= r_* j_0 + \epsilon \langle r_\epsilon \rangle_c + \epsilon^2 \langle r_{\epsilon\epsilon} \rangle_c + \epsilon^3 (\langle r_{\epsilon\epsilon\epsilon} \rangle_c + 2\langle r_\epsilon \rangle) + \ldots \qquad (2.C.8)
\end{aligned}$$

Plugging expansions (2.C.3) and (2.C.5) into the NFM Eqs. (2.A.9), we obtain

$$\begin{aligned}
\epsilon^2 \partial_{\tilde{T}} (\epsilon r_\epsilon + \epsilon^2 r_{\epsilon\epsilon} + \ldots) &= \epsilon(2v_* r_\epsilon + 2r_* v_\epsilon) \\
&\quad + \epsilon^2 (2v_* r_{\epsilon\epsilon} + 2r_\epsilon v_\epsilon + 2r_* v_{\epsilon\epsilon}) \\
&\quad + \epsilon^3 (2v_\epsilon r_{\epsilon\epsilon} + 2r_\epsilon v_{\epsilon\epsilon}) + \ldots \\
\epsilon^2 \partial_{\tilde{T}} (\epsilon v_\epsilon + \epsilon^2 v_{\epsilon\epsilon} + \ldots) &= \epsilon(2v_* v_\epsilon - 2\pi^2 r_* r_\epsilon + \langle r_\epsilon \rangle_c) \\
&\quad + \epsilon^2 (v_\epsilon^2 - \pi^2 r_\epsilon^2 + 2v_* v_{\epsilon\epsilon} - 2\pi^2 r_* r_{\epsilon\epsilon} + \langle r_{\epsilon\epsilon} \rangle_c) \\
&\quad + \epsilon^3 (2v_\epsilon v_{\epsilon\epsilon} - 2\pi^2 r_\epsilon r_{\epsilon\epsilon} + \langle r_{\epsilon\epsilon\epsilon} \rangle_c + 2\langle r_\epsilon \rangle) + \ldots
\end{aligned}$$

These equations can be written in a more compact form as

$$-\left(L_c+\epsilon^2 L_{\epsilon\epsilon}\right)\left[\epsilon\begin{pmatrix} r_\epsilon \\ v_\epsilon \end{pmatrix}+\epsilon^2\begin{pmatrix} r_{\epsilon\epsilon} \\ v_{\epsilon\epsilon} \end{pmatrix}+...\right]=\epsilon^2 N_{\epsilon\epsilon}+\epsilon^3 N_{\epsilon\epsilon\epsilon}+\dots, \quad (2.C.9)$$

defining the linear and nonlinear operators

$$\begin{aligned} L_c &= \begin{pmatrix} 2v_* & 2r_* \\ \langle\cdot\rangle_c - 2\pi^2 r_* & 2v_* \end{pmatrix}, \\ L_{\epsilon\epsilon} &= \begin{pmatrix} -\partial_{\tilde{T}} & 0 \\ 2\langle\cdot\rangle & -\partial_{\tilde{T}} \end{pmatrix}, \\ N_{\epsilon\epsilon} &= \begin{pmatrix} 2r_\epsilon v_\epsilon \\ v_\epsilon^2 - \pi^2 r_\epsilon^2 \end{pmatrix}, \\ N_{\epsilon\epsilon\epsilon} &= \begin{pmatrix} 2r_\epsilon v_{\epsilon\epsilon} + 2r_{\epsilon\epsilon} v_\epsilon \\ 2v_\epsilon v_{\epsilon\epsilon} - 2\pi^2 r_\epsilon r_{\epsilon\epsilon} \end{pmatrix}, \end{aligned}$$

Next we collect terms by order in $\epsilon$. At first order we recover the linear problem (2.B.6) at the Turing bifurcation:

$$\begin{pmatrix} 2v_* & 2r_* \\ j_1^T - 2\pi^2 r_* & 2v_* \end{pmatrix}\begin{pmatrix} r_\epsilon \\ v_\epsilon \end{pmatrix}=\begin{pmatrix} 0 \\ 0 \end{pmatrix}.$$

Recalling that $j_1^T$ is given by Eq. (2.C.4), we find the neutral solution:

$$\begin{pmatrix} r_\epsilon \\ v_\epsilon \end{pmatrix} = A\,\mathbf{u}_c \cos\phi, \quad (2.C.10)$$

where $A$ is the small amplitude with slow time dependence that we aim to determine and $\mathbf{u}_c$ is the critical eigenmode given by Eq. (2.C.1). Substituting the solution (2.C.10) into the nonlinear forcing terms $N_{\epsilon\epsilon}$ we find

$$N_{\epsilon\epsilon} = \frac{A^2}{2}\begin{pmatrix} \pi^{-1} \\ v_*^2 - \pi^2 r_*^2 \end{pmatrix}[1+\cos(2\phi)],$$

what implies that, at second order, the solution must necessarily contain homogeneous and second spatial components

$$\begin{pmatrix} r_{\epsilon\epsilon} \\ v_{\epsilon\epsilon} \end{pmatrix} = \begin{pmatrix} r_{\epsilon\epsilon 0} \\ v_{\epsilon\epsilon 0} \end{pmatrix} + \begin{pmatrix} r_{\epsilon\epsilon 2} \\ v_{\epsilon\epsilon 2} \end{pmatrix}\cos(2\phi).$$

Equating the homogeneous, second order terms of equation (2.C.9) we find

$$-\begin{pmatrix} 2v_* & 2r_* \\ j_0 - 2\pi^2 r_* & 2v_* \end{pmatrix}\begin{pmatrix} r_{\epsilon\epsilon 0} \\ v_{\epsilon\epsilon 0} \end{pmatrix}=\frac{A^2}{2}\begin{pmatrix} \pi^{-1} \\ v_*^2 - \pi^2 r_*^2 \end{pmatrix},$$

and left-multiplying this equation by $L_c^{-1}$, and using Eq. (2.12) we find

$$\begin{pmatrix} r_{\epsilon\epsilon 0} \\ v_{\epsilon\epsilon 0} \end{pmatrix} = \frac{A^2}{4r_*(j_1^T - j_0)} \begin{pmatrix} 2v_* & -2r_* \\ 2\pi^2 r_* - j_0 & 2v_* \end{pmatrix} \begin{pmatrix} \pi^{-1} \\ v_*^2 - \pi^2 r_*^2 \end{pmatrix},$$

which gives the coefficients

$$r_{\epsilon\epsilon 0} = \frac{3v_*^2 - \pi^2 r_*^2}{2(j_1^T - j_0)} A^2, \tag{2.C.11}$$

$$v_{\epsilon\epsilon 0} = \frac{2\pi v_*^4 - v_* j_0 - 3\pi/2}{2(j_1^T - j_0)} A^2. \tag{2.C.12}$$

Proceeding similarly, we find the coefficients corresponding to the second spatial Fourier modes:

$$r_{\epsilon\epsilon 2} = \frac{3v_*^2 - \pi^2 r_*^2}{2(j_1^T - j_2)} A^2, \tag{2.C.13}$$

$$v_{\epsilon\epsilon 2} = \frac{2\pi v_*^4 - v_* j_2 - 3\pi/2}{2(j_1^T - j_2)} A^2. \tag{2.C.14}$$

Collecting the third-order terms of equation (2.C.9), we obtain the identity

$$-L_c \begin{pmatrix} r_{\epsilon\epsilon\epsilon} \\ v_{\epsilon\epsilon\epsilon} \end{pmatrix} - L_{\epsilon\epsilon} \begin{pmatrix} r_\epsilon \\ v_\epsilon \end{pmatrix} = N_{\epsilon\epsilon\epsilon}. \tag{2.C.15}$$

To obtain the desired amplitude equation, we shall left-multiply Eq. (2.C.15) by the left null-eigenvector (2.C.2) and project it into the first spatial Fourier mode. The first term on the right-hand side of Eq. (2.C.15) vanishes since $\mathbf{u}_c^\dagger L_c = 0$. The second term is

$$L_{\epsilon\epsilon} \begin{pmatrix} r_\epsilon \\ v_\epsilon \end{pmatrix} = \begin{pmatrix} -r_* \, \partial_{\tilde{T}} A \\ v_* \, \partial_{\tilde{T}} A + \delta j_1 \, r_* \, A \end{pmatrix} \cos\phi.$$

Finally, the nonlinear forcing term at the left-hand side of Eq. (2.C.15) is

$$\begin{aligned} N_{\epsilon\epsilon\epsilon} = & -A\cos\phi \begin{pmatrix} v_*\alpha - r_*\beta \\ \pi^2 r_*\alpha + v_*\beta \end{pmatrix} \\ & -A\cos(3\phi) \begin{pmatrix} v_* r_{\epsilon\epsilon 2} - r_* v_{\epsilon\epsilon 2} \\ \pi^2 r_* r_{\epsilon\epsilon 2} + v_* v_{\epsilon\epsilon 2} \end{pmatrix}, \end{aligned}$$

where $\alpha = (2r_{\epsilon\epsilon 0} + r_{\epsilon\epsilon 2})$ and $\beta = (2v_{\epsilon\epsilon 0} + v_{\epsilon\epsilon 2})$. Thus, the solvability condition gives

$$\mathbf{u}_c^\dagger \begin{pmatrix} r_* \, \partial_{\tilde{T}} A \\ -v_* \, \partial_{\tilde{T}} A - \delta j_1 \, r_* \, A \end{pmatrix} = -A \mathbf{u}_c^\dagger \begin{pmatrix} v_*\alpha - r_*\beta \\ \pi^2 r_*\alpha + v_*\beta \end{pmatrix}. \tag{2.C.16}$$

Substituting the coefficients (2.C.11), (2.C.12), (2.C.13), and (2.C.14) into Eq. (2.C.16) gives the desired amplitude equation

$$\partial_{\tilde{T}} A = \pi r_*^2 \, \delta j_1 A + \tilde{a} A^3, \tag{2.C.17}$$

where the parameter $\tilde{a}$ is

$$\begin{aligned} \tilde{a} =& \pi \left( 5v_*^4 + \pi^4 r_*^4 - \frac{5}{2} \right) \left( \frac{1}{j_1^T - j_0} + \frac{1/2}{j_1^T - j_2} \right) \\ & - v_* \left( \frac{j_0}{j_1^T - j_0} + \frac{j_2/2}{j_1^T - j_2} \right). \end{aligned} \tag{2.C.18}$$

Equating Eq. (2.C.18) to zero, gives the critical boundary $j_2^c$ separating subcritical and supercritical Turing bifurcations:

$$j_2^c = \frac{3j_1^T - j_0}{2} + \frac{6(j_1^T - j_0)^2 \pi^2 r_*^3}{5 + 4\pi^2 r_*^3 (3j_0 - j_1^T - 10\pi^2 r_* + 4\pi^6 r_*^5)}. \tag{2.C.19}$$

In dimensional form, Eqs. (2.C.17), (2.C.18), and (2.C.19) are respectively:

$$\tau \partial_T A = \pi \frac{\tau^2 R_*^2}{\Delta} \, \delta J_1 A + a A^3, \tag{2.C.20}$$

$$\begin{aligned} a = & \left[ \pi \left( \frac{5\Delta^3}{16\pi^4 \tau^4 R_*^4} + \frac{\pi^4 \tau^4 R_*^4}{\Delta} - \frac{5\Delta}{2} \right) \left( \frac{1}{J_1^T - J_0} + \frac{1/2}{J_1^T - J_2} \right) \right. \\ & \left. + \frac{\Delta}{2\pi\tau R_*} \left( \frac{J_0}{J_1^T - J_0} + \frac{J_2/2}{J_1^T - J_2} \right) \right], \end{aligned} \tag{2.C.21}$$

and

$$J_2^c = \frac{3J_1^T - J_0}{2} + \frac{6(J_1^T - J_0)^2 \pi^2 \tau^3 R_*^3}{5\Delta^2 + 4\pi^2 \tau^3 R_*^3 \left( 3J_0 - J_1^T - 10\pi^2 \tau R_* + \frac{4\pi^6 \tau^5 R_*^5}{\Delta^2} \right)}. \tag{2.C.22}$$

# 2.D Numerical simulations

## 2.D.1 Numerical simulation of the QIF model

In numerical simulations we used the Euler scheme with time step $dt = 10^{-3}$. Additionally, we considered the peak and reset values $v_p = -v_r = 100$. The algorithm used to simulate the QIF neuron (2.2) is shown in Fig. 2.D.1.

**Require:** Variables: $v_j$, $I_j$, $t_j^r$ (exit time from refractory period), $t$ (time).
Constants: $\tau, dt, v_p$.
**Ensure:** $\dot{v}_j = v_j^2 + I_j$ and $t_j^l$ and $t_j^r$.

**bool** spike$_j$ $\leftarrow$ **False**
**if** $t \geq t_j^r$ **then** ▷ Check whether the neuron is in the refractory period.
    $v_j \leftarrow v_j + \frac{dt}{\tau}\left(v_j^2 + I_j\right)$ ▷ Euler integration.
    **if** $v_j \geq v_p$ **then** ▷ Check if the voltage has crossed the threshold.
        spike$_j$ $\leftarrow$ **True** ▷ The neuron has spiked at time $t_j^l$.
        $t_j^r \leftarrow t + 2 \cdot \frac{\tau}{v_j}$ ▷ Set the end of the refractory period.
        $t_j^l \leftarrow t + \frac{\tau}{v_j}$ ▷ Spike time is set after $\frac{\tau}{v_j}$.
        $v_j \leftarrow -v_j$ ▷ Reset the voltage.
    **end if**
**end if**

**Figure 2.D.1:** Algorithm used for the Euler integration of the QIF neuron Eq. (2.2).

## 2.D.2 Numerical simulation of the ring network

To numerically implement the ring network of QIF neurons we divided the ring into $m = 100$ intervals located at $\phi_l = 2\pi l/m - \pi$, $l = 1, \ldots, m$. At each interval $\phi_l$, we considered $n = 2.5 \cdot 10^3$ excitatory and $n = 2.5 \cdot 10^3$ inhibitory neurons (i.e. the ring consisted of a total of $2N = 2m\,n = 5 \times 10^5$ QIF neurons).

The neurons in each location $\phi_l$ receive Lorentzian-distributed currents, which have been generated using the formula

$$\eta_i = \bar{\eta} + \Delta \tan\left[\frac{\pi}{2}\frac{2i - n - 1}{n + 1}\right],\ i = 1, \ldots, n. \tag{2.D.1}$$

On the other hand, perturbations (applied at time $t_0$) are modeled using the function

$$P^{e,i}(\phi, t) = A\left(e^{(t-t_0)/\tau_r} - 1\right) \cdot \cos\left(K \cdot \phi\right), \tag{2.D.2}$$

where $A$ is the amplitude, $K$ is the wave number, and $\tau_r$ is the rising time constant of the perturbation. In Figs. 2.2, 2.3 and 2.5 we used $t_0 = 0.05$ s,

$A = 0.3$, and $\tau_r = 4 \times 10^{-3}$ s. The perturbations had a duration of $\Delta t = 0.01$ s.

Finally, the instantaneous firing rates in Fig. 2.2 are obtained binning time and counting the spikes of neurons in each interval $\phi_l$ within a sliding time window of size $\delta t = 0.01$s.

# Discussion

In this thesis we have addressed issues concerning the effect of synchronous activity in the formation of spatiotemporal patterns in networks of spiking neurons.

First, we have shown that traditional neural field models are indeed capable of qualitatively reproducing many of the spatiotemporal patterns shown by their equivalent spiking neural networks. But we also have shown that in order to achieve this, they often need to consider additional heuristic elements, such as explicit fixed time delays, not present in the original networks of spiking neurons. Such limitations reveal the failure of traditional NFMs to predict the onset of synchrony-induced dynamics. Particularly, we have seen that synchronization appears to be decisive in shaping the dynamics of networks of recurrently coupled inhibitory neurons (I-I) and of cross-coupled excitatory-inhibitory (E-I) neuronal networks, and by extension, of distributed networks with spatially dependent excitatory-inhibitory interactions.

These observations have led us to the discovery of what we have called the *modes of oscillations* of a neuronal network, present in spatially distributed networks of heterogeneous spiking neurons. These modes reflect the transient episodes of spike synchronization among the neurons and therefore cannot be captured by traditional NFMs.

In order to investigate these oscillations we have derived a novel NFM for QIF neurons following the methodology of Montbrió et al. (2015). The low-dimensional description presented in this work (2.7) is closely related to that of Laing (2014) where he derived a neural field description of a

network of pulse-coupled theta neurons by invoking the Ott-Antonsen theory (Luke et al., 2013; So et al., 2014). However, some important differences exist between both approaches. In Laing's work, synaptic interactions were modeled as pulses of finite width, in contrast to the instantaneous interactions used in (Montbrió et al., 2015) and in the present work. The use of finite pulses greatly complicates the mathematical analysis and the numerical simulations. Additionally, in Laing's work and in other recently published works on pulse-coupled oscillators (Pazó and Montbrió, 2014; Gallego et al., 2017), the resulting low-dimensional description appears in terms of the complex Kuramoto order parameter, which gives a measure of the synchronicity of the population but is difficult to relate with physiologically relevant magnitudes such as the firing rate or the mean membrane potential. In contrast, the mean-field description adopted in section 1.3 and in chapter 2 greatly simplifies the analysis, allowing us to analytically investigate the linear and nonlinear stability of the spatially homogeneous states of the QIF-NFM.

This analysis revealed two important features regarding the *modes of oscillation*:

i) The frequency of each oscillation mode only depends of the corresponding Fourier coefficient of thepattern of synaptic connectivity.

ii) The decay rate is the same for all modes and reflects the diffusion of the phases of neurons due to a desynchronization mechanism which depends on the degree of quenched heterogeneity.

In section 1.2 we have also numerically shown that similar oscillatory behaviors occur in networks of identical QIF neurons subject to noise, as well as for different kinds of spiking neuron models (LIF and EIF).

Finally, we have investigated the existence and the stability of bump states, which bifurcate from the spatially homogeneous states via Turing bifurcations. The spectrum of such bump states has a continuous part off the real axis, indicating that similar synchronization-induced oscillatory modes also operate in neural bump states.

In summary, our results indicate that in general, a correct macroscopic description of spiking networks requires keeping track of the mean subthreshold voltage along with the mean firing rate, and that synchronous activity is capable of generating macroscopically relevant patterns which could have a potential impact in cognitive processing.

## Additional considerations and comments

It is worth commenting on some of the counterpart results of this thesis which may shed some light in future works that consider the use of the QIF-NFM or the QIF-FREs.

**Network topology.** First, the formalism presented in our work allows for different interpretations regarding the spatial distribution of neurons. In chapter 2 we considered a continuum topology in which neurons are spatially distributed according to an angular variable; an architecture typically used to model neurons that present tuning curves in response to sensory stimulus. However, an alternative interpretation of the ring topology is that in which neurons are arranged in discrete localized populations, for example representing cortical macrocolumns. The approach followed in section 1.1 is closer to this latter interpretation. In fact, we saw that the symmetry breaking mechanism of section 1.1.1.3 was identical for both the two-population network and the ring model.

Hence, despite in this thesis we have only considered a simple network architecture, i.e. the ring topology, the model can be easily extended to account for any network architecture whose graph is described by means of a Laplacian matrix. The theoretical framework established by the works of Pecora and Carroll (1998); Pecora (1998) allows one to perform a linear stability analysis of the stable homogeneous states for such network topologies, obtaining a similar result for the spectrum of eigenvalues. A similar approach aimed to model whole brain activity was followed by Atasoy et al. (2016) where they considered each node of the network as populations of neurons located somewhere in the cortex. In that work they studied the relationship between the structural connectivity and the resulting oscillatory dynamics. Therefore, a similar research may be conducted using the QIF-NFM, facilitating the mathematical analysis and allowing for a deeper study of the structural/functional relationship of the brain activity. Additionally, it would establish a direct link, not present in H-NFM, between the single neuron parameters and the macroscopic activity of the population.

**Symmetry breaking in the effective two-population model** (1.20)**.** It is well known that in a system of two identical cross-coupled neuronal populations, enough inhibitory coupling leads to a Pitchfork bifurcation. This model has been extensively studied as a functional description for two-choice decision making tasks (see. e.g. Martí et al., 2008; Roxin and

Ledberg, 2008). When using traditional firing rate models such as Eq.(1.20), linear stability analysis reveals that the stable state characterizing the initial (undecided) state is a stable node. Choice formation can be induced either by an increase in the external input that destabilizes the spontaneous state (Wang, 2002; Durstewitz and Wang, 2003; Lo and Wang, 2006), or via an escape mechanisms induced by finite-size noise.

However, in a network of spiking neurons the same spontaneous state is a stable focus—for a given choice of the parameters—, which can be captured by means of the QIF firing rate equations (1.47). Such a system may display interesting responses when is exposed to random inputs due to resonance effects.

## Open questions and future direction

Besides the already proposed research paths, interesting directions of further study are the analysis of the full QIF-NFM (2.6) considering different time scales for excitatory and inhibitory neurons ($\tau_e \neq \tau_i$ or/and $\bar{\eta}_e \neq \bar{\eta}_i$). As it was recently proved (Avitabile et al., 2017), such time scale separation produces a rich variety of robust spatio temporal patterns. It would be enlightening to see whether such dynamics are also present in our model and whether new dynamics linked to synchronization related mechanisms arise, such as the PING oscillations observed in section 1.2. Additional directions include the study of the model considering synaptic delays (Pazó and Montbrió, 2016) and synaptic kinetics (Devalle et al., 2017b; Ratas and Pyragas, 2016) which would automatically give rise to ING oscillations for the spatially homogeneous state, as seen in section 1.2, and could additionally lead to spatiotemporal phenomena not previously observed in traditional NFMs.

The results concerning the bump state may also open new doors towards interesting models of cognitive processing. Dynamical regimes combining both, oscillations of different frequencies and persistent states, have attracted the attention of many researchers due to their potential use as plausible computational mechanisms underlying a variety of cognitive tasks, for example feature categorization (Martí and Rinzel, 2013), decision making (Wilimzig et al., 2006; Rabinovich et al., 2008; Bicho et al., 2011), or working memory (Compte, 2000; Gutkin et al., 2001; Laing et al., 2002; Dipoppa and Gutkin, 2013b; Wimmer et al., 2014; Roxin and Compte, 2016). Specifically, computational studies in localized populations of spiking neurons

have explored the role of oscillations in shaping network dynamics—and hence in driving behavior—during working memory tasks or flexible switching between oscillatory signals (Gutkin et al., 2001; Dipoppa and Gutkin, 2013b,a; Schmidt et al., 2018). As such, the combined manifestation of oscillations and persistent bump states in spatially extended systems could establish a potential computational framework for obtaining mechanistic explanations of the already mentioned cognitive tasks. Moreover, our analysis have exposed a direct, and rather simple connection between the structure of the network and the range of frequencies that the network is capable of generating, establishing a potential encoding mechanism based on the relation between the network structure and its activity spectrum.

The model presented in this work is however built upon some constraints which are worth commenting and which may open questions for future investigation. First, the exact derivation of the H-NFM is only possible for QIF neurons, which as we have already mentioned represent the canonical model for Class I excitability. Therefore, the model may not be appropriate when dealing with networks of Class II excitability neurons. Additionally, when compared with other integrate-and-fire neuron models, experimental results suggest that the EIF model might be a better choice since it has been shown that the spike onset of actual neurons is better described by an exponential nonlinearity (Badel et al., 2008). Nonetheless, in this work we have seen that both models present similar qualitative dynamics at the population level. It would be necessary to check whether this holds for dynamical regimes in which a relevant quantity of neurons is far from threshold, i.e. when the EIF and the QIF models display significantly different dynamics.

Second, the validity of the full connectivity assumption should be assessed, for example, by qualitatively comparing the model with an equivalent network of spiking neurons with sparse connectivity. Such network configurations are often used as a way of introducing random fluctuations in the activity of the neurons, and to some extent, to introduce some degree of heterogeneity into the network. But most importantly, they usually respond to anatomical considerations of the actual shape of neuronal networks. As such, it would be enlightening to compare the full connectivity network considering a noisy environment, with the sparse connectivity paradigm, and for example, see to what extent synchronous activity is lost.

Finally, the model shows potential for studying more realistic networks without a substantial increase on its complexity by considering for example,

conductance based * spiking neurons (Ratas and Pyragas, 2016), synaptic adaptation, electrical coupling modeled as gap junctions (Laing, 2015), etc.

In summary, we believe that the model presented in this thesis will indeed serve to further understand the dynamics of large networks of spiking neurons, and will open the door to new theoretical advances on neural field models.

*A first approach to study the macroscopic dynamics of networks of QIF neurons with conductance-based synapses is presented in Appendix B.2.

# APPENDIX A

# Numerical simulations

This appendix offers a detailed description of the methodology used to numerically implement the various models used throughout the thesis. All simulations were implemented in `Python` with an extensive use of `numpy` and `scipy` libraries. The source code is available at https://github.com/JMED106/QIF-FR. By default, to numerically integrate ODEs—-QIF, LIF, EIF model neurons; and macroscopic firing rate equations: H-FREs and QIF-FREs—-we used Euler scheme with a time step $dt = 10^{-3}$. Results obtained from simulations, such as the firing rate, $r$, were afterwards appropriately rescaled to account for biologically meaningful quantities using a similar approach as in Eqs. (2.A.5) and (2.A.6). For example, we systematically used $\tau_m = 20$ ms or $\tau_m = 10$ ms, that once applied to the simulated firing rate quantities, $r$, gave us values of the population firing rate, $R = r/\tau_m$, in the range of 5-100 Hz (higher values for ING and PING oscillations).

## A.1 Simulations of spiking neural networks

When choosing a particular model of spiking neurons we were seeking mathematical simplicity and the decision was highly motivated by the work done during the development of the QIF-FREs (1.47). Therefore we started working with **current-based** quadratic integrate-and-fire (QIF) model neurons

rather than with their homologous—and more realistic—conductance-based representations. Nevertheless, in appendix B.2 we derive a set of QIF-FREs for a network of all-to-all QIF neurons with conductances. This is still a work in progress which could give rise to interesting results, and solves some of the problems presented by the current-based approach, such as the non-saturation of the firing rate.

Despite focusing our study on networks of QIF neurons, we also performed simulations of other types of spiking neuron models to show the generality of the observed phenomena. Specifically, in Figs. A.2, 1.6 and 1.11; and Figs. A.1 and 1.8 to 1.11; we used leaky integrate-and-fire (LIF) and exponential integrate-and-fire (EIF) model neurons, respectively. All three models, LIF, QIF and EIF can be written with the general equation [Eq. (1.21)] that we copy here for convenience

$$\tau_m \frac{dv}{dt} = f(v) + RI(t) \quad + \text{resetting rule involving } v_r, \text{ and } v_p, \quad \text{(A.1.1)}$$

where the function $f(v)$ for each model, is:

- LIF: $f(u) = -v + E$,
- QIF: $f(u) = v^2$, (after proper rescaling, see section 1.3.1)
- EIF: $f(u) = -v + E + \Delta_T \exp\left(\frac{v - v_{\text{rh}}}{\Delta_T}\right)$.

Here, $E$ is the reversal potential or rest potential, and $\Delta_T$ is the spike slope factor that measures the sharpness of the spike onset in the EIF model once the *threshold*[*] $v_{\text{th}}$ is reached (Fourcaud-Trocmé et al., 2003). All three models can be interpreted as limits of the Hodgkin and Huxley (1952) model (Gerstner et al., 2014). In particular, taking $\Delta_T \to 0$ transforms the EIF into the LIF (Fourcaud-Trocmé et al., 2003). In addition, the dynamics of the EIF near the threshold potential are equivalent to the QIF model, which corresponds to the canonical type-I neuron model (see section 1.3.1). The reset condition discussed in section 1.3.1 is done in a similar way in all three models, i.e. whenever the membrane potential, $v_i$, reaches a given peak

[*]Notice the difference between the actual *threshold* and the *numerical threshold*. In the first case, the value corresponds to the unstable fixed point which provides the spike mechanism in QIF and EIF models, whereas the second case is present in all three models and defines the numerical point at which the reset is done. Thus, for the LIF model, the threshold is purely numerical and is equivalent to the peak potential, $v_p$.

**Table A.1:** Microscopic parameters used in simulations of integrate-and-fire model neurons and some of the corresponding theoretically derived quantities, such as fixed points and refractory periods.

| | | **LIF** | **QIF** | **EIF** |
|---|---|---|---|---|
| **Parameter** | *Symbol* | (mV) | (a.u.) | (mV) |
| Peak potential | $v_p$ | $-45$ | 100 | 40 |
| Reset potential | $v_r$ | $-68$ | $-100$ | $-68$ |
| Reversal potential | $E$ | $-48$ | — | $-50$ |
| Spike slope factor | $\Delta_T$ | — | — | 3 |
| Rheobase potential | $v_{\text{rh}}$ | — | — | $-45$ |
| Absolute refr. period | $\Delta_{\text{abs}}$ | 0 ms | 0 | 5 ms |
| **Indirect quantity** | | | | |
| Threshold potential | $v_{\text{th}}$ | — | 0 | $\sim(-42)$ |
| Resting potential | $v_{\text{rest}}$ | $-48$ | 0 | $\sim(-49)$ |
| Relative refr. period | $\Delta_{\text{rel}}$ | 0 ms | 0.02 | 0 ms |

potential $v_p$, the neuron is reset to $v_r$. Notice however, that in the case of the LIF neuron the reset is done immediately after reaching a *numerical threshold*, $v_p = v_{\text{th}}$, whereas in the QIF and EIF models, the membrane potential must reach the peak potential above the *actual threshold*, $v_p > v_{\text{th}}$, in order to be reset.

As a consequence, the LIF model does not have a refractory period except from the time step of the simulation, which limits the maximum firing rate attainable by neurons. In simulations, adding an absolute refractory time on the order of 1 ms did not produced any significant differences on the observed dynamics. In contrast, the QIF model has a relative refractory period once the peak potential is crossed, as explained in Section 1.3.1. Finally, the EIF model neuron presents both relative and absolute refractory periods, $\Delta_{\text{abs}}$. The former, as in the QIF model, is due to the spiking generation mechanism, while the latter is introduced by hand in the simulations by holding the neuron at the reset potential for an additional refractory time $\Delta_{\text{abs}}$ after the neuron fires a spike.

### Parameters of single neurons

The parameters used to simulate spiking neurons are summarized in Table A.1. They were chosen such that the dynamics were similar in all systems, but their values are not far from those typically used in computational works dealing with spiking neural networks (see, e.g., Fourcaud-Trocmé et al., 2003; Richardson, 2007; Roxin et al., 2011). The case of the QIF model is different as explained in section 1.3.1. In order to do a proper comparison between the QIF-FREs (1.47) and its equivalent spiking neural network, is necessary to define the threshold at 0. However, to compare the membrane potential with other spiking neurons, a simple shift can be done after the simulations are done. Specifically, in Fig. 1.13, the results of voltages were shifted to $v_{\text{th}} = -50$ ms. Additionally, the LIF model does not have an actual spiking generation mechanism (Izhikevich, 2007), therefore the *spikes* in Fig. 1.6(d) are manually added whenever the neuron reaches the peak value $v_p$. In contrast, both QIF and EIF diverge whenever the threshold is crossed, and hence, the reset is done when the neuron arrives at a certain peak potential $v_p$. The resting, $v_{\text{rest}}$, and threshold, $v_{\text{th}}$, potentials of the EIF neuron in Table A.1 are numerically obtained. These values and the rheobase potential are shown in Fig. A.1.

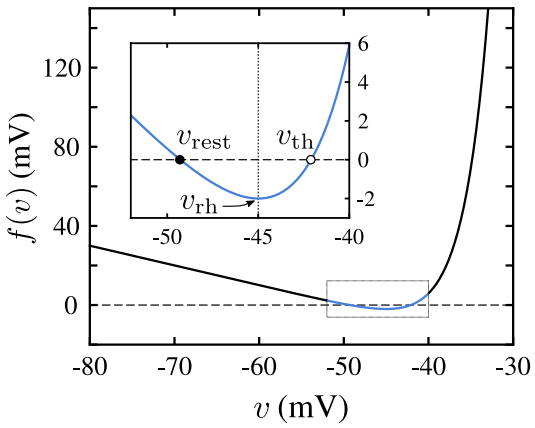


**Figure A.1:** The $f(v)$ curve of the EIF model for parameters in Table A.1.

## Properties of the heterogeneous network

In all cases we considered all-to-all networks of heterogeneous populations of neurons. On one hand, in Figs. 1.7, 1.8, 1.10 and 1.11 we modeled quenched heterogeneity by setting a constant external current for each neuron, taken from a deterministically generated (2.D.1) Lorentzian distribution (1.46), or when indicated, from a gaussian distribution. On the other hand, in Figs. 1.6, 1.9 and 1.11 we simulated identical neurons receiving time

varying inputs randomly taken from a gaussian distribution—-also known as Gaussian White Noise (GWN).

In order to describe the highly irregular activity observed in real cells, is common to consider random uncorrelated external inputs arriving at the single cells $i$. This can be mathematically written by means of a 1-dimensional stochastic differential equation (SDE) of the form

$$\tau_m \frac{dv_i}{dt} = (f(v_i) + I_i) + \sigma\eta_i(t) \tag{A.1.2}$$

where $\sigma$ is the amplitude of temporal fluctuations about the mean, and $\eta_i(t)$ is the Gaussian white-noise term. In addition, $I_i$ represent deterministic inputs arriving from both external and recurrent connections, as in Eqs. (1.31) or (2.3). The term between brackets in the left side of equation (A.1.2) is the drift coefficient, that is the deterministic part of the SDE characterizing the local trend, while the second term corresponds to the diffusion coefficient, i.e. the stochastic part affecting the average size of the fluctuations of $v_i$.

The above SDE is described in terms of the Itô scheme and can be numerically integrated using the Euler-Maruyama method:

$$v_i^{n+1} = v_i^n + \frac{dt}{\tilde{\tau}} \left(f\left(v_i^n\right) + I_i\right) + \sigma\Delta W_n, \tag{A.1.3}$$
$$\Delta W_n \sim \sqrt{\frac{dt}{\tilde{\tau}}}\mathcal{N}(0,1),$$

where $\mathcal{N}(0,1)$ denotes the normal distribution and $dt/\tilde{\tau}$ is the simulation step time. Note that the Euler-Heun method is appropriate for SDEs described in therms of the Stratonovich interpretation, and hence would probably give incorrect results in our case.

Finally, we refer the reader to the algorithm 2.D.1 for an explicit pseudocode describing the numerical integration of the QIF model neuron. The corresponding pseudocode for LIF and EIF numerical integration is similar except for the implementation of the refractory period.

### Transfer function of a population of noisy LIF neurons

A proper comparison between simulations of LIF neurons and the WC equation [Eqs. (1.5) and (1.9)] is done by taking the stationary mean firing rate of the population of LIF neurons (f-I curve) as the transfer function, $\Phi(I)$, in Eq. (1.5). Using the continuous approach and applying the Fokker-Planck equation (Siegert, 1951; Amit and Tsodyks, 1991; Roxin et al., 2011)

one can obtain the gain function of an ensemble of noisy LIF neurons:

$$\Phi(I) = \left\{ \tau_m \sqrt{\pi} \int_{v_-}^{v_+} dv\, e^{v^2} \text{erfc}(-v) \right\}^{-1}, \tag{A.1.4}$$

with $v_- = (v_{th} - E - I)/\sigma$ and $v_- = (v_r - E - I)/\sigma$. Note that $I$ is the mean input averaged over all neurons which in the particular case of an all-to-all network is just $I = \bar{\eta} + J_0 S$, with $\bar{\eta}$ being a constant external common input as in Eq. (1.47). In addition, $\text{erfc}(x)$ corresponds to the complementary error function, which in some cases appears just as the error function:

$$\Phi(I) = \left\{ \tau_m \sqrt{\pi} \int_{v_-}^{v_+} dv\, e^{v^2} \left(1 + \text{erf}(v)\right) \right\}^{-1}.$$

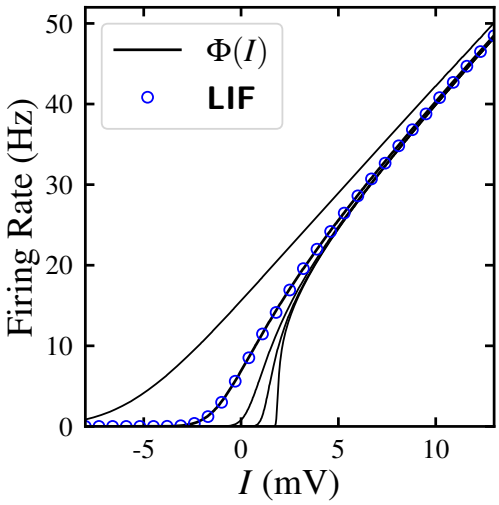


**Figure A.2:** Transfer function for a population of identical non-interacting LIF neurons under external GWN. Blue dots correspond to the firing rate of a network of LIF neurons obtained by numerically integrating Eq. (A.1.2) with $f(v) = -v + E$, using the integration method (A.1.3). Black lines are computed for different levels of diffusive noise, using Eq. (A.1.6). From top to bottom: $\sigma = 5,\ 2,\ 1,\ 0.5,\ 0.1$ mV. Other parameters are $v_r = -68$ mV, $v_{th} = -48$ mV, $E = -50$ mV, $\tau_m = 20$ ms.

However, the numerical implementation of both the error function, $\text{erf}(x)$, and the complementary error function, $\text{erfc}(x)$ can represent a challenge due to arithmetic underflow. In our particular case, we had to use the complementary error function. Finally, using the *scaled complementary error function*, $\text{erfcx}(x)$ defined as

$$\text{erfc}(x) = 1 - \text{erf}(x) = e^{-x^2} \text{erfcx}(x), \tag{A.1.5}$$

one can usually avoid errors due to arithmetic underflow, as the resulting expression for the transfer function is:

$$\Phi(I) = \left\{ \tau_m \sqrt{\pi} \int_{v_-}^{v_+} dv\, \text{erfcx}(-v) \right\}^{-1}. \tag{A.1.6}$$

Fig. A.2 shows the agreement between simulations of LIF neurons using the above integration method, and numerical results of Eq. (A.1.6).

# APPENDIX B

# Mathematical appendix

## B.1 Derivation of the firing rate equations

The mathematical derivation of the firing rate equations from the continuity equation is tedious, but not difficult. The continuity equation [Eq. (1.37)] and the Lorentzian ansatz [Eq. (1.39)] have already been introduced earlier, but is repeated here for convenience:

$$\frac{\partial \rho}{\partial t} + \frac{1}{\tau_m}\frac{\partial}{\partial v}\left[\left(v^2 + \eta + \tau_m J_0 R + I\right)\rho\right] = 0, \tag{B.1.1}$$

$$\rho = \frac{1}{\pi}\frac{x}{(v-y)^2 + x^2}, \tag{B.1.2}$$

where we have avoided to explicitly show the functional dependence of the variables; $x = x(\eta, t)$, $y = y(\eta, t)$, $R = R(t)$, $I = I(t)$, and $\rho = \rho(v|\eta, t)$. Substituting (B.1.2) into (B.1.1) and computing the derivatives, one obtains

$$\begin{aligned}\frac{\tau_m}{2}\frac{\dot{x}}{\pi A} - \frac{\tau_m x}{\pi}\frac{x\dot{x} - y(v-y)}{A^2} + \frac{xv}{\pi A} \\ - \left(v^2 + \eta + \tau_m J_0 R + I\right)\frac{x(v-y)}{\pi A^2} = 0\end{aligned} \tag{B.1.3}$$

where $A = (v-y)^2 + x^2 = v^2 + y^2 + x^2 - 2vy$ and the over-dot denotes the partial derivative over time. Then, by multiplying the equation by $\pi A$

we have

$$\frac{\tau_m \dot{x}}{2}\left(v^2+y^2+x^2-2vy\right)-\tau_m x^2\dot{x}+\tau_m x\dot{y}\,(v-y)+$$
$$xv\left(v^2+y^2+x^2-2vy\right)-x(v-y)\left(v^2+\eta+\tau_m J_0 R+I\right)=0. \tag{B.1.4}$$

We collect the terms by their order in $v$:

$$v^2\left(\frac{\tau_m\dot{x}}{2}-2xy+xy\right)=0 \tag{B.1.5a}$$
$$v\left(\tau_m y\dot{x}+\tau_m x\dot{y}+x\left(x^2+y^2\right)-x\left(\eta+\tau_m J_0 R+I\right)\right)=0 \tag{B.1.5b}$$
$$\frac{\tau_m\dot{x}}{2}\left(x^2+y^2\right)-\tau x^2\dot{x}-\tau xy\dot{y}+xy\left(\eta+\tau_m J_0 R+I\right)=0. \tag{B.1.5c}$$

Eq. (B.1.5a) is just

$$\tau_m\dot{x}=2xy, \tag{B.1.6}$$

and substituting into (B.1.5b), we obtain a second equation

$$\tau_m\dot{y}=y^2+(\eta+I+J_0R)-x^2. \tag{B.1.7}$$

The third equation, Eq. (B.1.5c), is a linear combination of the other two. This system of differential equations can be represented by a single complex differential equation using $w(\eta,t)\equiv x(\eta,t)+iy(\eta,t)$, which leads to Eq. (1.45):

$$\tau_m\frac{\partial w}{\partial t}=i\left[\eta+\tau_m J_0 R-w^2+I\right]. \tag{B.1.8}$$

### B.1.1 Reduction to a system of two ODEs: QIF-FREs

Following the derivation in the main text [Section 1.3.4] we can choose a Lorentzian distribution for the external currents [Eq. (1.46)], reducing the dimensionality of the system to a system of two coupled ODEs. The integrals (1.41) and (1.43) can be computed applying the residue theorem as described in the following steps.

First, the integrals to be solved are of the type:

$$I=\frac{\Delta}{\pi}\int_{-\infty}^{\infty}\frac{h(\eta,t)}{(\eta-\bar{\eta})^2+\Delta^2}d\eta, \tag{B.1.9}$$

with $h$ being $x$ or $y$. The only constrains we must take into account is that $x,y\in\mathbb{R}$ and $x(\eta,t)\geq 0$, $\forall t\geq 0$ in order the distribution to make sense.

Having this in mind, the integral can be solved using the residue theorem, and has the general form

$$\int_C f(z)dz = 2\pi i \sum_{k=1}^{n} I\left(C, a_k\right) \mathrm{Res}\left(f, a_k\right) \tag{B.1.10}$$

where $C$ is the contour that encloses the pole(s) $a_k$, $I$ denotes the winding number of $C$ around $a_k$, and $\mathrm{Res}(f, a_k)$ are the residues of $f$ at $a_k$. The poles of $f(z)$ for well-defined functions of $x$ and $y$ are calculated by finding the corresponding Laurent series expansion, and taking coefficients $a_{-1}$:

$$f(z) = \frac{h(z,t)}{2i\Delta}\left(\frac{1}{z-\bar{\eta}-i\Delta} - \frac{1}{z-\bar{\eta}+i\Delta}\right). \tag{B.1.11}$$

The poles, therefore, are $a_+ = \bar{\eta} + i\Delta$ and $a_- = \bar{\eta} - i\Delta$.

Now, the choice of $C$ enclosing the pole(s) needs to take into account the constrain mentioned above, i.e. that $x$ must remain positive for all values of $\eta$. Thus, we make an analytic continuation of $w(\eta, t)$ from real $\eta$ into the complex-valued $\eta = \eta_R + i\eta_I = z$. Substituting into Eq. (B.1.8) we have

$$\tau_m \frac{dx}{dt} = -\eta_I + 2xy, \tag{B.1.12a}$$

$$\tau_m \frac{dv}{dt} = y^2 + \eta_R - x^2 + \tau_m J_0 R + I. \tag{B.1.12b}$$

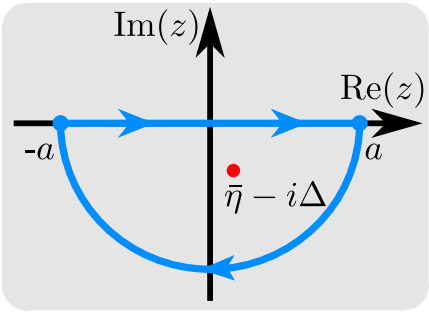


**Figure B.1:** The contour $C$ encloses the pole $\bar{\eta} - i\Delta$, $\Delta > 0$.

At $x = 0$, Eq. (B.1.12a) is $\tau_m \dot{x} = -\eta_I$ which requires $\eta_I < 0$ to maintain a positive value of $x$. Therefore we need to consider the pole in the lower half plane of $z$, and consequently $C$ is the contour that goes along the real line from $-a$ to $a$ and then clockwise along a semicircle centered at 0 from $a$ to $-a$ as shown in Fig. B.1. The residue of $f$ at such pole $z_p = \bar{\eta} - i\Delta$ is $\mathrm{Res}_{z_p} f(z) = -h(\bar{\eta} - i\Delta, t)/(2i\Delta)$, and the integral (B.1.9) becomes

$$\int_C f(z)dz = 2\pi i\,(-1)\,\frac{-h(\bar{\eta}-i\Delta,t)}{2i\Delta} = \frac{\pi h(\bar{\eta}-i\Delta,t)}{\Delta}. \tag{B.1.13}$$

Finally the integral (B.1.9) is

$$I = h(\bar{\eta} - i\Delta, t) - \int_{\text{arc}} f(z)dz = h(\bar{\eta} - i\Delta), \tag{B.1.14}$$

where we used $\int_C = \int_{\text{straight}} + \int_{\text{arc}}$, being the integral over the straight line the original integral. By estimation, is easy to see that the integral over the arc vanishes as $a \to \infty$.

Therefore the integrals (1.41) and (1.43) are just:

$$R(t) = \frac{x(\bar{\eta} - i\Delta)}{\pi\tau_m} \quad \text{and} \quad V(t) = y(\bar{\eta} - i\Delta), \tag{B.1.15}$$

which finally leads to the QIF-FREs (1.47).

## B.2 QIF-FREs for conductance-based spiking neurons

Going back to the QIF neuron model, Eqs.(1.30) and (1.32), we can now define the conductance-based QIF neuron in the following way

$$\begin{aligned}\tau\frac{dv_j}{dt} = v_j^2 + (\eta_j - v_j) - a_e\tau S_e(t)(v_j - E_e) \\ - a_i\tau S_i(t)(v_j - E_i) + P(t),\end{aligned} \tag{B.2.1}$$

where $a_\alpha$ and $E_\alpha$ correspond to the excitatory or inhibitory ($\alpha = e, i$) synaptic conductance and reversal potential, respectively. And $S_\alpha$ is the synaptic activation due to excitatory or inhibitory synaptic efferents. Notice that, the method used to reduce the dimensionality of the network admits any representation of the QIF neuron of the form (Montbrió et al., 2015):

$$\tau_m\frac{dv_j}{dt} = v_j^2 A(\mathbf{x}_j, t) + v_j B(\mathbf{x}_j, t) + C(\mathbf{x}_j, t), \tag{B.2.2}$$

with $A$, $B$, and $C$ being functions which may depend on a parameter, or a set of parameters, distributed in a similar way as the external currents in Eq. (1.31) or (B.2.1). A detailed proof of this generalization is given in (Montbrió et al., 2015). For the particular case $A = 1$, the complex valued solution of the continuity equation (1.37) corresponding to the system (B.2.2) reads

$$\tau_m\frac{dw}{dt} = i\left[C - w^2\right] + Bw. \tag{B.2.3}$$

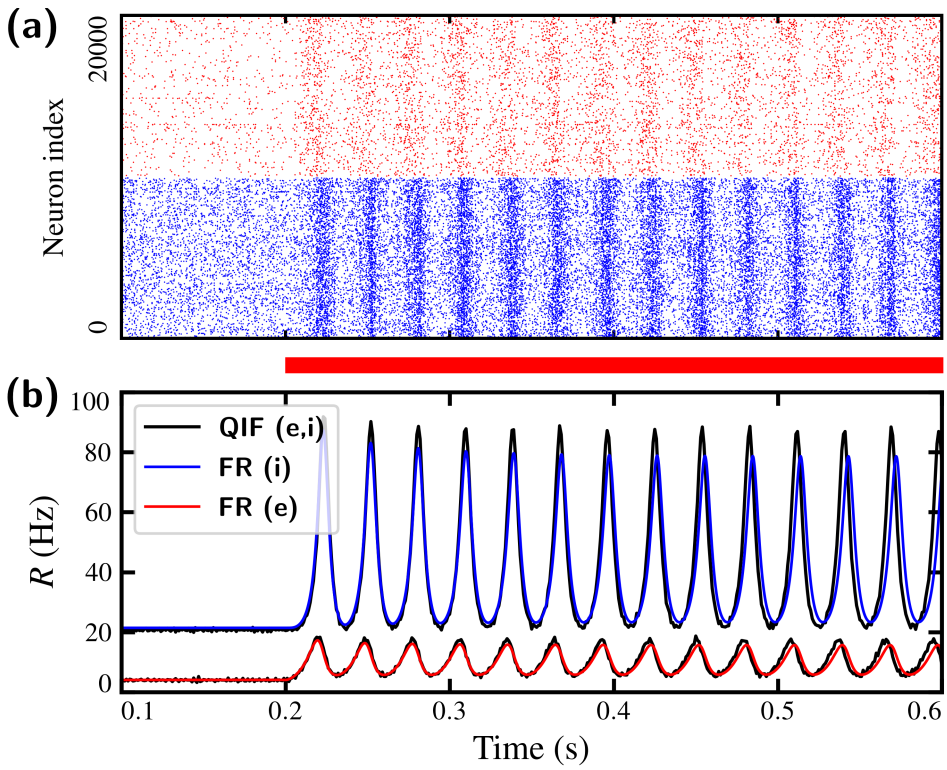


**Figure B.1:** PING oscillations (see section 1.1.1.2) in a network of $N = 2 \cdot 10^4$ (1:1) conductance-based QIF neurons (B.2.1). At time 0.2 s the external current of the excitatory population is increased from $\bar{\eta}_e = 1$ to $\bar{\eta}_e = 8$ and the system starts to oscillate. **(a)** Raster plot of the excitatory (in red) and the inhibitory (in blue) populations. **(b)** Firing rate of both populations. The black lines in the back correspond to simulations of the spiking neural network, while the red and the blue lines in the front are computed using the QIF-FREs (B.2.6) and they represent the excitatory and the inhibitory firing rate, respectively. Parameters are: $\tau_e = 20$ ms, $\tau_i = 10$ ms, $\Delta = 1$, $\bar{\eta}_i = -1$, $\bar{\eta}_e = 1 \to 8$, $J_{ei} = 3$, $J_{ie} = 1$, $a_e = a_i = 1$, $E_i = -10$, $E_e = 10$, $J_{ee} = J_{ii} = 0$.

For the specific neuron model (B.2.1), functions $B$ and $C$ are:

$$B(t) = 1 + a_e \tau_m S_e(t) + a_i \tau_m S_i(t), \tag{B.2.4}$$

$$C(\eta, t) = \eta + P(t) + a_e E_e \tau_m S_e(t) + a_i E_i \tau_m S_i(t) \tag{B.2.5}$$

Following the same derivation as in the previous section we arrive at the QIF-FREs for "conductance-based" QIF neurons:

$$\tau_m \frac{dR}{dt} = \frac{\Delta}{\tau_m \pi} + 2RV - \tau_m R \left( \frac{1}{\tau_m} + a_e S_e(t) + a_i S_i(t) \right) \quad \text{(B.2.6a)}$$

$$\tau_m \frac{dV}{dt} = V^2 + \bar{\eta} - (\pi \tau_m R)^2 - V - \tau_m \left[ a_e S_e(t) \left( V - E_e \right) + a_i S_i(t) \left( V - E_i \right) \right] + P(t). \quad \text{(B.2.6b)}$$

**Conductance-based QIF-FREs**

A similar result was obtained by Ratas and Pyragas (2016) where they used voltage-dependent synapses.

In contrast to the current-based QIF-FREs (1.47), here, the firing rate saturates for large values of the synaptic coupling, therefore it is indeed a more realistic model and represents a step forward towards more realistic conductance-based population models. Finally, in Fig. B.1 we show an example of PING oscillations in a two-population network of conductance-based QIF neurons (B.2.1) showing good—except for finite size-effects—agreement between the spiking network model (black line) and the QIF-FREs (colored lines).

# References


Abbott, L. F. (1999). Lapicque's introduction of the integrate-and-fire model neuron (1907). *Brain Research Bulletin*, 50(5-6):303–304.

Abbott, L. F. and Van Vreeswijk, C. (1993). Asynchronous states in networks of pulse-coupled oscillators. *Physical Review E*, 48(2):1483–1490.

Amari, S.-I. (1972). Characteristics of Random Nets of Analog Neuron-Like Elements. *IEEE Transactions on Systems, Man and Cybernetics*, 2(5):643–657.

Amari, S.-I. (1974). A method of statistical neurodynamics. *Kybernetik*, 14(4):201–215.

Amari, S.-I. (1977). Dynamics of pattern formation in lateral-inhibition type neural fields. *Biological cybernetics*, 87:77–87.

Amit, D. and Brunel, N. (1997). Model of global spontaneous activity and local structured activity during delay periods in the cerebral cortex. *Cerebral Cortex*, 7(3):237–252.

Amit, D. J. and Tsodyks, M. V. (1991). Quantitative study of attractor neural network retrieving at low spike rates: I. Substrate - spikes, rates and neuronal gain. *Network: Computation in Neural Systems*, 2(3):259–273.

Atasoy, S., Donnelly, I., and Pearson, J. (2016). Human brain networks function in connectome-specific harmonic waves. *Nature Communications*, 7:10340.

Atay, F. M. and Hutt, A. (2004). Stability and Bifurcations in Neural Fields with Finite Propagation Speed and General Connectivity. *SIAM Journal on Applied Mathematics*, 65(2):644–666.

Avitabile, D. (2016). Numerical computation of coherent structures in spatially-extended systems. *Second International Conference on Mathematical Neuroscience, Antibes Juan-les-Pins*.

Avitabile, D., Desroches, M., and Knobloch, E. (2017). Spatiotemporal canards in neural field equations. *Physical Review E*, 95(4):1–8.

Badel, L., Lefort, S., Brette, R., Petersen, C. C. H., Gerstner, W., and Richardson, M. J. E. (2008). Dynamic I-V Curves Are Reliable Predictors of Naturalistic Pyramidal-Neuron Voltage Traces. *Journal of Neurophysiology*, 99(2):656–666.

Bartos, M., Vida, I., and Jonas, P. (2007). Synaptic mechanisms of synchronized gamma oscillations in inhibitory interneuron networks. *Nature Reviews Neuroscience*, 8(1):45–56.

Battaglia, D., Brunel, N., and Hansel, D. (2007). Temporal Decorrelation of Collective Oscillations in Neural Networks with Local Inhibition and Long-Range Excitation. *Phys. Rev. Lett.*, 99(23):238106.

Beer, R. D. (1995). On the Dynamics of Small Continuous-Time Recurrent Neural Networks. *Adaptive Behavior*, 3(4):469–509.

Ben-Yishai, R., Bar-Or, R. L., and Sompolinsky, H. (1995). Theory of orientation tuning in visual cortex. *Proceedings of the National Academy of Sciences*, 92(9):3844–3848.

Bennett, M. V. and Zukin, R. (2004). Electrical Coupling and Neuronal Synchronization in the Mammalian Brain. *Neuron*, 41(4):495–511.

Beurle, R. L. (1956). Properties of a mass of cells capable of regenerating pulses. *Philosophical Transactions of the Royal Society of London. Series B, Biological Sciences*, 240(669):55–94.

Bicho, E., Erlhagen, W., Louro, L., and Costa e Silva, E. (2011). Neuro-cognitive mechanisms of decision making in joint action: A human-robot interaction study. *Human Movement Science*, 30(5):846–868.

Börgers, C. and Kopell, N. (2003). Synchronization in networks of excitatory and inhibitory neurons with sparse, random connectivity. *Neural computation*, 15:509–538.

Bressloff, P. C. (2012). Spatiotemporal dynamics of continuum neural fields. *Journal of Physics A: Mathematical and Theoretical*, 45(3):033001.

Bressloff, P. C., Cowan, J. D., Golubitsky, M., Thomas, P. J., and Wiener, M. C. (2001). Geometric visual hallucinations, Euclidean symmetry and the functional architecture of striate cortex. *Philosophical Transactions of the Royal Society B: Biological Sciences*, 356(1407):299–330.

Bressloff, P. C. and Webber, M. A. (2012). Neural field model of binocular rivalry waves. *Journal of Computational Neuroscience*, 32(2):233–252.

Brunel, N. (2000). Dynamics of sparsely connected networks of excitatory and inhibitory spiking neurons. *Journal of Computational Neuroscience*, 8(3):183–208.

Brunel, N., Chance, F. S., Fourcaud, N., and Abbott, L. F. (2001). Effects of synaptic noise and filtering on the frequency response of spiking neurons. *Physical Review Letters*, 86(10):2186–2189.

Brunel, N. and Hakim, V. (1999). Fast global oscillations in networks of integrate-and-fire neurons with low firing rates. *Neural computation*, 11(7):1621–1671.

Brunel, N. and Hakim, V. (2008). Sparsely synchronized neuronal oscillations. *Chaos*, 18(1).

Brunel, N. and Van Rossum, M. C. (2007a). Lapicque's 1907 paper: From frogs to integrate-and-fire. *Biological Cybernetics*, 97(5-6):337–339.

Brunel, N. and Van Rossum, M. C. (2007b). Quantitative investigations of electrical nerve excitation treated as polarization. *Biological Cybernetics*, 97(5-6):341–349.

Brunel, N. and Wang, X.-J. (2003). What determines the frequency of fast network oscillations with irregular neural discharges? I. Synaptic dynamics and excitation-inhibition balance. *Journal of neurophysiology*, 90(1):415–430.

Buia, C. and Tiesinga, P. (2006). Attentional modulation of firing rate and synchrony in a model cortical network. *Journal of Computational Neuroscience*, 20(3):247–264.

Buzsáki, G. and Draguhn, A. (2004). Neuronal oscillations in cortical networks. *Science (New York, N.Y.)*, 304(5679):1926–9.

Buzsáki, G. and Moser, E. I. (2013). Memory, navigation and theta rhythm in the hippocampal-entorhinal system. *Nature Neuroscience*, 16(2):130–138.

Buzsáki, G. and Wang, X.-J. (2012). Mechanisms of Gamma Oscillations. *Annual Review of Neuroscience*, 35(1):203–225.

Byrne, Á., Brookes, M. J., and Coombes, S. (2017). A mean field model for movement induced changes in the beta rhythm. *Journal of Computational Neuroscience*, 43(2):143–158.

Chandra, S., Hathcock, D., Crain, K., Antonsen, T. M., Girvan, M., and Ott, E. (2017). Modeling the network dynamics of pulse-coupled neurons. *Chaos*, 27(3).

Compte, A. (2000). Synaptic Mechanisms and Network Dynamics Underlying Spatial Working Memory in a Cortical Network Model. *Cerebral Cortex*, 10(9):910–923.

Coombes, S. (2005). Waves, bumps, and patterns in neural field theories. *Biological Cybernetics*, 93(2):91–108.

Coombes, S. (2010). Large-scale neural dynamics: Simple and complex. *NeuroImage*, 52(3):731 – 739. Computational Models of the Brain.

Coombes, S., beim Graben, P., and Potthast, R. (2014). Tutorial on neural field theory. In *Neural fields*, pages 1–43. Springer.

Coombes, S. and Byrne, Á. (2019). Next generation neural mass models. In *Lecture Notes in Nonlinear Dynamics in Computational Neuroscience: from Physics and Biology to ICT*. Springer. In press.

Coombes, S. and Laing, C. (2009). Delays in activity-based neural networks. *Philosophical transactions. Series A, Mathematical, physical, and engineering sciences*, 367(1891):1117–29.

Coombes, S., Lord, G. J., and Owen, M. R. (2003). Waves and bumps in neuronal networks with axo-dendritic synaptic interactions. *Physica D: Nonlinear Phenomena*, 178(3-4):219–241.

Cowan, J. (2014). *A Personal Account of the Development of the Field Theory of Large-Scale Brain Activity from 1945 Onward*, pages 47–96. Springer Berlin Heidelberg, Berlin, Heidelberg.

Cragg, B. and Temperley, H. (1954). The organisation of neurones: A co-operative analogy. *Electroencephalography and Clinical Neurophysiology*, 6(1952):85–92.

Deco, G., Jirsa, V. K., Robinson, P. a., Breakspear, M., and Friston, K. (2008). The dynamic brain: from spiking neurons to neural masses and cortical fields. *PLoS computational biology*, 4(8):e1000092.

Destexhe, A. and Sejnowski, T. J. (2009). The Wilson-Cowan model, 36 years later. *Biological Cybernetics*, 101(1):1–2.

Devalle, F., Roxin, A., and Montbrió, E. (2017a). Firing rate equations require a spike synchrony mechanism to correctly describe fast oscillations in inhibitory networks. *PLoS Computational Biology*, 13(12):1–21.

Devalle, F., Roxin, A., and Montbrió, E. (2017b). Firing rate equations require a spike synchrony mechanism to correctly describe fast oscillations in inhibitory networks. *in Preparation [Confidentially]*, pages 1–21.

Dijkstra, K., Gils, S. A. V., Janssens, S. G., Kuznetsov, Y. A., and Visser, S. (2015). Pitchfork-Hopf bifurcations in 1D neural field models with transmission delays. *Physica D: Nonlinear Phenomena*, 297:88–101.

Dipoppa, M. and Gutkin, B. S. (2013a). Correlations in background activity control persistent state stability and allow execution of working memory tasks. *Frontiers in Computational Neuroscience*, 7(October):139.

Dipoppa, M. and Gutkin, B. S. (2013b). Flexible frequency control of cortical oscillations enables computations required for working memory. *Proceedings of the National Academy of Sciences of the United States of America*, 110(31):12828–33.

Dumont, G., Ermentrout, G. B., and Gutkin, B. (2017). Macroscopic phase-resetting curves for spiking neural networks. *Physical Review E*, 96(4):1–8.

Durstewitz, D. and Wang, X.-J. (2003). Self-organizing neural integrator predicts interval times through climbing activity. *The Journal of neuroscience : the official journal of the Society for Neuroscience*, 23(12):5342–53.

Ermentrout, B. (1994). Reduction of Conductance-Based Models with Slow Synapses to Neural Nets. *Neural Computation*, 6(4):679–695.

Ermentrout, B. (1998). Neural networks as spatio-temporal pattern-forming systems. *Reports on Progress in Physics*, 61(4):353–430.

Ermentrout, G. B. (1996). Type I neurons, phase resettings curves and synchrony. *Neural Comput*, 8(5):979–1001.

Ermentrout, G. B. and Cowan, J. D. (1979). A Mathematical Theory of Visual Hallucinatory Patterns. *Biological Cybernetics*, 34:137–150.

Ermentrout, G. B. and Cowan, J. D. (1980). Large Scale Spatially Organized Activity in Neural Nets. *SIAM Journal on Applied Mathematics*, 38(1):1–21.

Ermentrout, G. B. and Kopell, N. (1986). Parabolic Bursting in an Excitable System Coupled with a Slow Oscillation.

Ermentrout, G. B. and McLeod, J. B. (1993). Existence and uniqueness of travelling waves for a neural network. *Proceedings of the Royal Society of Edinburgh: Section A Mathematics*, 123(03):461–478.

Ermentrout, G. B. and Terman, D. H. (2010). *Mathematical foundations of neuroscience*, volume 64. Springer.

Esnaola-Acebes, J. M., Roxin, A., Avitabile, D., and Montbrió, E. (2017). Synchrony-induced modes of oscillation of a neural field model. *Physical Review E*, 96(5):052407.

Fisahn, A., Pike, F. G., Buhl, E. H., and Paulsen, O. (1998). Cholinergic induction of network oscillations at 40 Hz in the hippocampus in vitro. *Nature*, 394(6689):186–189.

Fourcaud-Trocmé, N., Hansel, D., van Vreeswijk, C., and Brunel, N. (2003). How spike generation mechanisms determine the neuronal response to fluctuating inputs. *J. Neurosci.*, 23(37):11628–11640.

Freeman, W. J. (1964). A linear distributed feedback model for prepyriform cortex. *Experimental Neurology*, 10(6):525–547.

Freeman, W. J. (1975). *Mass action in the nervous system : examination of the neurophysiological : examination of the neurophysiological basis of adaptive behavior trough the EEG.* Academic Press, New York.

Fusi, S. and Mattia, M. (1999). Collective Behavior of Networks with Linear (VLSI) Integrate-and-Fire Neurons. *Neural Computation*, 11(3):633–652.

Gallego, R., Montbrió, E., and Pazó, D. (2017). Synchronization scenarios in the Winfree model of coupled oscillators. *Physical Review E*, 96(4):1–11.

Geisler, C. D. and Goldberg, J. M. (1966). A Stochastic Model of the Repetitive Activity of Neurons. *Biophysical Journal*, 6(1):53–69.

Gerstner, W. (2000). Population dynamics of spiking neurons: fast transients, asynchronous states, and locking. *Neural Comput.*, 12(1):43–89.

Gerstner, W., Kistler, W. M., Naud, R., and Paninski, L. (2014). *Neuronal dynamics : from single neurons to networks and models of cognition*. Cambridge University Press, Cambridge, United Kingdom.

Gibson, J. R., Beierlein, M., and Connors, B. W. (1999). Two networks of electrically coupled inhibitory neurons in neocortex. *Nature*, 402(6757):75–79.

Giese, M. A. (1999). *Dynamic Neural Field Theory for Motion Perception*. Springer US, Boston, MA.

Gloveli, T., Kopell, N., and Dugladze, T. (2010). Neuronal Activity Patterns During Hippocampal Network Oscillations In Vitro. In Cutsuridis, V., Graham, B., Cobb, S., and Vida, I., editors, *Hippocampal Microcircuits*, pages 247–276. Springer New York, New York, NY.

Griffith, J. S. (1963). On the stability of brain-like structures. *Biophysical journal*, 3:299–308.

Grossberg, S. (1973). Contour Enhancement, Short Term Memory, and Constancies in Reverberating Neural Networks. *Studies in Applied Mathematics*, 52(3):213–257.

Gutkin, B. S. and Ermentrout, G. B. (1998). Dynamics of Membrane Excitability Determine Interspike Interval Variability: A Link between Spike Generation Mechanisms and Cortical Spike Train Statistics. *Neural Computation*, 10(5):1047–1065.

Gutkin, B. S., Laing, C. R., Colby, C. L., Chow, C. C., and Ermentrout, G. B. (2001). Turning on and off with excitation: The role of spike-timing asynchrony and synchrony in sustained neural activity. *Journal of Computational Neuroscience*, 11(2):121–134.

Hansel, D. and Mato, G. (2001). Existence and stability of persistent states in large neuronal networks. *Physical Review Letters*, 86(18):4175–4178.

Hansel, D. and Mato, G. (2003). Asynchronous States and the Emergence of Synchrony in Large Networks of Interacting Excitatory and Inhibitory Neurons. *Neural Computation*, 15(1):1–56.

Hansel, D. and Sompolinsky, H. (1998). Modeling Feature Selectivity in Local Cortical Circuits. *Methods in Neuronal Modeling: From Ions to Networks*, pages 499–567.

Hill, A. V. (1936). Excitation and accommodation in nerve. *Proceedings of the Royal Society of London. Series B, Biological Sciences*, 119(814):305–355.

Hodgkin, A. and Huxley, A. (1952). A quantitative description of membrane current and its application to conduction and excitation in nerve. *The Journal of physiology*, pages 500–544.

Hoppensteadt, F. C. and Izhikevich, E. M. (1997). *Weakly Connected Neural Networks*, volume 126 of *Applied Mathematical Sciences*. Springer New York, New York, NY.

Hubel, D. H. and Wiesel, T. N. (1962). Receptive fields, binocular interaction and functional architecture in the cat's visual cortex. *The Journal of Physiology*, 160(1):106–154.

Hubel, D. H. and Wiesel, T. N. (1968). Receptive fields and functional architecture of monkey striate cortex. *The Journal of physiology*, 195(1):215–43.

Hutt, A. (2008). Local excitation-lateral inhibition interaction yields oscillatory instabilities in nonlocally interacting systems involving finite propagation delay. *Physics Letters, Section A: General, Atomic and Solid State Physics*, 372(5):541–546.

Izhikevich, E. M. (2007). *Dynamical Systems in Neuroscience: The Geometry of Excitability and Burtsing*. The MIT Press, Cambridge, Massachusetts.

Jansen, B. H. and Rit, V. G. (1995). Electroencephalogram and visual evoked potential generation in a mathematical model of coupled cortical columns. *Biological Cybernetics*, 73(4):357–366.

Jirsa, V. and Haken, H. (1997). A derivation of a macroscopic field theory of the brain from the quasi-microscopic neural dynamics. *Physica D: Nonlinear Phenomena*, 99(4):503–526.

Jirsa, V., Jantzen, K., Fuchs, A., and Kelso, J. (2002). Spatiotemporal forward solution of the EEG and MEG using network modeling. *IEEE Transactions on Medical Imaging*, 21(5):493–504.

Jirsa, V. K., Jantzen, K. J., Fuchs, A., and Kelso, J. S. (2001). Neural field dynamics on the folded three-dimensional cortical sheet and its forward eeg and meg. In Insana, M. F. and Leahy, R. M., editors, *Information Processing in Medical Imaging*, pages 286–299, Berlin, Heidelberg. Springer Berlin Heidelberg.

Kawamura, Y. (2014). From the Kuramoto-Sakaguchi model to the Kuramoto-Sivashinsky equation. *Physical Review E*, 2(11):1–6.

Keeley, S., Fenton, A. A., and Rinzel, J. (2017). Modeling fast and slow gamma oscillations with interneurons of different subtype. *Journal of Neurophysiology*, 117(3):950–965.

Kilpatrick, Z. and Bressloff, P. (2010). Binocular Rivalry in a Competitive Neural Network with Synaptic Depression. *SIAM Journal on Applied Dynamical Systems*, 9(4):1303–1347.

Knight, B. W. (1972). Dynamics of encoding in a population of neurons. *The Journal of general physiology*, 59(6):734–766.

Kopell, N., Börgers, C., Pervouchine, D., Malerba, P., and Tort, A. (2010). Gamma and Theta Rhythms in Biophysical Models of Hippocampal Circuits. In Cutsuridis, V., Graham, B., Cobb, S., and Vida, I., editors, *Hippocampal Microcircuits: A Computational Modeler's Resource Book*, pages 423–457. Springer New York, New York, NY.

Kuramoto, Y. (1984). *Chemical Oscillations, Waves, and Turbulence*, volume 19 of *Springer Series in Synergetics*. Springer Berlin Heidelberg, Berlin, Heidelberg.

Laing, C. R. (2009). The dynamics of chimera states in heterogeneous Kuramoto networks. *Physica D: Nonlinear Phenomena*, 238(16):1569–1588.

Laing, C. R. (2014). Derivation of a neural field model from a network of theta neurons. *Physical Review E*, 90(1):010901.

Laing, C. R. (2015). Exact Neural Fields Incorporating Gap Junctions. *SIAM Journal on Applied Dynamical Systems*, 14(4):1899–1929.

Laing, C. R. (2016a). Bumps in Small-World Networks. *Front Comput Neurosci*, 10(June):53.

Laing, C. R. (2016b). Travelling waves in arrays of delay-coupled phase oscillators. *Chaos*, 26(9).

Laing, C. R. (2018). The Dynamics of Networks of Identical Theta Neurons. *Journal of Mathematical Neuroscience*, 8(1).

Laing, C. R. and Troy, W. C. (2003). Two-bump solutions of Amari-type models of neuronal pattern formation. *Physica D: Nonlinear Phenomena*, 178(3-4):190–218.

Laing, C. R., Troy, W. C., Gutkin, B., and Ermentrout, G. B. (2002). Multiple Bumps in a Neuronal Model of Working Memory. *SIAM Journal on Applied Mathematics*, 63(1):62–97.

Latham, P. E., Richmond, B. J., Nelson, P. G., and Nirenberg, S. (2000). Intrinsic dynamics in neuronal networks. I. Theory. *Journal of Neurophysiology*, 83(2):808–827.

Ledoux, E. and Brunel, N. (2011). Dynamics of Networks of Excitatory and Inhibitory Neurons in Response to Time-Dependent Inputs. *Frontiers in Computational Neuroscience*, 5:25.

Lee, W. S., Ott, E., and Antonsen, T. M. (2009). Large Coupled Oscillator Systems with Heterogeneous Interaction Delays. *Phys. Rev. Lett.*, 103(4):44101.

Liley, D., Cadusch, P., and Dafilis, M. (2002). A spatially continuous mean field theory of electrocortical activity. *Network: Computation in Neural Systems*, 13(1):67–113.

Lo, C.-C. and Wang, X.-J. (2006). Cortico-basal ganglia circuit mechanism for a decision threshold in reaction time tasks. *Nature Neuroscience*, 9(7):956–963.

Lodato, S. and Arlotta, P. (2015). Generating Neuronal Diversity in the Mammalian Cerebral Cortex. *Annual Review of Cell and Developmental Biology*, 31(1):699–720.

Luke, T. B., Barreto, E., and So, P. (2013). Complete classification of the macroscopic behavior of a heterogeneous network of theta neurons. *Neural Comput.*, 25(12):3207–3234.

Lund, J. S., Angelucci, A., and Bressloff, P. C. (2003). Anatomical substrates for functional columns in macaque monkey primary visual cortex. *Cerebral Cortex*, 13(1):15–24.

Martí, D., Deco, G., Mattia, M., Gigante, G., and Del Giudice, P. (2008). A fluctuation-driven mechanism for slow decision processes in reverberant networks. *PLoS ONE*, 3(7).

Martí, D. and Rinzel, J. (2013). Dynamics of feature categorization. *Neural computation*, 25:1–45.

Martin, K. A. C. (1988). THE WELLCOME PRIZE LECTURE FROM SINGLE CELLS TO SIMPLE CIRCUITS IN THE CEREBRAL CORTEX. *Quarterly Journal of Experimental Physiology*, 73(5):637–702.

McCulloch, W. S. and Pitts, W. (1943). A logical calculus of the ideas immanent in nervous activity. *The Bulletin of Mathematical Biophysics*, 5(4):115–133.

Montbrió, E. and Pazó, D. (2018). Kuramoto Model for Excitation-Inhibition-Based Oscillations. *Physical Review Letters*, 120(24):244101.

Montbrió, E., Pazó, D., and Roxin, A. (2015). Macroscopic description for networks of spiking neurons. *Physical Review X*, 5(2):1–15.

Mountcastle, V. (1997). The columnar organization of the neocortex. *Brain*, 120(4):701–722.

Mountcastle, V. B. (1957). Modality and Topographic Properties of Single Neurons of Cat's Somatic Sensory Cortex. *Journal of Neurophysiology*, 20(4):408–434.

Naud, R. and Gerstner, W. (2012). Coding and Decoding with Adapting Neurons: A Population Approach to the Peri-Stimulus Time Histogram. *PLoS Computational Biology*, 8(10).

Nunez, P. L. (1974). The brain wave equation: a model for the EEG. *Mathematical Biosciences*, 21(3-4):279–297.

Nunez, P. L. and Srinivasan, R. (2009). *Electric Fields of the Brain: The neurophysics of EEG*.

Nykamp, D. and Tranchina, D. (2000). A population density approach that facilitates large-scale modeling of neural networks: analysis and an application to orientation tuning. *Journal of computational neuroscience*, 8(1):19–50.

Nykamp, D. Q., Friedman, D., Shaker, S., Shinn, M., Vella, M., Compte, A., and Roxin, A. (2017). Mean-field equations for neuronal networks with arbitrary degree distributions. *Physical Review E*, 95(4):042323.

O'Keeffe, K. P. and Strogatz, S. H. (2016). Dynamics of a population of oscillatory and excitable elements. *Physical Review E*, 93(6):1–8.

Omel'chenko, O. E. (2013). Coherence–incoherence patterns in a ring of non-locally coupled phase oscillators. *Nonlinearity*, 26(9):2469.

Omel'chenko, O. E., Wolfrum, M., and Laing, C. R. (2014). Partially coherent twisted states in arrays of coupled phase oscillators. *Chaos: An Interdisciplinary Journal of Nonlinear Science*, 24(2):023102.

Omurtag, A., Knight, B. W., and Sirovich, L. (2000). On the simulation of large populations of neurons. *J Comput Neurosci*, 8:51–63.

Ott, E. and Antonsen, T. M. (2008). Low dimensional behavior of large systems of globally coupled oscillators. *Chaos (Woodbury, N.Y.)*, 18(3):037113.

Ott, E. and Antonsen, T. M. (2009). Long time evolution of phase oscillator systems. *Chaos*, 19(2).

Ott, E., Hunt, B. R., and Antonsen, T. M. (2011). Comment on "Long time evolution of phase oscillators systems". *Chaos*, 21:25112.

Pazó, D. and Montbrió, E. (2014). Low-dimensional dynamics of populations of pulse-coupled oscillators. *Phys. Rev. X*, 4:011009.

Pazó, D. and Montbrió, E. (2016). From Quasiperiodic Partial Synchronization to Collective Chaos in Populations of Inhibitory Neurons with Delay. *Physical Review Letters*, 116(23):238101.

Pecora, L. M. (1998). Synchronization conditions and desynchronizing patterns in coupled limit-cycle and chaotic systems. *Physical Review E*, 58(1):347–360.

Pecora, L. M. and Carroll, T. L. (1998). Master Stability Functions for Synchronized Coupled Systems. *Physical Review Letters*, 80(10):2109–2112.

Pinto, D. J. and Ermentrout, G. B. (2001a). Spatially Structured Activity in Synaptically Coupled Neuronal Networks: I. Traveling Fronts and Pulses. *SIAM Journal on Applied Mathematics*, 62(1):206–225.

Pinto, D. J. and Ermentrout, G. B. (2001b). Spatially Structured Activity in Synaptically Coupled Neuronal Networks: II. Lateral Inhibition and Standing Pulses. *SIAM Journal on Applied Mathematics*, 62(1):226–243.

Rabinovich, M. I., Huerta, R., Varona, P., and Afraimovich, V. S. (2008). Transient cognitive dynamics, metastability, and decision making. *PLoS Computational Biology*, 4(5):25–30.

Rankin, J., Avitabile, D., Baladron, J., Faye, G., and Lloyd, D. J. B. (2014). Continuation of Localized Coherent Structures in Nonlocal Neural Field Equations. *SIAM Journal on Scientific Computing*, 36(1):B70–B93.

Ratas, I. and Pyragas, K. (2016). Macroscopic self-oscillations and aging transition in a network of synaptically coupled quadratic integrate-and-fire neurons. *Physical Review E - Statistical, Nonlinear, and Soft Matter Physics*, 94(3):1–11.

Ratas, I. and Pyragas, K. (2017). Symmetry breaking in two interacting populations of quadratic integrate-and-fire neurons. *Physical Review E*, 96(4):1–9.

Richardson, M. J. E. (2007). Firing-rate response of linear and nonlinear integrate-and-fire neurons to modulated current-based and conductance-based synaptic drive. *Physical Review E - Statistical, Nonlinear, and Soft Matter Physics*, 76(2):1–15.

Roberts, M. J., Lowet, E., Brunet, N. M., TerWal, M., Tiesinga, P., Fries, P., and DeWeerd, P. (2013). Robust gamma coherence between macaque V1 and V2 by dynamic frequency matching. *Neuron*, 78(3):523–536.

Roulet, J. and Mindlin, G. B. (2016). Average activity of excitatory and inhibitory neural populations. *Chaos*, 26(9).

Roxin, A., Brunel, N., and Hansel, D. (2005). Role of delays in shaping spatiotemporal dynamics of neuronal activity in large networks. *Physical review letters*, 94(23):238103.

Roxin, A., Brunel, N., Hansel, D., Mongillo, G., and van Vreeswijk, C. (2011). On the Distribution of Firing Rates in Networks of Cortical Neurons. *Journal of Neuroscience*, 31(45):16217–16226.

Roxin, A. and Compte, A. (2016). Oscillations in the bistable regime of neuronal networks. *Physical Review E*, 94(1):1–17.

Roxin, A. and Ledberg, A. (2008). Neurobiological models of two-choice decision making can be reduced to a one-dimensional nonlinear diffusion equation. *PLoS computational biology*, 4(3):e1000046.

Roxin, A. and Montbrió, E. (2011). How effective delays shape oscillatory dynamics in neuronal networks. *Physica D: Nonlinear Phenomena*, 240(3):323–345.

Schaffer, E. S., Ostojic, S., and Abbott, L. F. (2013). A Complex-Valued Firing-Rate Model That Approximates the Dynamics of Spiking Networks. *PLoS Computational Biology*, 9(10):e1003301.

Schmidt, H., Avitabile, D., Montbrió, E., and Roxin, A. (2018). Network mechanisms underlying the role of oscillations in cognitive tasks. *bioRxiv*.

Shriki, O., Hansel, D., and Sompolinsky, H. (2003). Rate models for conductance-based cortical neuronal networks. *Neural computation*, 15(8):1809–41.

Siegert, A. J. F. (1951). On the first passage time probability problem. *Physical Review*, 81(4):617–623.

Silberberg, G., Bethge, M., Markram, H., Pawelzik, K., and Tsodyks, M. (2004). Dynamics of Population Rate Codes in Ensembles of Neocortical Neurons. *Journal of Neurophysiology*, 91(2):704–709.

So, P., Luke, T. B., and Barreto, E. (2014). Networks of theta neurons with time-varying excitability: Macroscopic chaos, multistability, and final-state uncertainty. *Physica D*, 267(0):16–26.

Somers, D., Nelson, S., and Sur, M. (1995). An emergent model of orientation selectivity in cat visual cortical simple cells. *The Journal of Neuroscience*, 15(8):5448–5465.

Stein, R. B. (1965). A Theoretical Analysis of Neuronal Variability. *Biophysical Journal*, 5(2):173–194.

Stein, R. B. (1967). Some Models of Neuronal Variability. *Biophysical Journal*, 7(1):37–68.

Tass, P. (1995). Cortical pattern formation during visual hallucinations. *Journal of Biological Physics*, 21(3):177–210.

Tiesinga, P. and Sejnowski, T. J. (2009). Cortical Enlightenment: Are Attentional Gamma Oscillations Driven by ING or PING? *Neuron*, 63(6):727–732.

Tiesinga, P. H. and Sejnowski, T. J. (2010). Mechanisms for Phase Shifting in Cortical Networks and their Role in Communication through Coherence. *Frontiers in Human Neuroscience*, 4(November):1–14.

Touboul, J. (2012). Mean-field equations for stochastic firing-rate neural fields with delays: Derivation and noise-induced transitions. *Physica D: Nonlinear Phenomena*, 241(15):1223–1244.

Tuckwell, H. C. (1988). *Introduction to theoretical neurobiology - volume 1*. Cambridge university press.

Van Vreeswijk, C., Abbott, L. F., and Bard Ermentrout, G. (1994). When inhibition not excitation synchronizes neural firing. *Journal of Computational Neuroscience*, 1(4):313–321.

Veltz, R. (2013). Interplay between synaptic delays and propagation delays in neural field equations. *SIAM Journal on Applied Dynamical Systems*, 12(3):1566–1612.

Wang, X.-J. (2002). Probabilistic decision making by slow reverberation in cortical circuits. *Neuron*, 36(5):955–68.

Wang, X.-J. and Buzsáki, G. (1996). Gamma Oscillation by Synaptic Inhibition in a Hippocampal Interneuronal Network Model. *The Journal of Neuroscience*, 16(20):6402–6413.

Weiss, T. F. (1966). A model of the peripheral auditory system. *Kybernetik*, 3(4):153–175.

Whittington, M. A., Cunningham, M. O., LeBeau, F. E., Racca, C., and Traub, R. D. (2011). Multiple origins of the cortical gamma rhythm. *Developmental Neurobiology*, 71(1):92–106.

Whittington, M. A., Traub, R. D., and Jefferys, J. G. R. (1995). Synchronized oscillations in interneuron networks driven by metabotropic glutamate receptor activation.

Whittington, M. A., Traub, R. D., Kopell, N., Ermentrout, B., and Buhl, E. H. (2000). Inhibition-based rhythms: Experimental and mathematical observations on network dynamics. *International Journal of Psychophysiology*, 38(3):315–336.

Wilimzig, C., Schneider, S., and Schöner, G. (2006). The time course of saccadic decision making: Dynamic field theory. *Neural Networks*, 19(8):1059–1074.

Wilson, H. R. and Cowan, J. D. (1972). Excitatory and inhibitory interactions in localized populations of model neurons. *Biophysical journal*, 12(1):1–24.

Wilson, H. R. and Cowan, J. D. (1973). A mathematical theory of the functional dynamics of cortical and thalamic nervous tissue. *Kybernetik*, 13(2):55–80.

Wimmer, K., Nykamp, D. Q., Constantinidis, C., and Compte, A. (2014). Bump attractor dynamics in prefrontal cortex explains behavioral precision in spatial working memory. *Nature Neuroscience*, 17(3):431–439.

Zhang, K. (1996). Representation of Spatial Orientation by the Intrinsic Dynamics of the Head-Direction Cell Ensemble: A Theory. *The Journal of Neuroscience*, 16(6):2112–2126.

Zhang, L. (2007). How Do Synaptic Coupling and Spatial Temporal Delay Influence Traveling Waves in Nonlinear Nonlocal Neuronal Networks? *SIAM Journal on Applied Dynamical Systems*, 6(3):597–644.